UNIVERSITY OF LEEDS

1D AND 2D PHOTONIC CRYSTALS FOR THERMO-PHOTOVOLTAIC CONVERTERS AND ELECTRO-OPTIC MODULATORS

HANG YU

Submitted in accordance with the requirements for the degree of PhD. Electronics and Electrical Engineering

The University of Leeds

Faculty of Engineering

School of Electronics and Electrical Engineering

March 2022

Abstract

Photonic crystals are widely used in photovoltaic applications such as filters, mirrors and selective radiators due to their tunable energy bands and the advantage that photons travel faster than electrons without interaction. This thesis describes photonic crystal components in thermophotovoltaic systems that may improve the overall efficiency, with particular focus on spectral efficiency and the band structures of 2D photonic crystals under the influence of rough surfaces and complex refractive indices.

Spectral efficiency is crucial for assessing the optical performance of filters. Although 1D photonic crystals have been extensively studied, there are still many open questions on the inevitable fabrication defects in practical production. In this work, the spectral efficiency of a wide range of structures is found to be reduced by the effect of complex refractive index. Studies on the interface roughness show a similar trend and further illustrate that the structures when modified by evolution algorithm allow such defects to be compensated in to some extent. In addition, emissivity studies of 1D photonic crystals have shown that a non-periodic structure can obtain the same radiation peaks as a periodic structure with more layers, while having a smaller total thickness and fewer interference peaks.

To explore the photonic band characteristics of 2D photonic crystals, the structures that achieve the largest bandgaps are obtained by comparing different hole/cylinder shapes in a variety of lattices. Also, alternative materials and optimizations of the filling fraction are used to derive the optimal structure with the maximum photonic band utilization rate, providing a theoretical basis for relevant applications.

In addition, in the study of 2D photonic crystal slabs, it was found that annular holes make it easier to obtain higher effective refractive indices and relatively small bandgap shifts. We report the design of an inner radius optimized honeycomb lattice with annular holes, which exhibits a

normalized bandgap width of $3 * 10^{-6}$ and a utilization rate of less than 0.001%. This helps to achieve fast band switching of the modulator.

Intellectual Property

The candidate confirms that the work submitted is his/her own and that appropriate credit has been given where reference has been made to the work of others.

This copy has been supplied on the understanding that it is copyright material and that no quotation from the thesis may be published without proper acknowledgement.

Signed 

Acknowledgements

The work that I have undertaken for my PhD thesis would not have been possible without the generous help of many people. First of all, I would like to thank my main supervisor, Dr. Zoran Ikonic, for his guidance and patience during my PhD studies, which opened my eyes to a whole new world. I consider it a great privilege to be a student of his, and I will never forget Dr. Zoran Ikonic's dedication to his students and his gentle and approachable attributes. His tireless teaching, encouragement and support over the years, which has inspired me to strive for excellence and to make the most of my doctoral studies!

I am sincerely grateful to the other two supervisors, Prof. Robert Kelsall and Dr. Dragan Indjin. They have given me great support since I started my studies as a researcher. I am very grateful to Prof. Robert Kelsall for his generous advice and encouragement on my thesis and report, which has been of great benefit to me in my academic writing. I am grateful to Dr. Dragan Indjin for his patience in providing solutions and hints when I encountered problems with my computational programs.

I would like to thank Dr. Zhichao Chen for helping me throughout my PhD. I have benefited a lot from his wise advice during my PhD studies. Whenever I had a problem, he was always there to help and to talk to me. I will be grateful for his help. I would like to thank Prof. Mohsen Razavi and the other teachers in the university for providing me with a good atmosphere to study, work and live in. I would like to thank all my fellows at Pollard Institute and all the staff in the school.

Finally, I would like to say a big thank you to my friends and family, especially my fiancée Kunqi Geng. It was their care, encouragement and support over the years that enabled me to devote myself to my studies and successfully complete my dissertation. I have had the pleasure of living in the beautiful city of Leeds for the past five years or so, studying for my Masters and PhD.

Leeds is like a second home to me and I thank you for making my life such an unforgettable experience and a wonderful memory.

Abstract

Photonic crystals are widely used in photovoltaic applications such as filters, mirrors and selective radiators due to their tunable energy bands and the advantage that photons travel faster than electrons without interaction. This thesis describes photonic crystal components in thermophotovoltaic systems that may improve the overall efficiency, with particular focus on spectral efficiency and the band structures of 2D photonic crystals under the influence of rough surfaces and complex refractive indices.

Spectral efficiency is crucial for assessing the optical performance of filters. Although 1D photonic crystals have been extensively studied, there are still many open questions on the inevitable fabrication defects in practical production. In this work, the spectral efficiency of a wide range of structures is found to be reduced by the effect of complex refractive index. Studies on the interface roughness show a similar trend and further illustrate that the structures when modified by evolution algorithm allow such defects to be compensated in to some extent. In addition, emissivity studies of 1D photonic crystals have shown that a non-periodic structure can obtain the same radiation peaks as a periodic structure with more layers, while having a smaller total thickness and fewer interference peaks.

To explore the photonic band characteristics of 2D photonic crystals, the structures that achieve the largest bandgaps are obtained by comparing different hole/cylinder shapes in a variety of lattices. Also, alternative materials and optimizations of the filling fraction are used to derive the optimal structure with the maximum photonic band utilization rate, providing a theoretical basis for relevant applications.

In addition, in the study of 2D photonic crystal slabs, it was found that annular holes make it easier to obtain higher effective refractive indices and relatively small bandgap shifts. We report the design of an inner radius optimized honeycomb lattice with annular holes, which exhibits a

normalized bandgap width of $3 * 10^{-6}$ and a utilization rate of less than 0.001%. This helps to achieve fast band switching of the modulator.

List of publications

Some of the results reported in this thesis have been published in the following journals:

[1] Yu H, Ikonic Z, Indjin D, et al. The effect of interface roughness on spectral efficiency of thermophotovoltaics with multi-layer filters[J]. Optik, 2022, 257: 168663.

[2] Yu H, Ikonic Z, Indjin D. Optimal photonic crystal slabs for modulators based on transitions between photonic bands[J]. Optik, 2022: 169720.

List of abbreviations and acronyms

1D, 2D or 3D	one, two or three-dimensional(photonic crystals)
FDTD	Finite-difference time-domain method
GA	genetic algorithm
H	high (refractive index)
L	low (refractive index)
mpb	MIT photonic bands tool
PhC	photonic crystals
PS	pattern search method
PV	photovoltaic
RI	refractive index
TPV	thermophotovoltaic

Contents

List of Figures

List of Tables

0.3pt 40pt

Chapter 1

Introduction

This chapter outlines the background research of the whole thesis. Thermophotovoltaics have been a hot topic of research in the energy sector in recent years, and the performance and efficiency have been progressively improved with related technological breakthroughs. In this chapter a brief overview of TPV(thermophotovoltaic) systems is given first, including research in the field. One-dimensional photonic crystal, as a highly promising filter material, will be addressed separately with regard to the factors affecting effectiveness and the challenges for industrial development. Finally, two-dimensional photonic crystals (and slabs) will be discussed in terms of their band structures and applications for its characteristics.

1.1 Overview of TPV system

1.1.1 A brief description of TPV system

Thermophotovoltaics convert high-grade thermal energy into electricity [1–3]. This approach is considered important in the energy industry due to its environmentally-friendly characteristics (no pollution, noise and fossil fuels consumption), far better than that of traditional fossil fuel energy. In 1996, JX Crystals from United States reported a portable small-scale thermophotovoltaic power generation system based on GaSb cells, with 90% total energy utilization rate [4]. Western Washington University has developed a sample of a thermophotovoltaic powered automobile, equipped with 8 GaSb TPV components and able to reach 100 miles per hour [5]. The operation process of TPV system can be simply explained through Fig. 1.1. The high-grade heat source drives the thermal emitter to radiate the infrared photon stream, which

is then absorbed by the TPV cell to generate electron-hole pairs. When the cell is externally loaded, the electrons in the conduction bands return to the valence band through the load to form a loop, therby realizing heat conversion to electricity.[6, 7] The energy conversion efficiency can be improved by optimization of TPV cell bandgaps, by careful structural design of system components, and by tailoring the radiation spectrum coming to the PV cells. To recycle the photons which cannot be used by PV(photovolatic) cells, multi-layer spectral filters are used, and this thesis considers the limitations coming from imperfections in practical realization of these filters, and their optimisation.

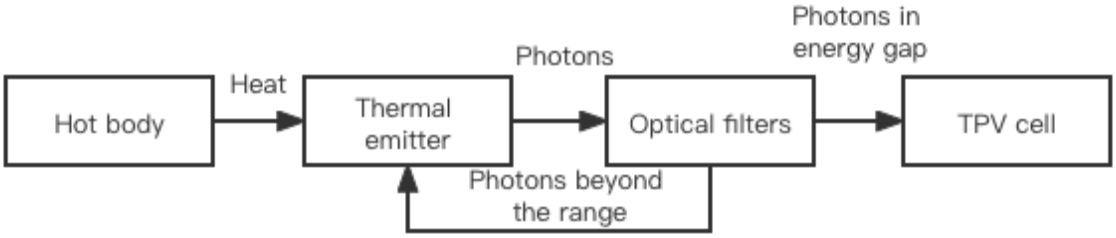

Figure 1.1: Diagram of TPV system.

The design of a spectrally selective filter based on a one-dimensional photonic crystal structure has been investigated with the aim of improving the performance of thermo-photovoltaic devices [6, 8]. The application of an optical filter helps to reflect back those wavelengths which lie outside the most favorable wavelength range, in order to avoid PV cell heating that leads to lower PV efficiency. Previous research has indicated that the efficiency of a TPV system can be enhanced by 45%-75% by the incorporation of such filters [9]. For thermal emitters of TPV system, the best choice to match emission spectrum of GaSb cell is 3D Tungsten photonic crystal [10, 11]. In Natalija Jovanović's research, a 2D PhC in single-crystal tungsten which is well-matched to the PV diode of the whole system is introduced [12]. Compared with 1D PhC, the 2D PhC absorber has obvious advantages, with wider absorption capacity, high absorption rate, and wide-angle of absorption [13].

1.1.2 Recent emergence of TPV systems

Thermophotovoltaic(TPV) is a solid-state energy device which has potential applications in the development and utilization of high-temperature fuel cell waste heat, industrial waste heat, isotope decay heat and solar energy. [14–16] It has been invented for the first time in the MIT in

1960s, with calculated output power of 1W in ideal ambient conditions. [17] The related theory has then been completed and improved by a number of researchers. P. Baldasaro proposed physical model and analysed the operation of a PV cell and emitter. [18] R. Dziendziel has calculated maximum efficiency under ideal conditions. [19] M. Zenker gives measurement of GaSb cell in TPV system applying different emitters as shown in Table. 1 [20]. M. Whale's team proved that the radiation density would increase when the distance between the radiation source and PV cell is smaller, by using micro-scale radiation conversion theory. [21]

Table 1.1: Measurement of TPV systems applying different emitters[20].

Type of emitter	System efficiency	Power density(W/(cm)^2)
Ideal emitter	33%	2.8
Grey body emitter	8.9%	1.1
Selective emitter	14%	1.1

1.2 One-dimensional Photonic crystal

1.2.1 Development of 1-D PhC for TPV applications

The conversion efficiency of a TPV system can be improved by controlling the radiation energy spectrum accepted by the cell. Thus one research approach worth pursuing is to improve the performance of optical filters. For example, a structure composed of 1-D photonic crystal and semiconductor film was presented in 2004 to achieve wide reflection bandgap which reflected back most of the photons that cannot be accepted by the emitter.[22] Related research on 1-D PhC filters revealed that it possesses promising spectrum characteristics, especially under high temperature conditions over 1500K.[23, 24] Based on the features of easy fabrication, simple structure and excellent filtering performance, F. O'Sullivan's group has designed an one-dimensional Si/SiO2 PhC filter and the results of numerical simulation agree well with the experimental results.[25, 26] However, the reflection peak in the photonic crystal bands may reflected back some photons which could be converted, especially those located near the reference wavelength of PV cell. This may cause severe reduction of system spectral efficiency and output power density. The discussions on influential factors on optical performance will be given in the next chapter.

1.2.2 Influential factors on optical performance

Considering the characteristic matrix of the film and the parameters included, the change of incidence angle will affect the equivalent admittance and the optical thickness of the film. [27, 28] According to Bloch's theorem, the dispersion relationship of photonic crystal can be found by using transfer matrix method for wave transmission in periodical structure:

$$cos(KD) = cos\delta_1 cos\delta_2 - \frac{1}{2}[\frac{n_1}{n_2} + \frac{n_2}{n_1}]sin\delta_1 sin\delta_2 \tag{1.1}$$

where K is the wave vector of periodical Bloch wave, δ_i represents the change of light phase in the dielectric layer and λ is the wavelength of incident light. The bandgap width can be derived by equation (1.2):

$$\triangle\omega = \frac{\pi\omega_0}{4cos\theta} sin^{-1}(\frac{n_1 - n_2}{n_1 + n_2}) \tag{1.2}$$

where ω_0 is the corresponding central frequency of central radiation wavelength λ and $\theta istheincidenceangleofli$

Table 1.2: Bandgap width for different incidence angle.[29]

Clockwise angles θ	0	30	60	75
Normalized bandgap width $\triangle\omega$	4.0735×10^{11}	4.7036×10^{11}	8.1496×10^{11}	1.5739×10^{11}
Counter clockwise angle $-\theta$	0	-30	-60	-75

Table 1.2 gives the bandgap width when the incidence angle varies from 0 to 75°. In this case, the refractive index of two media are 2.38 and 1.35 respectively and the geometric thickness for one period is $2000nm$. Central radiation wavelength is $1550nm$ [29]. By reading this table, the fact can be revealed that the bandgap width is increasing with incidence angle. It is interesting to point out that, when the incidence angle increases from 0-30°, the increase of width of bandgap is not that obvious. But from 30-60° and 60-75°, the value almost doubled. Photonic crystal, as the structure with periodically arrayed different materials, can be significantly influenced by the change of parameters of the structure. By increasing the number of periods, the oscillation occurs at the top of the middle transmission band. The number of the oscillation peak equals n-1. With increase of the number of periods, the transmission peaks on the side of the band

have increased and their width tuned to be narrower.[30] When the defect layer with complex refractive index is added in the multilayer structure, the number of periods of real RI layer will affect the defect mode as well.[8, 31]

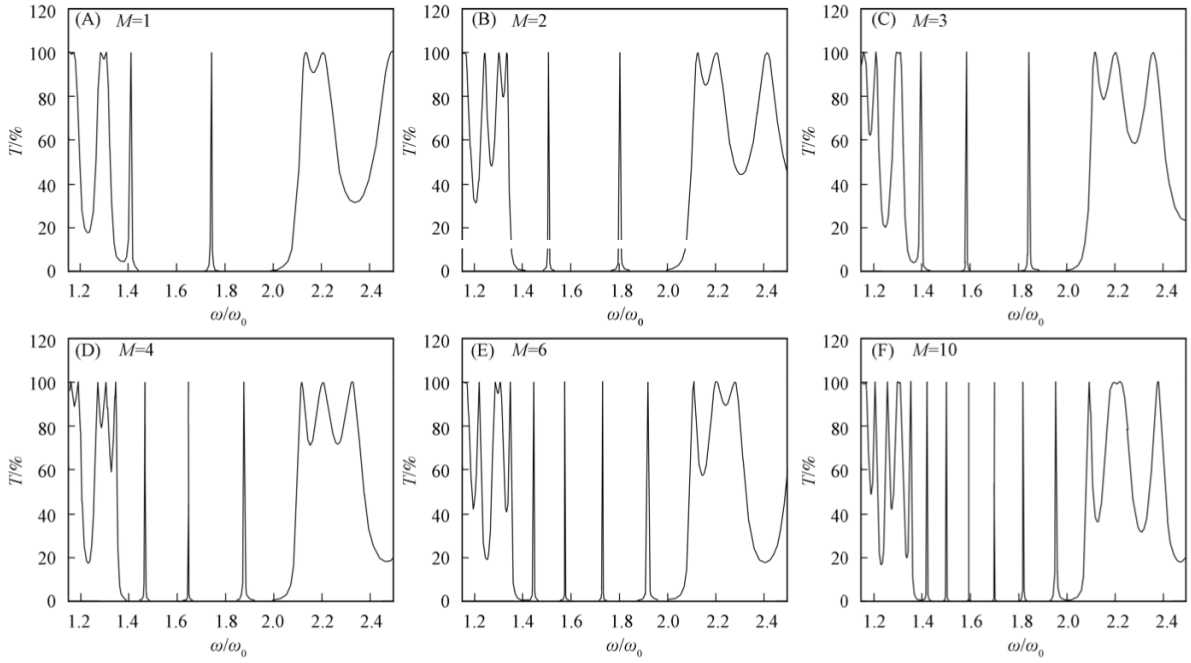

Figure 1.2: Transmittance for different number of periods of defect layers.[8]

The structure of 1D PhC is $(AB)_N(D)_M(AB)_N$ and complex refractive index of defect medium D can be written as:

$$n_D = n + iC_\lambda/n \tag{1.3}$$

where C equals 5.44 μm and n is the real part of the medium index which is 3.0. λ is the wavelength of the incident wave. The thicknesses of layers nm for real refractive index and 344 nm for complex index layer respectively. The refractive index of medium A and B are 1.38 and 2.35. When the number of periods of defect medium D remains at 2 and increase the number of periods N, the defect mode turns to be sharper. If the number of periods continues to increase, the defect mode would vanish which means there is a limitation for the number of periods. If the number of periods M is increasing, as shown in Figure 1.2, the number of defect modes is increasing. A transmittance defect mode with almost 100% of reduction occurs in the band gap. The bandgap location and width do not change.

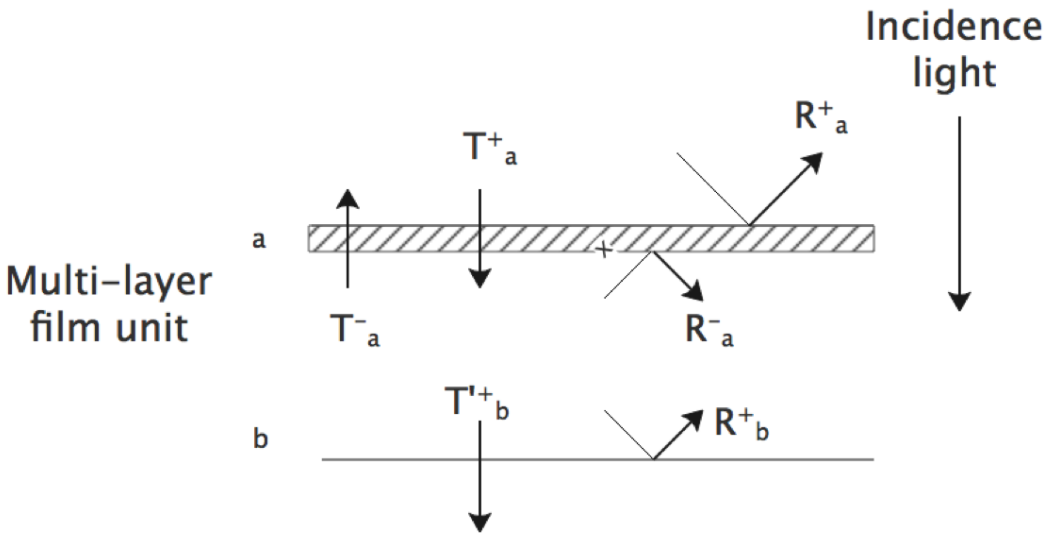

Figure 1.3: Instruction graph of reflectance on the substrate.

Figure 1.3 shows the reflection of incidence light both on the front side and back side of layers. The reflectivity can be calculated as[32]:

$$\begin{aligned} R &= R_a^+ + T_a^+ R_b^+ T_a^- [1 + R_a^- R_b^+ + (R_a^- R_b^+)^2 + ...] \\ R &= R_a^+ + \frac{T_a^+ R_b^+ T_a^-}{1 - R_a^- R_b^+} = \frac{R_a^+ + R_b^+ (T_a^+ T_a^- - R_a^+ R_a^-)}{1 - R_a^- R_b^+} \end{aligned} \tag{1.4}$$

where $R = \frac{R_a + R_b - s R_a R_b}{1 - R_a R_b}$ if there is no absorption of optical thin film. Similarly, the transmittance of multi-layer AR can be obtained as:

$$T = T_a^+ T_b^+ + T_a^+ T_b^+ R_a^+ R_a^- [1 + R_a^- R_b^+ + (R_a^- R_b^+)^2 + ...]$$

$$T = \frac{T_a T_b}{1 - R_a R_b} \tag{1.5}$$

In Hendradi Hardhienata's research, the refractive index of medium 1 and 2 are set as 1 and 3 respectively. d_1 and d_2 represent the thickness of two layers. By comparing Figure 1.3 (a), (b) and (c), the width of the bandgap gets larger when the thickness of the medium increases. In addition, the transmittance peaks move to longer wavelength [33].

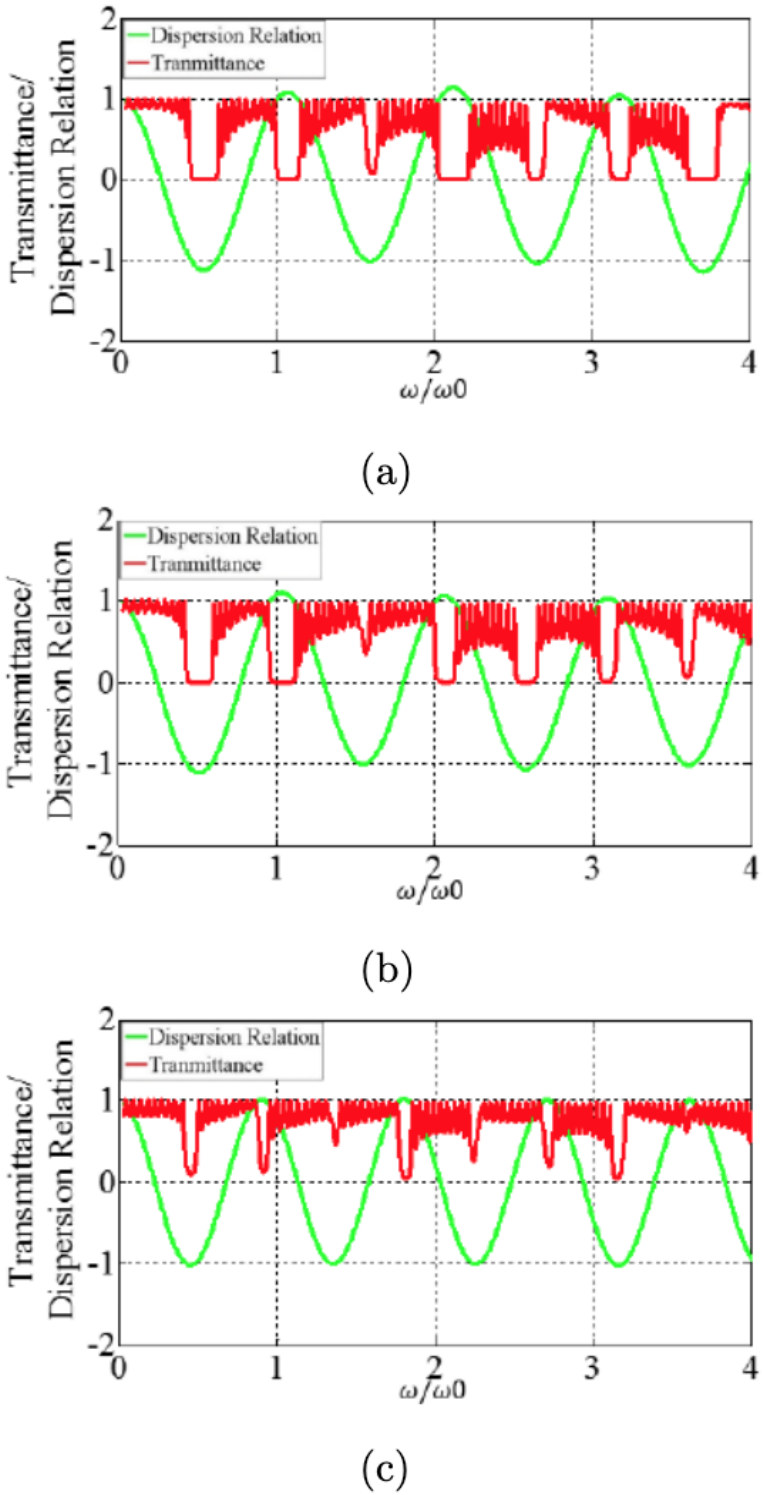

Figure 1.4: Transmittance for different thicknesses of layers (a) d1=0.4mm,d2=0.6mm; (b) d1=0.6mm,d2=0.6mm; (c)d1=0.6mm d2=0.8mm[33].

1.2.3 Challenges in the application of PhC

The refractive indices in the above discussion correspond to the ideal materials. Typically, the expression for complex RI can be written as $n + ik$, which consists of refractive index as its real

part n and its imaginary part k proportional to the absorption coefficient. With consideration of complex values here, the attenuation characteristic of transmission of light in the medium can be simulated by the mathematical models and shown in the form of figures. The simulation is based on multilayer filter TPV systems and the material are Si and SiO_2, with complex refractive indices given in the related literature. Here, complex RI is introduced to show both real and imaginary parts of refractive index in limited periods of 1D PhC. For example, if the complex refractive index is taken into consideration, the characteristic of transmittance peak in TE mode for different incidence angles can be shown in Fig. 1.5[34].

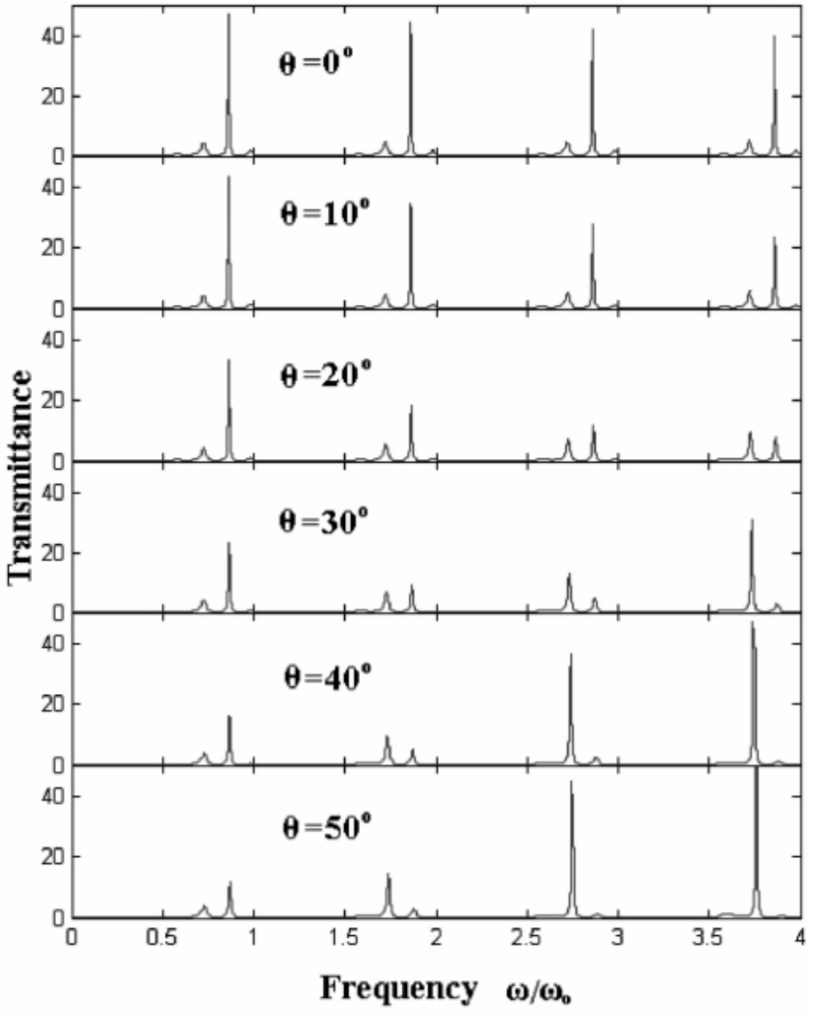

Figure 1.5: Transmittance characteristic with different incidence angle in TE mode [34].

This research is based on 1-D quasi-periodic photonic crystal with real medium A and designed medium B. Medium A is Silicon with real refractive index and medium B is made of complex refractive index ($n_B = 1.365 - 4.27i$) material. The number of periods is taken to be 5 and the incidence angle step is 10°, from 0 to 50°. As the angle of incidence increases, the transmittance

of each main peak decreases monotonically, and the transmittance of each sub-peak increases monotonically. The absolute value of transmittance versus incidence angle gets larger when the relative frequency of the peaks get higher. However, the locations of peaks do not change with different incidence angles.

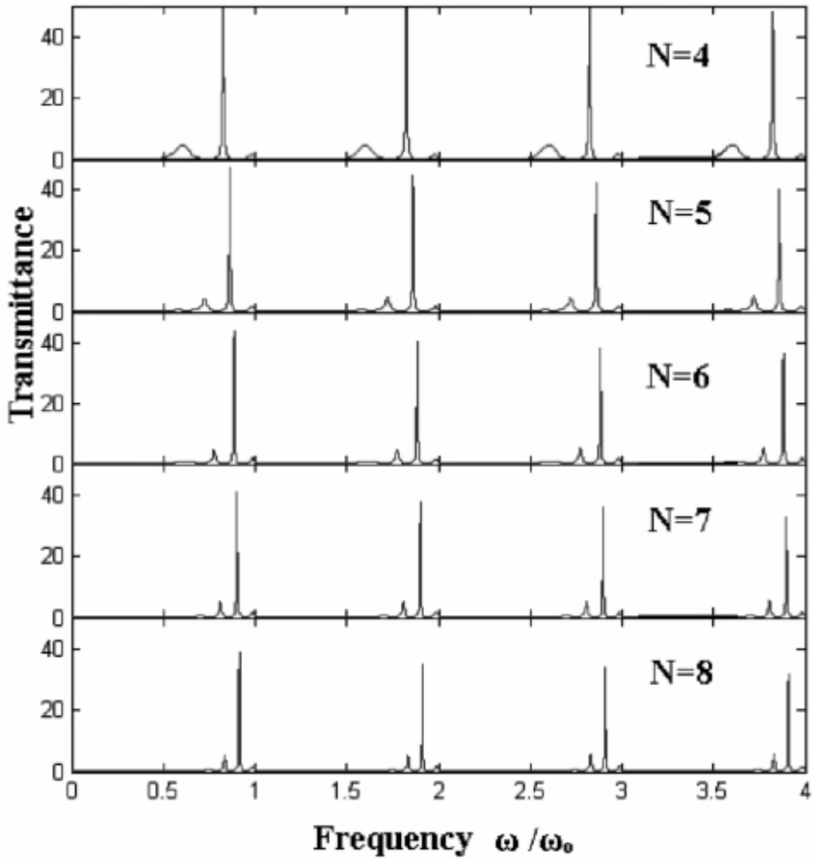

Figure 1.6: Transmittance for different number of periods, with complex index layers[34].

The condition above regards complex index layer as the defect layer, if it has the same number of periods as the real index layer, e.g. (AB)N structure, the transmittance would decrease while the peaks of transmission move towards short wave direction[34]. The transmittance is shown in Fig. 1.6. With the increase of number of periods, the location of main peaks slightly moved to the shorter wavelength, while the sub-peaks show obvious movement in the same direction. Also, the larger the corresponding frequency at main peaks, the larger the absolute value of period changing. Table 1.3 shows the transmittance values at different major peaks:

Table 1.3: Transmittance for different number of periods[34].

Number of period	4	5	6	7	8
The first main peak	56.0	46.0	43.3	41.1	38.9
The second main peak	53.3	43.8	40.5	37.8	35.1
The third main peak	51.3	41.1	37.8	36.2	34.0
The fourth main peal	48.7	38.9	36.2	33.4	31.8

Under the condition that complex refractive index is taken as the defect layer property, the thickness of real index layers makes almost no difference on the bandgap width. The defect mode moves in the high frequency direction with increasing thickness. This means that the change of thickness influences the bandgap central frequency of photonic crystals[34, 35].

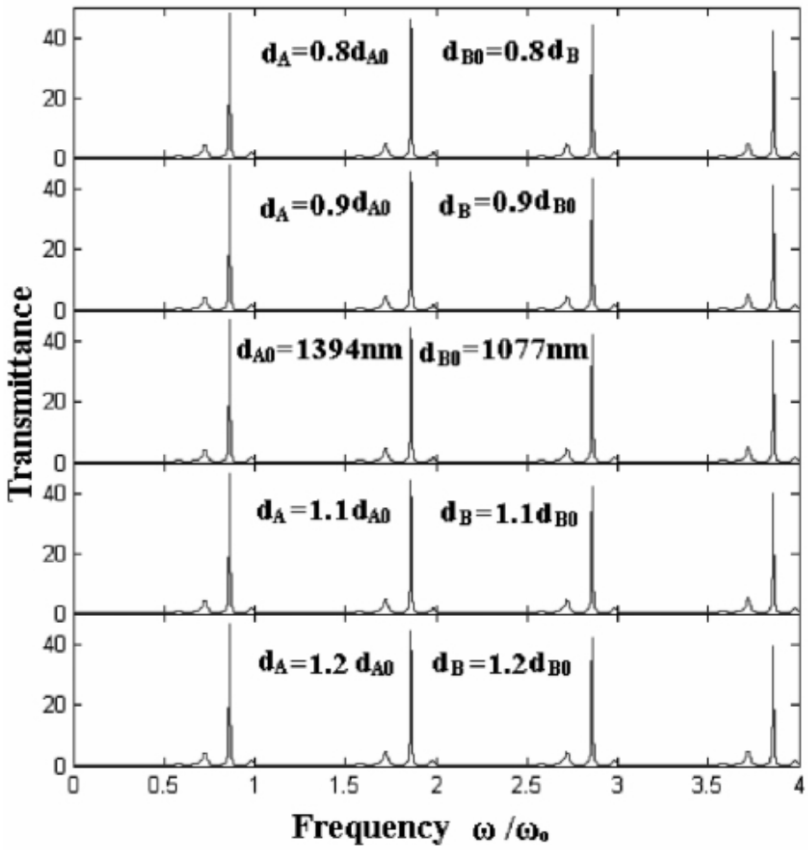

Figure 1.7: Instruction graph of reflectance on the substrate.[34]

Figure 1.7 shows the transmittance characteristics for different layer thickness in the structure with real index medium A and complex index medium B, periodically arrayed. For each increase of thickness of two layers, from 0.8 d_{A0}, 0.8 d_{B0} to 1.2 d_{A0}, 1.2 d_{B0}, the transmittance of main peaks decrease by a factor of 2.2%. The changing trend of transmittance of the four main peaks all follow the rule that all their transmittance reduces with the same reduction.

Another class of defects that may not be avoided in the fabrication process is roughness of the interface or surfaces of thin films. Various filter designs, based on multilayer stacks, have been considered in the literature, assuming that the interfaces are perfectly flat. In this work we account for the effect of interface roughness, which is known to affect the spectral properties of thin films, as discussed by A. Tikhonravov, et al [36].

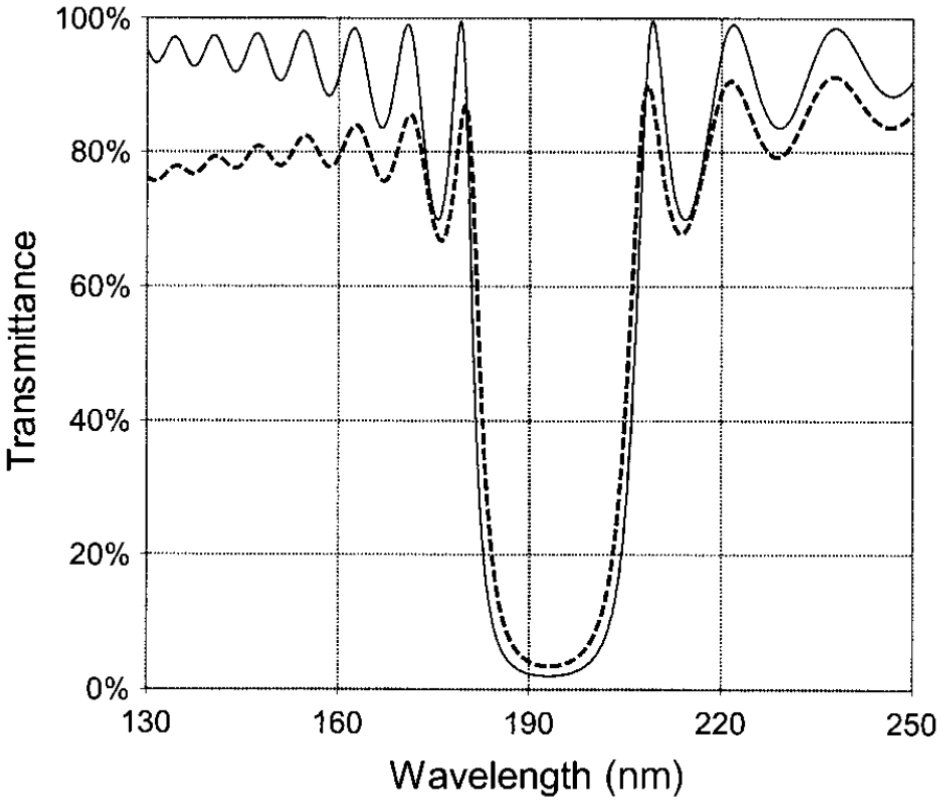

Figure 1.8: Comparison of the transmittance for ideal surface(solid) and large-scale roughness(dashed)[36].

Figure 1.8 shows the transmittance of ideal 31-layer quarter-wave mirror with and without small-scale roughness added. The value of rms roughness has been set to 5 nm for each interface. It is obvious that ideal mirror surfaces give higher average and peak transmittance than with small-scale interface roughness. For multilayer SiC films on Si substrate, the reflectance spectrum is shown in Figure 1.9.

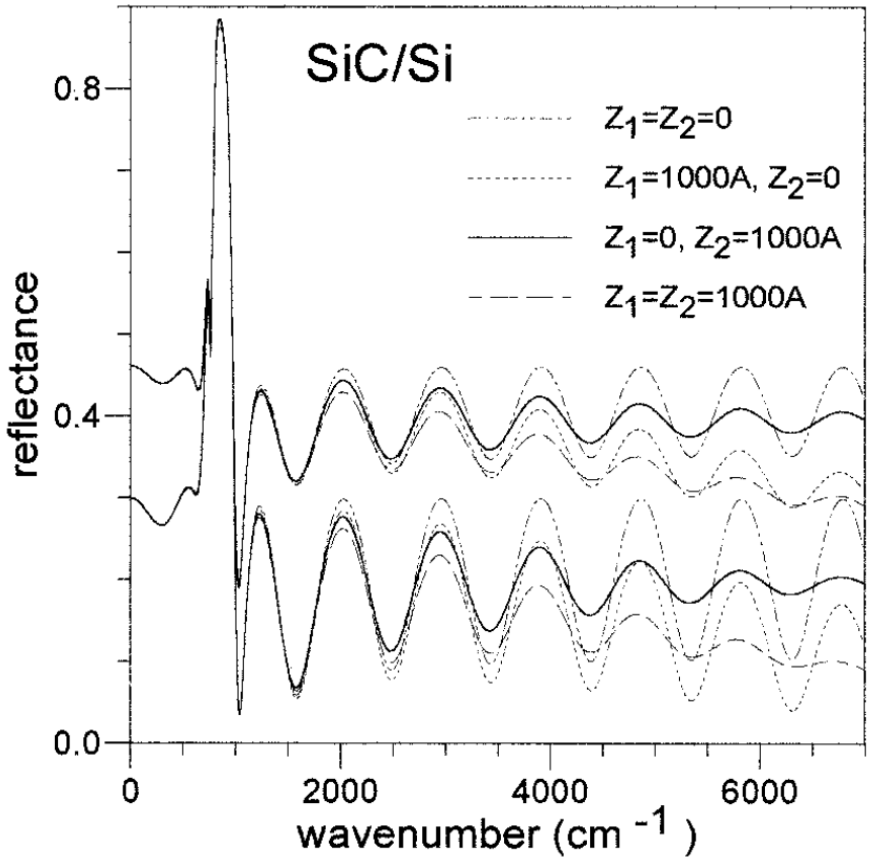

Figure 1.9: Influence of rough interfaces for a SiC layer on Silicon substrate[37].

The reduction can be observed when the interface or surface roughness is considered, compared to the ideal SiC-Si structure. The average reflectance is reduced, especially for high frequencies. If both surface and interface have same amount of roughness, a severe reduction exists.

1.3 Two-dimensional Photonic crystal

1.3.1 Overview of 2-D PhC

For 2-D photonic crystals, the rods can be arrayed as in the structure in Figure 1.10:

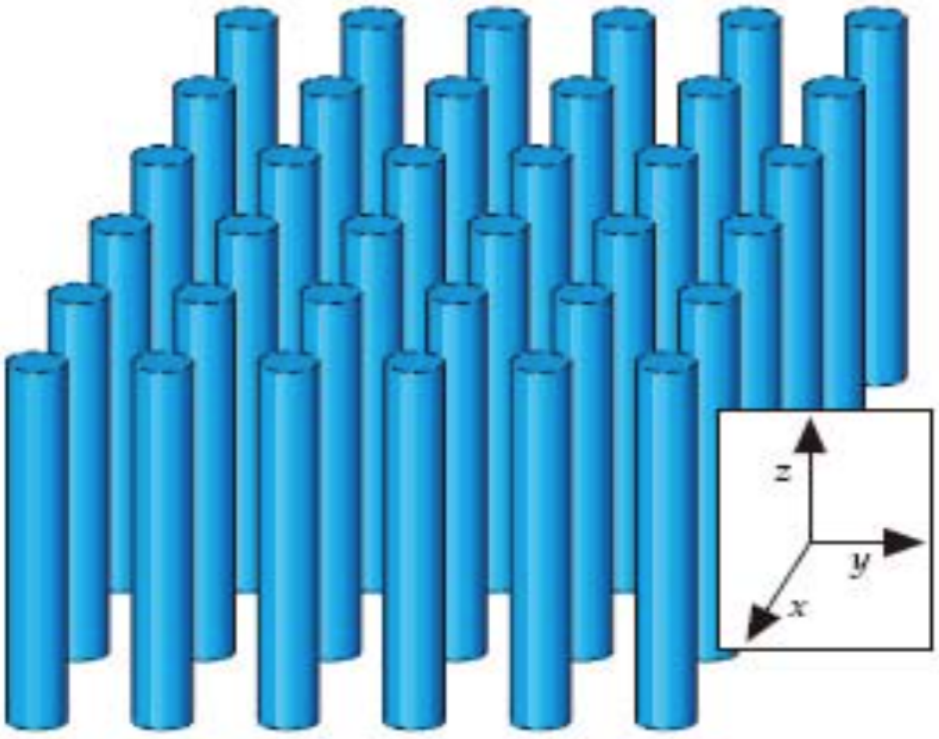

Figure 1.10: Schematic diagram of 2-D photonic crystals.

Two dimensional photonic crystal consists of dielectric rods in air or air holes in dielectric substrate, and features periodic structure in a plane perpendicular to the rods axis. The permittivity of this structure is periodic function of the spatial position in the direction perpendicular to the rods, while in the direction parallel to the column axis the permittivity does not vary with the spatial position [38, 39]. The increasing interest in controlling thermal radiation using photonic crystals has high-lightened the need for high-performance thermal emitters. [11, 40–42] Most of research on periodic microstructred selective emitter was focused on 2-D tungsten PhC[12, 43–45]. Besides, Tantalum has an extremely high melting point (3290K) and small coefficient of expansion, which is also a good material in TPV applications. The results indicate that for wavelengths larger than the cut-off wavelength, the average emissivity of tantalum is greater than that of tungsten.[45–48] Selective emitters can be designed to match different TPV cells by adjusting the size of its structure. Theoretical studies have shown that the spectral modulation of two-dimensional photonic crystals is mainly influenced by microcavity resonance (resonant cavity effect), whose cut-off wavelengths can all be calculated from the resonant frequency of the fundamental mode of the resonant cavity, which is twice as deep as the hole

depth.[12, 49–51] For rectangular holes, the calculation of cutoff wavelength λ_{cutoff} is:

$$\lambda_{cutoff} = \frac{2}{\sqrt{\left(\frac{l}{L_x}\right)^2 + \left(\frac{m}{L_y}\right)^2 + \left(\frac{n}{2L_z}\right)^2}} \tag{1.6}$$

Here, l, m and n are all integers and the micro cavity size is $L_x \times L_y \times L_z$. Similarly, the formulae for structure with circular holes for TE and TM modes are:

$$f_{TM} = \frac{1}{2\pi\sqrt{\mu\varepsilon}}\sqrt{\left(\frac{X_{mn}}{a}\right)^2 + \left(\frac{p\pi}{2d}\right)^2} \tag{1.7}$$

$$f_{TE} = \frac{1}{2\pi\sqrt{\mu\varepsilon}}\sqrt{\left(\frac{X'_{mn}}{a}\right)^2 + \left(\frac{p\pi}{2d}\right)^2} \tag{1.8}$$

Here, X denotes the nth root of the first class Bessel function of order m, X' denotes the nth root of the derivative of the first class Bessel function of order m, a is the radius of the cylindrical hole, d is the depth of the cylindrical hole, μ and ϵ denote the magnetic and electrical permeability of the material filling the cylindrical hole, respectively.

1.3.2 2-D photonic crystal slab

A two-dimensional photonic crystal repeats infinitely in both directions in the plane and is homogeneous and extends infinitely in the third direction perpendicular to the plane of the period. In this case, the photonic bandgap exist in all directions in the periodic plane. The intensity of the light field in the vertical direction is assumed to be constant. Under this assumption, the light propagating in the periodic plane can be divided into two polarisation states, the transverse electric mode (TE) and the transverse magnetic mode (TM). It is important to mention that the definitions of the electromagnetic field vectors in TE and TM modes in photonic crystals is quite different from that in classical optical theory. From analytical perspectives, the TE and TM modes have covered all the electric field and magnetic field in the photonic crystals respectively [52, 53]. The other field components can be easily obtained from one field component in the same polarization which describes the plane electromagnetic wave. Thus, the numerical calculation can be simplified to build such ideal two-dimensional photonic crystal model. The ideal model which does not exist in real life helps to understand possible properties of 2-D PhC.

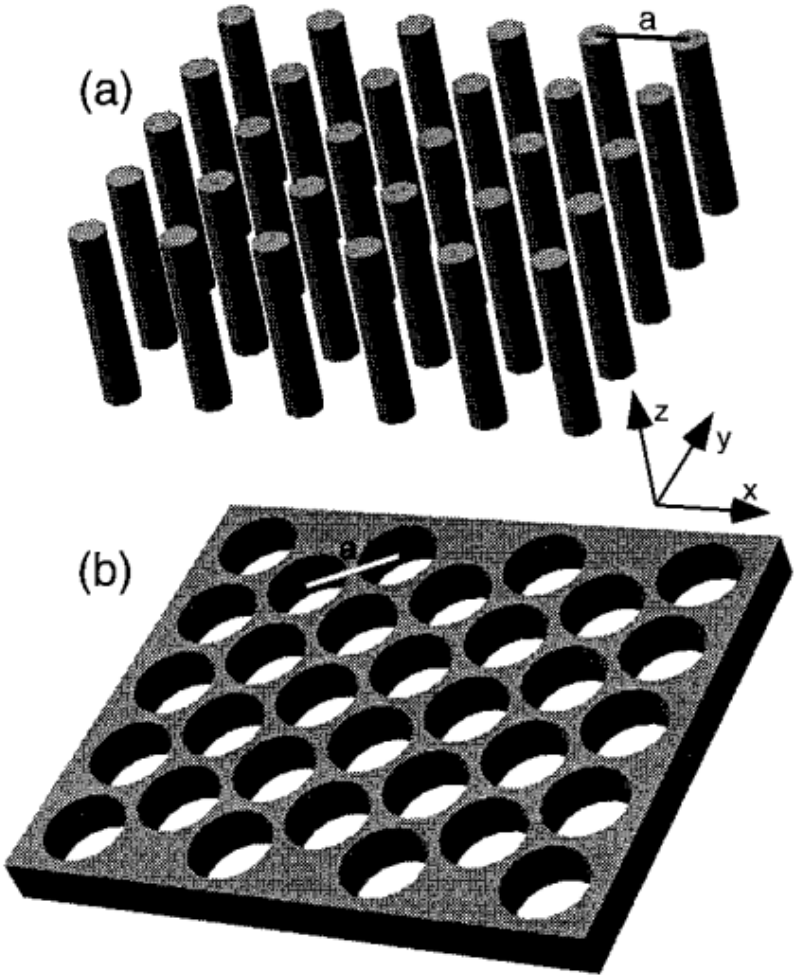

Figure 1.11: Two-dimensional photonic slabs:(a) Square lattice with dielectric rods in air, height=2.0a;(b) Triangular lattice with air holes in dielectric slab, thickness=0.6a [52].

For the slab structure, with its finite height (unlike the conventional two-dimensional materials), the light is confined in the slab because of the refractive index difference between the slab and cladding layers on the upper and lower sides [52, 54, 55], and the dispersion will not be exactly the same as for the two-dimensional photonic crystal. It is useful to add the dispersion curve, called light cone (calculated with the average refractive index of the photonic crystal slab), in the band structure diagrams. It is important to note that the slab structure features symmetry on the plane z=0 and the k-vectors on x and y planes are observation targets. Thus, the TE and TM polarizations can be simply replaced by their analogous modes: even and odd modes respectively [56].

The state-of-art photonic crystal slab has dielectric rods on the substrate which are arrayed periodically and filled with air. Another approach is etching of holes periodically on the sub-

strate, which is also the preferable way to achieve slabs due to its easy control of operation and accuracy [57]. Steven G Johnson's team first investigated the guided mode of photonic crystal slab using plane wave method with super cells.[52]. Due to the theoratical limitations, the leaky mode of PhC slab cannot be calculated. Fan's research group focused on solving field distribution of eigenmodes using FDTD [53]. But there is still no direct way to calculate the dispersion relation and field distribution for the leaky mode of a photonic crystal slab until scattering matrix method was first used to calculate the reflection and transmission of a photonic crystal slab with a substrate by DM. Whittaker without providing the calculations of eigenmodes directly[58]. The calculation of eigenmodes of photonic crystal slab in air was then fulfilled by N Carlson [59] with only guided mode involved and then applied to specific structure by Tikhodeev [60].

1.3.3 Characteristics of band structures

Photonic crystal bandgaps have the property of scaling independence, which means that if all the parameters of 2 PhCs are the same except size, they possess the same band structures. The only difference between them is the wavelength range of bandgaps. Therefore, the normalised frequency $a/2\pi c$ is often used in discussing photonic band structures. Assuming that there is no net charge in the PhC and the current is zero, according to Maxwell equations,

$$\begin{aligned} \nabla \cdot D &= 0 \\ \nabla \cdot B &= 0 \\ \nabla \times E &= -\frac{\partial B}{\partial t} \\ \nabla \times H &= \frac{\partial D}{\partial t} \end{aligned} \tag{1.9}$$

By initializing lattice constant a, the scale in Eq. (1.9) can be converted to:

$$\begin{aligned} \frac{r}{a} &= r' \\ \frac{ct}{a} &= t' \end{aligned} \tag{1.10}$$

Here, r' and t' are dimensionless wave vector and time. Then the dielectric function and magnetic field intensity are concluded as:

$$\begin{aligned} \varepsilon'(r') &= \varepsilon(r) \\ H'(r') &= H(r) \end{aligned} \tag{1.11}$$

Based on the Eq. (1.11), $H'(r', t')$ must satisfy the following condition[61]:

$$\nabla' \times \frac{1}{\varepsilon'(r')} \nabla' \times H'(r') = \frac{\omega^2}{c^2} H'(r') \tag{1.12}$$

Here, ∇' is used as notation of gradient of r'. If the remaining parameters of the two photonic crystals are the same except the scales, then their eigenequations can be written in the same form as the equation for the dimensionless dislocation vector by scale transformation, i.e. the photonic crystal is scale-free. Therefore, in photonic crystals, normalised frequencies are usually used when frequencies are involved:

$$\omega_C = \omega a / 2\pi C \tag{1.13}$$

It is clear that the photonic crystal bandgap is determined by the lattice constant. Any bandgap in the specific wavelength range required can be obtained by simply changing the lattice constant using the normalised frequency. In the following discussions, $a/2\pi c$ is used as the unit of frequency.

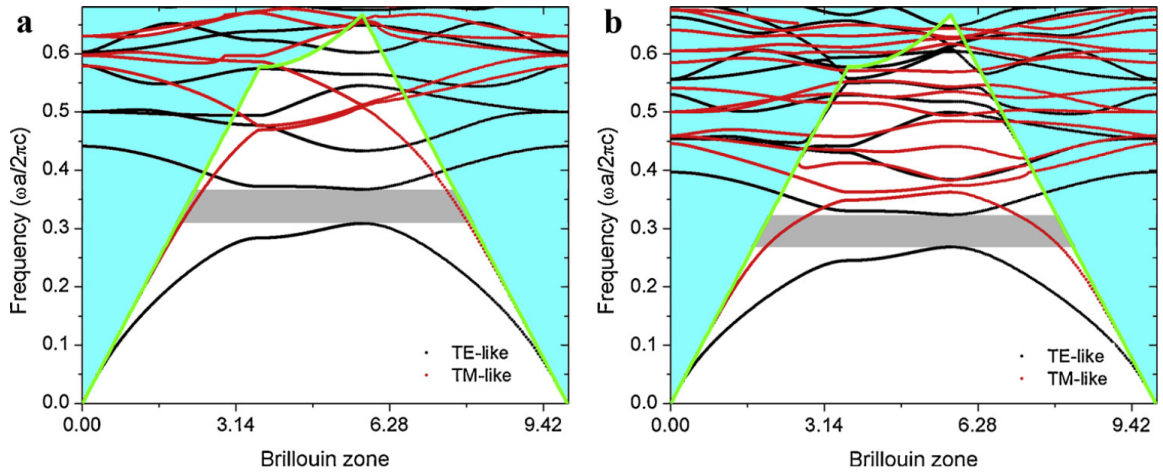

Figure 1.12: Photonic band structures of different slab thickness of (a)d=0.3a, (b)d=0.5a. [62].

The band structures of photonic crystal slabs with different substrate thickness are shown in

Fig. 1.12 [62]. The green curves are the light cone and the blue area is the notation of limitation of light by the Fresnel reflection due to the refractive index difference in the vertical direction. By increasing the slab thickness, the range of TE-like bandgap remains and moves to the lower frequency. The most important feature of the energy band diagram of planar photonic crystal is the light cone. Within the light cone, there is a continuous region containing all possible frequencies in the background. In a homogeneous background, the light cone is simply the wave vector divided by the refractive index: k/n.

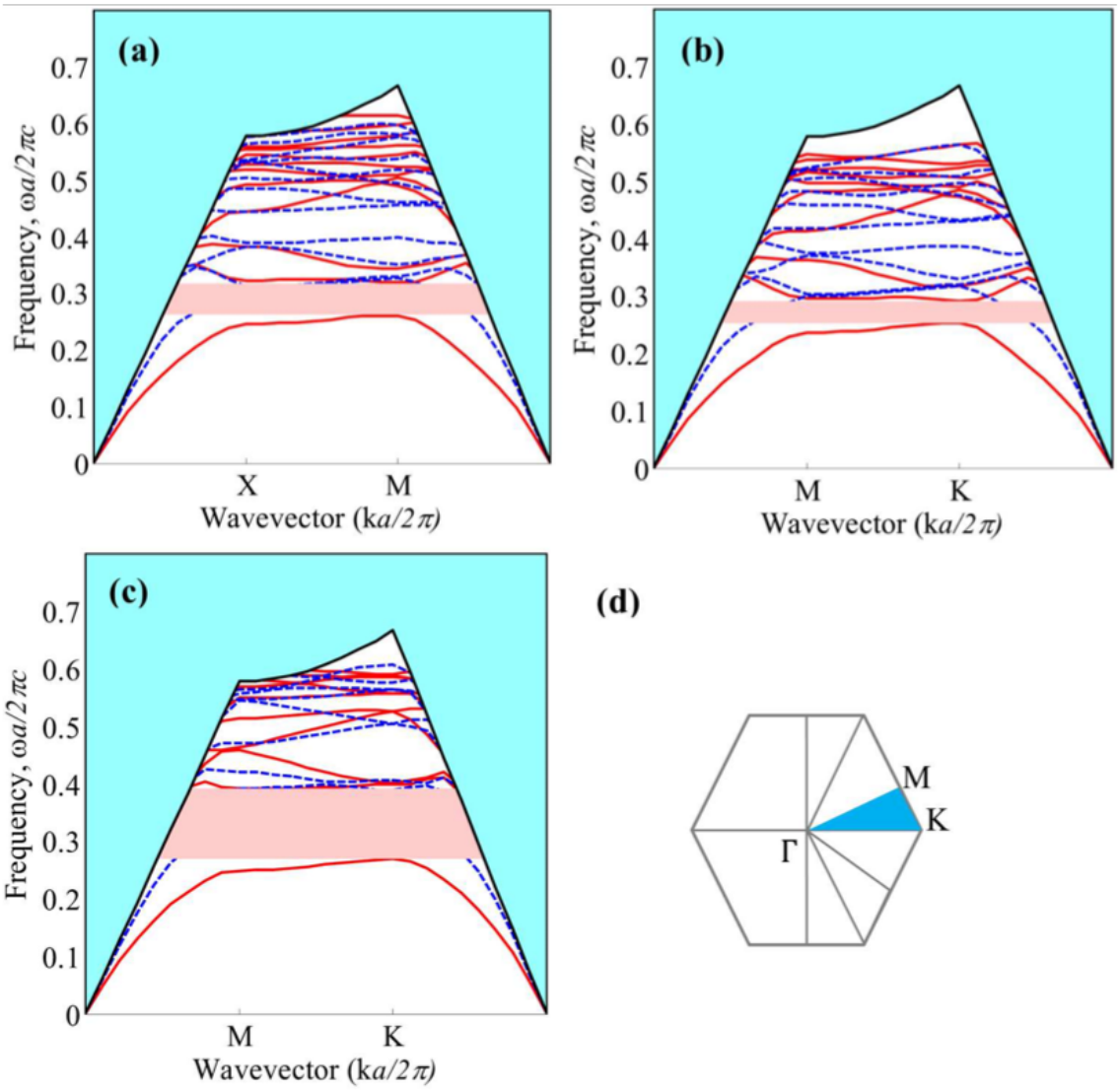

Figure 1.13: Band diagram of triangular lattice with (a) elliptical, (b) rectangular, (c) hexagonal air holes and (d) the first Brillouin zone of hexagonal structure. [63].

For a periodic background, the light cone is the lowest energy band of the corresponding two-dimensional system. Fig. 1.13 shows the band diagram of triangular lattice with different

shape of holes etched in [63]. From the simulation results, the hexagonal structure gives the largest TE-like bandgap. The second largest bandgap is observed in elliptical structure, with approximately half the size of that in hexagonal structure. Rectangular hole is another case for comparison, and the bandgap is only around a quarter of that in the optimal structure.

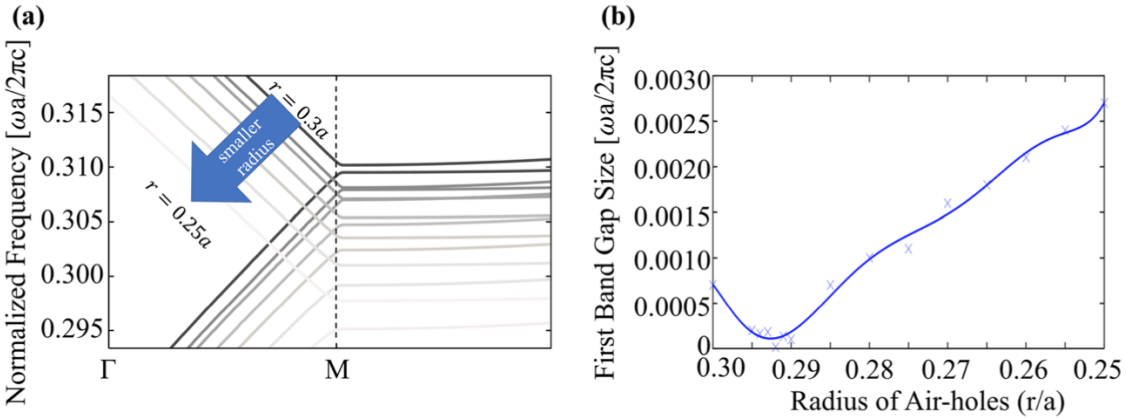

Figure 1.14: Band structures for first 2 photonic bands:(a) for different air-hole radius ranges from 0.25-0.3a; (b) the minimum bandgap when radius=0.292a [64].

Maximizing the photonic bandgap width is always the priority for researchers to bring it into various applications. These include e.g. using line defects to form optical waveguides or using point defects to form optical microcavities [65–67]. The properties become more meaningful when the bandgap width of a photonic crystal is increased, so efforts have been made to increase the bandgap width of photonic crystals. Besides, the bandgap width can be also minimized from modulating perspective. In terms of operating frequency during modulation, smaller bandgap width is easier for band switching [64].

1.4 Research work in this thesis

As mentioned earlier, in terms of improving the overall conversion efficiency of thermophotovoltaic systems, the main research hotspots focused on are how to improve the filtering and radiation efficiency of the internal components of the system. Therefore, using photonic crystals as the topic of exploration, the main chapters of this thesis are organised as follows. Chapter 1 focuses on some background knowledge and process development of photonic crystals and thermophotovoltaic systems involved in this thesis. Starting with the challenges of efficiency improvement in TPV systems, the application of photonic crystals in TPV components such as optical filters and thermal emitters is presented, with an emphasis on the problems that may be

faced in fabrication and the band structures of photonic crystal slabs. Chapter 2 gives the basic theory and methods for designing and analysing photonic crystals. It covers the mathematical principles used for modelling, the effects of complex refractive index and interfacial roughness on spectral efficiency, as well as the optimisation scope and objectives of genetic algorithm.

In Chapter 3 ,the emission performance of non-periodic arrangements of one-dimensional photonic crystals is analysed. The emissivity peak, central frequency and total layer thickness of the 4-layer non-periodic structure and the 10-layer periodic structure are investigated using the transfer matrix method. The optimised non-periodic structure is found to have the same high emissivity and smaller thickness.

Chapter 4 discusses a variety of materials and structures for 1D photonic crystals, with reference to relevant studies and self-designed crystal models. On this basis, the effects of the complex refractive index and the roughness of the interface on the spectral efficiency are studied separately. It is shown that each of these factors causes a reduction in optical efficiency, and optimization of the layer thickness using genetic algorithm is necessary to achieve performance similar to that of the original structure.

Different material choices for two-dimensional photonic crystals are given in Chapter 5. Using the plane wave expansion method to simulate silicon/air and tungsten/air respectively, it is concluded that the tungsten structure has a larger photonic band due to its larger dielectric constant difference. The optimised filling fraction results in a structure with the maximum bandgap utilisation.

Chapter 6 continues the exploration of the properties and applications of the minimum photonic bandgap, based on the study of the maximum bandgap in the previous chapter. Using the plane wave expansion method and the MPB tool, various combinations of lattice types and hole shapes are calculated and compared. It is shown that the highest effective refractive index change and the smallest bandgap width can be obtained for annular hole in honeycomb lattice.

Chapter 7 concludes and gives an outlook on the whole research work of the thesis.

1.5 Novelty and highlights

The main innovative points and highlights of this thesis include:

(1) A 4-layer non-periodic structure with the same high emission efficiency as the self-designed 10-layer 1D photonic crystal structure is given. After optimization, the main emission peak of the periodic structure remains unchanged and the maximum value of the clutter peak is promoted, increasing the possibility of improving the utilization in specific frequency range; the main emission peak of the non-periodic structure is narrower and closer to the emission performance of the periodic structure without deviating from the central frequency.

(2) The genetic algorithm optimized model has better average spectral efficiency when optimization target is spectral efficiency rather than transmittance. Smaller number of layers can be a good choice if roughness cannot be avoided. The Si/SiO_2 structure has higher spectral efficiency than that of SiO_2/TiO_2 for the same type of structure. Structure with optimized layer widths and interface roughness considered can slightly improve the optical performance of filters.

(3) The required effective refractive index change coming from a shift in the energy band structure of a photonic crystal is generated. Comparison made for three lattices with eight hole shapes for effective refractive index variation leads to the conclusion that honeycomb lattice with annular holes is the optimal structure. Using Genetic algorithm to optimise the inner radius of the annular structure, the resulting two-dimensional photonic crystal slab can switch bands rapidly in a very small frequency range.

Chapter 2

Methods

This chapter contains the methods used in the study. First, two mathematical methods applied to form one and two-dimensional photonic crystals are presented, together with the derivation of the calculation of the spectral efficiency. Then, a theoretical analysis of the defect problems that may be encountered in the practical production process, such as the complex refractive index, and the roughness of the interface are given. Finally, the simulation tools and optimisation algorithms used in this paper are briefly described. The spectral efficiency of the model is optimised through a series of calculations and parameter adjustments, and the optical performance of the optimal structure is found. The theoretical principles and optimisation analysis of photonic crystals for use in thermophotovoltaic systems are detailed.

2.1 Mathematical principles

2.1.1 Transfer matrix method(TMM)

To develop a photonic crystal model, the Transfer Matrix Method is used to implement it in the simulation software. Transfer matrix can be derived by applying thin film optical theory, the admittance of medium can also be calculated. The essence of transfer matrix is that it is the product of feature matrix of each layer [68, 69]. By calculating the admittance of medium, the reflection and refractive coefficient can be obtained as a result. The sketch of electromagnetic wave passing through the single layer thin film is shown below:

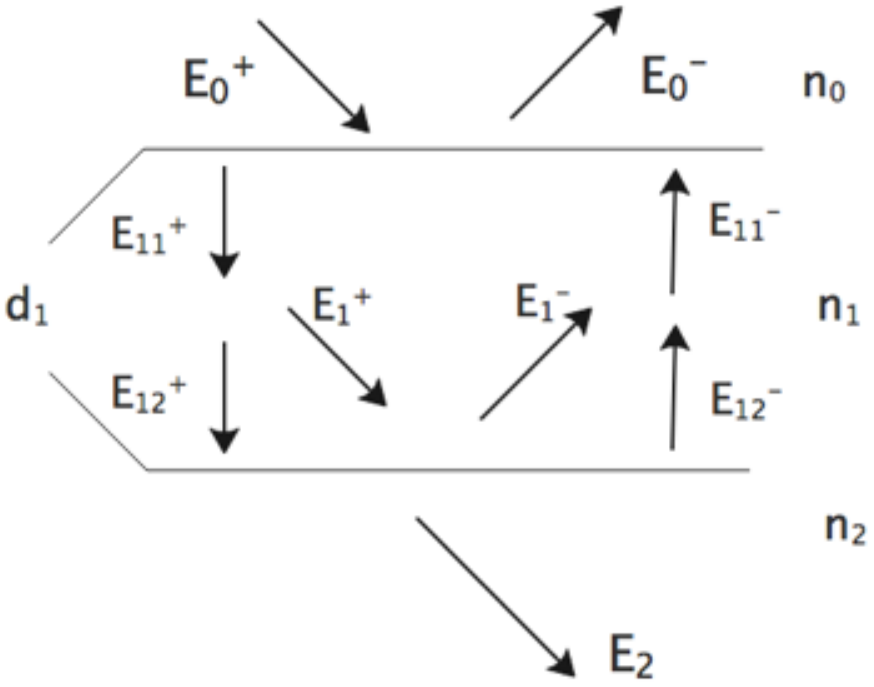

Figure 2.1: Electromagnetic pass through single layer film. The supersripts of + and - means the different propagation directions. The superscripts of 0, 1 and 2 means the layer state,and 11 and 12 means the interface state.

The figure shows that the electromagnetic wave E_0 turned to E_2 after passing through the AR. E_1 represents the status of electromagnetic wave in the layer. E_{11}^+, E_{12}^- represent the instantaneous state of the field which just crossed the interface, and E_{11}^-, E_{12}^+ are the fields which are going to pass through the layer. Through the admittance connecting E_0 and E_2, the film can be regarded as surface of a media. The equations below can be obtained by applying boundary conditions to the first media surface n_0:

$$H_0 = Y(k \times E_0) \tag{2.1}$$

$$\begin{cases} E_0 = E_0^+ + E_0^- = E_{11}^+ + E_{11}^- \\ k \times E_0 = k \times E_{11}^+ + k \times E_{11}^- \\ H_0 = H_0^+ + H_0^- = H_{11}^+ + H_{11}^- \\ H_0 = \eta_1(k \times E_{11}^+ + k \times_{11}^-) \end{cases} \tag{2.2}$$

The difference between these two transient states in the propagation through the dielectric media

lies in the phase factor introduced due to the layer thickness [37, 70]. The phase thickness for the first interface can be derived as:

$$\begin{cases} E_{12}^{+} = E_{11}^{+} e^{-i\delta_1} \\ E_{12}^{-} = E_{11}^{-} e^{i\delta_1} \end{cases} \Rightarrow \delta_1 = \frac{2\pi}{d} N_1 d_1 \cos(\theta_1) \tag{2.3}$$

By combining Eq. (2.2) and (2.3), the matrix of the relation between n_0 and n_1 can be found as Eq. (2.4)

$$\begin{bmatrix} k \times \delta_0 \\ H_0 \end{bmatrix} = \begin{bmatrix} e^{i\delta_1} & e^{-i\delta_1} \\ \eta_1 e^{i\delta_1} & -\eta_1 e^{-i\delta_1} \end{bmatrix} \begin{bmatrix} k \times E_{12}^{+} \\ k \times E_{12}^{-} \end{bmatrix} \tag{2.4}$$

Similarly, the relationship of electric field between n_1 and n_2 can be obtained as:

$$\begin{bmatrix} k \times E_{12}^{+} \\ k \times E_{12}^{-} \end{bmatrix} = \begin{bmatrix} \frac{1}{2} & \frac{1}{2\eta_1} \\ \frac{1}{2} & -\frac{1}{2\eta_1} \end{bmatrix} \begin{bmatrix} k \times E_2 \\ H_2 \end{bmatrix} \tag{2.5}$$

Thus, the relationship between the electromagnetic field on two sides should be obtained by multiplying Eq. (2.4) and (2.5):

$$k \times E_0 \begin{bmatrix} 1 \\ Y \end{bmatrix} = \begin{bmatrix} \cos\delta_1 & \frac{i\sin\delta_1}{n_1} \\ in_j \sin\delta_{kj} & \cos\delta_1 \end{bmatrix} \begin{bmatrix} 1 \\ \eta_2 \end{bmatrix} (k \times E_2) \tag{2.6}$$

So far, the equivalent derivation from film to media surface is accomplished. If the conclusion is spread to the entire media space, the feature matrix of layer j when period number is k will be obtained as:

$$M_{kj} = \begin{bmatrix} \cos\delta_{kj} & \frac{i\sin\delta_{kj}}{n_j} \\ in_j \sin\delta_{kj} & \cos\delta_{kj} \end{bmatrix} \tag{2.7}$$

$$\delta_{kj} = \frac{2\pi n_j d_j \cos\theta_j}{\lambda} \tag{2.8}$$

In Eq. 2.8, θ_j indicates the angle of propagation in the layer j for period number of k. The

modified admittance η_j has following expressions for TE mode:

$$\eta_j = n_j \cos\theta_j \sqrt{\frac{\varepsilon_0}{u_0}} \tag{2.9}$$

The structure of designed photonic crystal is shown below:

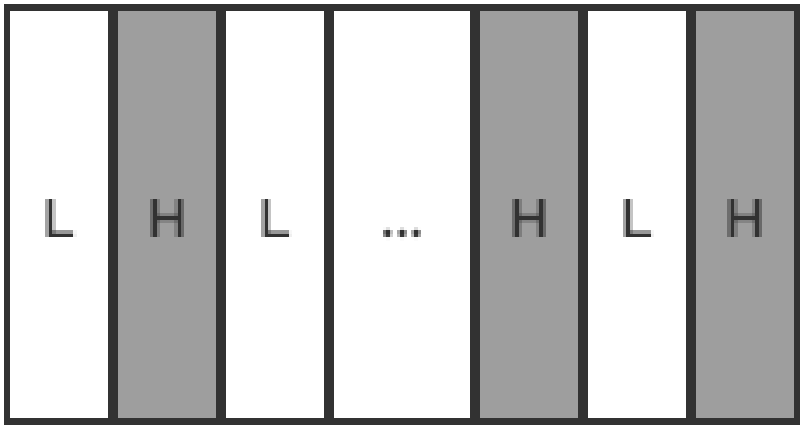

Figure 2.2: Structure sketch of 1D photonic crystal in this project. In this case, the high refractive index material is Si(3.9766) and the low index material is SiO_2(1.4585).

In Fig. 2.2, medium H and L represent Si and SiO_2 respectively. The thicknesses of both layers are set as a quarter of the wavelength for original model and will be modified in later optimization. For medium A which has complex value included, the refractive index n_j should be replaced by $\widetilde{n}_j = n_j + ki$. Therefore, the expression for transmittance can be written as:

$$T = \frac{4\eta_0\eta_{N+1}}{|\eta_0 m_{11} + \eta_0\eta_{N+1} + m_{21} + \eta_{N+1}m_{11}|^2} \tag{2.10}$$

where $M = \begin{bmatrix} m_{11} & m_{12} \\ m_{21} & m_{22} \end{bmatrix}$.

2.1.2 Spectral efficiency calculation

The spectral efficiency of optical filters is actually the ratio of energy accepted by the cell and the total energy coming to the filters [71, 72]. In this sub-chapter, the simulation model is briefly described. The optical filters of multilayer structures with two media are built between

hot body (in this case, blackbody) and TPV cell (in this case GaSb cell). Since the blackbody is assumed as the heat source in the thermophotovoltaic system, the refractive index n_{BB} equals to 1. The radiation power which is accepted by the GaSb cell $P_{radiation}$ can be expressed as[26]:

$$\begin{aligned} &P_{Rad} = P_{Tot} - P_{Ref} \\ &= \int_0^\infty \frac{n_{BB}^2 \omega^3 \hbar}{4\pi^2 c^2 exp\left(\frac{\hbar\omega}{kT_{BB}}\right)-1} \bar{T_{BC}}(\omega)\, d\omega - \int_{\omega_{gap}}^\infty \frac{n_{PV}^2 \omega^3 \hbar}{4\pi^2 c^2 exp\left(\frac{\hbar\omega - eV}{kT_{PV}}\right)-1} \bar{T_{CB}}(\omega)\, d\omega \end{aligned} \tag{2.11}$$

where $\overline{T_{BC}}(\omega)$ is the transmittance from the black body to the cell, and is given by

$$\overline{T_{BC}}(\omega) = \int_0^{\theta_X} \{T_{BC\_TE}(\omega,\theta) + T_{BC\_TM}(\omega,\theta)\} \cos(\theta) \sin(\theta)\, \mathrm{d}\,\theta \tag{2.12}$$

Similarly, the expression for $\overline{T_{CB}}(\omega)$, which is the transmittance from cell to black body is:

$$\overline{T_{CB}}(\omega) = \int_0^{\theta_X} \{T_{CB\_TE}(\omega,\theta) + T_{CB\_TM}(\omega,\theta)\} \cos(\theta) \sin(\theta)\, \mathrm{d}\,\theta \tag{2.13}$$

The power generated by the TPV system equals the photon flux from black body to the cell minus the part which is reflected back to the black body:

$$P_{Gen} = eV \left(\int_{\omega_{gap}}^\infty \frac{n_{BB}^2 \omega^2}{4\pi^2 c^2 exp\left(\frac{\hbar\omega}{kT_{BB}}\right)-1} \bar{T_{BC}}(\omega)\, d\omega - \int_{\omega_{gap}}^\infty \frac{n_{PV}^2 \omega^2}{4\pi^2 c^2 exp\left(\frac{\hbar\omega - eV}{kT_{PV}}\right)-1} \bar{T_{CB}}(\omega)\, d\omega \right\} \tag{2.14}$$

The system efficiency η_{sys} can be obtained as P_{gen} divided by P_{rad} [26, 73]. To calculate the spectral efficiency, it is assumed that all the power transmitted to the cell with larger photon energy than the bandgap of GaSb cell (i.e. $0.7eV$) can be converted to electricity, so the transmittance of these photons will ideally be 1. All other photons should be reflected back to the emitter, i.e. the transmittance for them will ideally be 0. The expression for the spectral efficiency can then be written as:

$$\eta_{Spe} = \frac{\int_{\omega_{gap}}^\infty \frac{{n_{BB}}^2 \omega^3 \hbar}{4\pi^2 c^2 exp\left(\frac{\hbar\omega}{kT_{BB}}\right)-1} \bar{T_{BC}}(\omega)\, d\omega}{\int_0^\infty \frac{{n_{BB}}^2 \omega^3 \hbar}{4\pi^2 c^2 exp\left(\frac{\hbar\omega}{kT_{BB}}\right)-1} (1 - \bar{R_{BC}})(\omega)\, d\omega} \tag{2.15}$$

In numerical calculations the limits of the integrals were approximated, with 0 and infinity replaced by frequencies corresponding to wavelengths of $6\mu m$ and $0.5\mu m$ respectively.

2.1.3 Plane Wave Expansion method(PWE)

The study of the energy bands of photonic crystals of various specific structures and their transmission properties is extremely promising and valuable for fundamental research. The plane-wave expansion method is one of the effective methods to study the energy band structure of photonic crystals. In this subsection, the eigen equations of electromagnetic waves in photonic crystals are derived by the plane wave expansion method (PWE), starting from the Maxwell system of equations [26, 74]. Suppose that in A photonic crystal, no net charge exists and the current is zero, according to Maxwell's equations:

$$\begin{aligned} &\nabla \cdot D = 0 \\ &\nabla \cdot B = 0 \\ &\nabla \times E = -\frac{\partial B}{\partial t} \\ &\nabla \times H = \frac{\partial D}{\partial t} \end{aligned} \tag{2.16}$$

In Eq. (2.16), D is the electric displacement vector, B is the magnetic induction vector, E and H are the electric and magnetic fields respectively. Assuming that there is only A linear relation between D and E, ignoring higher order terms, and the medium is non-magnetic, the equation can be written:

$$\begin{cases} D = \varepsilon_0 \varepsilon(r) E \\ B = \mu_0 H \end{cases} \tag{2.17}$$

where ϵ_0 and μ_0 are dielectric constant and permeability respectively, $\epsilon(r)$ is relative dielectric constant, which is the function of space location r. While E and H are normally complex functions of time and space, the electric intensity vector and magnetic intensity vector can be transferred into simple harmonic mode considering monochromatic electromagnetic waves with the time-harmonic characteristic $e^{i\omega t}$ at a particular frequency ω :

$$\begin{cases} E(r,t) = E(r)e^{i\omega t} \\ H(r,t) = H(r)e^{i\omega t} \end{cases} \tag{2.18}$$

The following equation can be obtained from Eq. (2.16) and (2.18):

$$e^{i\omega t}\nabla \times E(r) = -\frac{\partial B}{\partial t} = -\mu_0 \frac{\partial (H(r) \cdot e^{i\omega t})}{\partial t} \tag{2.19}$$

Then the equation below can be derived:

$$\nabla \times E(r) = -i\omega\mu_0 H(r) \tag{2.20}$$

Similarly, the following equation is given for the magnetic field H:

$$\nabla \times H(r) = -i\omega\varepsilon_0\varepsilon(r)E(r) \tag{2.21}$$

Applying $\nabla\times$ to Eq. (2.20) and using Eq. (2.21) there, the equation of electric intensity vector $E(r)$ can be found:

$$\nabla \times \nabla \times E(r) = \mu_0\varepsilon_0\varepsilon\,(r)\,\omega^2 E(r) \tag{2.22}$$

where ω^2 is its eigenvalue. Since $\mu_0\epsilon_0 = \frac{1}{c^2}$, the equation can be written as:

$$\frac{1}{\varepsilon(r)}\nabla \times \nabla \times E(r) = \frac{\omega^2}{c^2}E(r) \tag{2.23}$$

Using a similar procedure for Eq. (2.21) and (2.20), the following relationship between magnetic field and dielectric constant is:

$$\nabla \times \frac{1}{\varepsilon(r)}\nabla \times H(r) = \frac{\omega^2}{c^2}H(r) \tag{2.24}$$

Now the eigenequations for electric and magnetic field of photonic crystals have been obtained. Denoting $\Theta_E = \frac{1}{\varepsilon(r)}\nabla \times \nabla\times$, $\Theta = \nabla \times \frac{1}{\varepsilon(r)}\nabla\times$, the equation can be derived as:

$$\begin{cases} \Theta_E E(r) = \frac{\omega^2}{c^2}E(r) \\ \Theta H(r) = \frac{\omega^2}{c^2}H(r) \end{cases} \tag{2.25}$$

Here, Θ is linear differential operator and $H(r)$ is eigenvector of magnetic field. It is important to mention that all the linear combinations of solutions to $H(r)$ are solutions to eigenequations. To solve the eigenequations, the magnetic intensity vector should be expanded as a superposition of plane waves:

$$H(r) = \sum_{k,\lambda} \widehat{e}(k,\lambda)h(k,\lambda)e^{ik\cdot r} \tag{2.26}$$

where $\widehat{e}(k,\lambda))$ represents the Unit vector in two orthogonal polarization directions of a plane wave with wave vector k, and $\widehat{e}(k,1),\widehat{e}(k,2),k$ make the right-handed helix system ($k\cdot\widehat{e}(k,\lambda)=0$), and $h(k,\lambda)$ stands for amplitude in the direction of $\widehat{e}(k,\lambda)$). Using the notation[56]:

$$f(r)=\frac{1}{\varepsilon(r)} \tag{2.27}$$

If $\epsilon(r)$ is periodic function, $f(r)$ must be periodic function as well. so $f(r)$ can be expanded in k space:

$$f(r)=\sum_{G} f(G)e^{iG\cdot r} \tag{2.28}$$

According to Eq. (2.27) and (2.28),

$$\begin{aligned}
&\nabla\times\left[\tfrac{1}{\varepsilon(r)}\nabla\times H(r)\right]=\textstyle\sum_{G,K,\lambda}\left[\nabla\times f(G)ik\times\widehat{e}(k,\lambda)\right]h(k,\lambda)e^{i(k+G)\cdot r}\\
&+\textstyle\sum_{G,k,\lambda}h(k,\lambda)e^{i(k+G)\cdot r}i(k+G)\times f(G)ik\times\widehat{e}(k,\lambda)\\
&=\textstyle\sum_{G,k,\lambda}-(k+G)\times f(G)[k\times\widehat{e}(k,\lambda)]h(k,\lambda)e^{i(k+G)\cdot r}
\end{aligned} \tag{2.29}$$

Put the equation above in Eq. (2.24) gives:

$$\sum_{G,k,\lambda}-(k+G)\times f(G)\left[k\times\widehat{e}(k,\lambda)\right]h(k,\lambda)e^{i(k+G)r}=-\left(\tfrac{\omega}{2}\right)^2\sum_{k,\lambda}\widehat{e}(k,\lambda)h(k,\lambda)e^{ikr} \tag{2.30}$$

This equation can be multiplied by $\widehat{e}(k,\lambda)e^{ikr}$), and simplified as:

$$\sum_{G,k,\lambda}k'\times f(G)\left[(k'-G)\times\widehat{e}(k'-G,\lambda)\right]\cdot\widehat{e}(k'.\lambda')h(k,\lambda)=-\left(\tfrac{\omega}{C}\right)^2\sum_{k,\lambda}\widehat{e}(k',\lambda)\cdot\widehat{e}(k',\lambda')h(k',\lambda) \tag{2.31}$$

Considering that $\widehat{e}(k',\lambda)\widehat{e}(k,\lambda')=\varepsilon_{\lambda\lambda'}$', the equation above can be further simplified as:

$$\sum_{G,k,\lambda}k'\times f(G)\left[(k'-G)\times\widehat{e}(k'-G,\lambda)\right]\cdot\widehat{e}(k',\lambda')h(k,\lambda)=-\left(\frac{\omega}{C}\right)^2h(k',\lambda') \tag{2.32}$$

By replacing k' with $k+G'$, Eq. (2.32) can be transformed as:

$$\sum_{G,k,\lambda}(k+G')\times f(G)\left[(k+G'-G)\times\widehat{e}(k+G'-G,\lambda)\right]\cdot\widehat{e}(k+G',\lambda')h(k,\lambda)=-\left(\frac{\omega}{C}\right)^2 h(k+G',\lambda') \tag{2.33}$$

And replacing $G'-G$ with G'',

$$\sum_{G,k,\lambda}\widehat{e}(k+G',\lambda')\cdot\left\{(k+G')\times f(G'-G'')\left[(k+G'')\times\widehat{e}(k+G'',\lambda)\right]\right\}h(k+G'',\lambda)=-\left(\frac{\omega}{C}\right)^2 h(k+G',\lambda') \tag{2.34}$$

Then make the replacements according to the following rules: change G' into G, G'' into G', λ' into λ, λ intoλ' [75, 76]:

$$\sum_{G,k,\lambda}\widehat{e}(k+G,\lambda)\cdot\left\{(k+G)\times f(G-G')\left[(k+G')\times\widehat{e}(k+G',\lambda')\right]\right\}h(k+G',\lambda')=-\left(\frac{\omega}{C}\right)^2 h(k+G,\lambda) \tag{2.35}$$

This expression can be simply regarded as:$A\cdot(B\times C\times D)=(A\times B)\cdot(C\times D)$. Therefore,

$$\begin{aligned}&\widehat{e}(k+G,\lambda)\left\{(k+G)\times[(k+G')\times\widehat{e}(k+G',\lambda')]\right\}=[\widehat{e}(k+G,\lambda)\times(k+G)]\cdot[(k+G')\times\widehat{e}(k+G',\lambda')]\\&=-[(k+G)\times\widehat{e}(k+G,\lambda)]\cdot[(k+G')\times\widehat{e}(k+G',\lambda')]\end{aligned} \tag{2.36}$$

Using the above equation in Eq. (2.35), the equation can be obtained as:

$$\sum_{G,k,\lambda}[(k+G)\times\widehat{e}(k+G,\lambda)]\cdot\left[(k+G')\times\widehat{e}(k+G',\lambda')\right]f(G-G')h(k+G',\lambda')=\left(\frac{\omega}{C}\right)^2 h(k+G,\lambda) \tag{2.37}$$

Eq. (2.37) is the eigen equation $h(k+G,\lambda)$. For a given k, the elements of eigen matrix Θ of $h(k+G,\lambda)$ are:

$$\Theta^k_{\lambda,G,\lambda',G'}=[(k+G)\times\widehat{e}(k+G,\lambda)]\cdot\left[(k+G')\times\widehat{e}(k+G',\lambda')\right]f(G-G') \tag{2.38}$$

The structure of the matrix can be shown to be follows as:

$$\begin{pmatrix} \Theta^k_{\lambda_1,G_1,\lambda_1,G_1} & \Theta^k_{\lambda_1,G_1,\lambda_2,G_1} & \Theta^k_{\lambda_1,G_1,\lambda_1,G_1} & \Theta^k_{\lambda_1,G_1,\lambda_2,G_1} & \cdots & \Theta^k_{\lambda_1,G_1,\lambda_2,G_N} \\ \Theta^k_{\lambda_2,G_1,\lambda_1,G_1} & \Theta^k_{\lambda_2,G_1,\lambda_2,G_1} & \Theta^k_{\lambda_2,G_1,\lambda_1,G_1} & \Theta^k_{\lambda_2,G_1,\lambda_2,G_1} & \cdots & \Theta^k_{\lambda_1,G_1,\lambda_2,G_N} \\ \Theta^k_{\lambda_1,G_1,\lambda_1,G_1} & \Theta^k_{\lambda_2,G_1,\lambda_2,G_1} & \Theta^k_{\lambda_1,G_1,\lambda_1,G_1} & \Theta^k_{\lambda_1,G_1,\lambda_2,G_1} & \cdots & \Theta^k_{\lambda_1,G_1,\lambda_2,G_N} \\ \Theta^k_{\lambda_2,G_1,\lambda_1,G_1} & \Theta^k_{\lambda_2,G_1,\lambda_2,G_1} & \Theta^k_{\lambda_2,G_1,\lambda_1,G_1} & \Theta^k_{\lambda_2,G_1,\lambda_2,G_1} & \cdots & \Theta^k_{\lambda_1,G_1,\lambda_2,G_N} \\ \vdots & \vdots & \vdots & \vdots & \ddots & \vdots \\ \Theta^k_{\lambda_2,G_N,\lambda_1,G_1} & \Theta^k_{\lambda_2,G_N,\lambda_2,G_1} & \Theta^k_{\lambda_2,G_N,\lambda_1,G_1} & \Theta^k_{\lambda_2,G_N,\lambda_2,G_1} & \cdots & \Theta^k_{\lambda_2,G_N,\lambda_2,G_N} \end{pmatrix} \tag{2.39}$$

which means, in the photonic crystal which has N primitive cells (the number of reciprocal lattice vectors is N), for every given k, its eigen matrix possesses $2N \times 2N$ elements and its eigen value is $\left(\frac{\omega}{C}\right)^2$. However, the eigenvalue problem described above is an infinitely large matrix and cannot be solved completely. In order to solve this problem, some approximation is required, for example taking a sufficient number of inverse lattice vectors to represent the full analytic solution. If a number N of inverse lattice vectors is taken, the problem is simplified as an eigenvalue calculation of an N x N matrix which is more appropriate to solve by computer. Once the eigenvalues and eigenvectors of the matrix have been found, the energy band structure of the photonic crystal and the corresponding spatial distribution of the eigenfields can be obtained.

2.2 Fabrication defects

2.2.1 Derivation of complex refractive index

One dimensional photonic crystal is a periodic array of layers and the refractive index of the material changes periodically in one direction[77, 78]. To show the decrement of transmission electromagnetic waves, complex refractive index is introduced to illustrate the optical performance of 1D PhC and some other important parameters. Considering the absorption of light in the medium, the optical performance can be described via two parameters, i.e. refractive index n and absorptivity a [79]. If it is assumed that the light transmits in the transparent medium which has no absorption, the plane wave function along the x direction will be:

$$\widetilde{E}(x,t) = A_0 e^{i(\omega t - kx)} \tag{2.40}$$

Similarly, the attenuation of light along the transmission length in the absorbing medium is:

$$I(x) = I_0 e^{-ax} \tag{2.41}$$

The relationship between light intensity and amplitude can be written as:

$$I(x) = A^2(x) \tag{2.42}$$

Therefore, the following equation can be obtained:

$$A(x) = A_0 e^{-\frac{a}{2}x} \tag{2.43}$$

Then, the wave in the medium can be written as:

$$\widetilde{E}(x,t) = A_0 e^{i(k-\frac{a}{2})x} \cdot e^{-i\omega t} = A_0 e^{-i\omega t} e^{i\widetilde{k}x} \tag{2.44}$$

where $\widetilde{k}$ is the complex wave vector $\widetilde{k} = k + i\frac{a}{2}$. The relationship between real wave vector and refractive index is:

$$k = \frac{2\pi}{\lambda} = \frac{\omega}{v} = \frac{\omega}{\frac{c}{n}} = \frac{\omega n}{c} \tag{2.45}$$

Therefore,

$$\widetilde{k} = \frac{\omega}{c}(n + i\frac{c\alpha}{2\omega}) = \frac{\omega}{c}\widetilde{n}, \tag{2.46}$$

where $\widetilde{n}$ is the complex refractive index, where the imaginary part reflects the absorption of medium. The complex refractive index can be simply written as:

$$\widetilde{n} = n + i\frac{c\alpha}{2\omega} \tag{2.47}$$

The imaginary part reflects the absorption of medium. The complex refractive index can be simply written as:

$$\widetilde{n} = n + ik \tag{2.48}$$

where n is the real part of the refractive index of absorbing medium, which depends on the speed of light through the medium; the imaginary part describes the attenuation of light in the medium. However, in the simulation of multi-layer structure filters, the symbol in front of the imaginary part should be negative. This is because the relationship between angular frequency ω and wave factor k is:

$$k = n\frac{\omega}{c} \tag{2.49}$$

The value of k should be complex in case of complex refractive index. This leads to both real and imaginary exponential change of the plane wave (x, t)

$$f(x,t) = e^{i(kx-\omega t)} = e^{i((k_{real}+k_{imag})x-\omega t)} = e^{-k_{imag}x} \cdot e^{i(k_{real}x-\omega t)} \tag{2.50}$$

The expression of plane wave $f(x, t)$ shows the transmission direction from negative to positive. Since the absorption would happen in the transmission process, the values of x should be mostly positive because of the decrease of signal, which means the exponential dependence $e^{-k_{imag}x}$ should be decaying. So the wave vector k_{imag} should be positive.

2.2.2 Effects of interface roughness

To calculate the transmission/reflection coefficient of a multi-layer structure we use the Transfer Matrix Method [80]. The field components of outgoing and incident electromagnetic waves are related via the transfer matrix. This is calculated from interface matrices and layer matrices for the structure [37, 81]. The interface matrix is:

$$I_{ij} = \frac{1}{t_{ij}} \begin{bmatrix} 1 & r_{ij} \\ r_{ij} & 1 \end{bmatrix}, \tag{2.51}$$

where r_{ij} and t_{ij} are reflection and transmission coefficients of interface ij, respectively, themselves derived from Fresnel equations. For TE modes, r_{ij} and t_{ij} are:

$$\begin{cases} r_{ij} = \frac{q_i - q_j}{q_i + q_j} \\ t_{ij} = \frac{2q_i}{q_i + q_j} \end{cases} \tag{2.52}$$

and for TM modes they are:

$$\begin{cases} r_{ij} = \frac{\widetilde{n}_j^2 q_i - \widetilde{n}_i^2 q_j}{\widetilde{n}_j^2 q_i + \widetilde{n}_i^2 q_j} \\ t_{ij} = \frac{2\widetilde{n}_i^2 \widetilde{n}_j^2 q_i}{\widetilde{n}_j^2 q_i + \widetilde{n}_i^2 q_j} \end{cases}, \tag{2.53}$$

where q_i is the optical admittance of layer i:

$$q_i = \sqrt{\widetilde{n}_i^2 - \eta_0^2 sin\phi_0}, \tag{2.54}$$

where $\widetilde{n}_i$ is the refractive index of layer i, η_0 is the refractive index of air ($\eta_0 = 1$) and ϕ_0 is the incidence angle [82, 83]. For non-absorbing medium, the transfer matrix through the medium only changes the phase of the propagating wave, so it can be written as:

$$L_i = \begin{bmatrix} e^{-i\xi_i d_i} & 0 \\ 0 & e^{i\xi_i d_i} \end{bmatrix}, \tag{2.55}$$

where $\xi_i d_i$ is layer phase thickness, which gives the phase change of electromagnetic wave transmission through layer i. Here, $\xi_i = 2\pi q_i/\lambda$. With all the interface and layer matrices set, the total system transfer matrix S can be obtained as:

$$S = \begin{bmatrix} S_{11} & S_{12} \\ S_{21} & S_{22} \end{bmatrix} = \left(\prod_{n=1}^{m} I_{n(n-1)} L_n \right) \bullet I_{m(m+1))} \tag{2.56}$$

Finally, the total amplitude reflection and transmission coefficients r and t for light coming from the left are [33]:

$$\begin{cases} r = \frac{E_0^-}{E_0^+} = \frac{S_{21}}{S_{11}} \\ t = \frac{E_{M+1}^+}{E_0^+} = \frac{1}{S_{11}} \end{cases} \tag{2.57}$$

The above expressions are valid for perfectly flat multi-layer structures. In reality, the thin films cannot be perfectly flat due to limitations of growth techniques. Thus, interface roughness should be included to achieve a more realistic model. With interface roughness present, for non-absorbing media:

$$\begin{cases} r_{ij} = -r_{ji} \\ t_{ij} t_{ji} - r_{ij} r_{ji} = 1 \end{cases}, \tag{2.58}$$

and Eq. 2.51 is written as:

$$I_{ij} = \frac{1}{t_{ij}} \begin{bmatrix} 1 & -r_{ji} \\ r_{ij} & t_{ij}t_{ji} - r_{ij}r_{ji} \end{bmatrix}, \tag{2.59}$$

where r_{ji} and t_{ji} are the complex Fresnel reflection and transmission coefficients at interface ji, initially calculated from Eq. 2.52 and 2.53, but then modified to include the effects of roughness. The modified coefficients at the ij-th rough interface, with a random Gaussian distribution of interface height, with the root mean square denoted as Z, are [37]:

$$\begin{cases} r_{ij} = r_{ij}^0 exp[-2(sn_m\sigma)^2] \\ r_{ji} = r_{ji}^0 exp[-2(sn_{m+1}\sigma)^2] \\ t_{ij} = t_{ij}^0 exp[-\frac{(s\sigma)^2(n_{m+1}-n_m)^2}{2}] \\ t_{ji} = t_{ji}^0 exp[-\frac{(s\sigma)^2(n_m-n_{m+1})^2}{2}] \end{cases} \tag{2.60}$$

Here, the superscript 0 denotes the reflection or transmission coefficients for an ideal interface,$\sigma = 1/\lambda$, and $s = 2\pi Z$.

2.3 Optimisation solution

2.3.1 Genetic Algorithm(GA)

The interest in Genetic Algorithm applications in searching for the best global value for some mathematical problems has been increasing [1]. When it comes to some practical issues, like the research target of this report, physical parameters of photonic crystals, the algorithm is also known to cope well with the optimization designs or searching for the minimum value among whole population of data [84–86]. The research group in Toyama University proposed that Genetic algorithm can be used to tackle optimization with complex variables involved [87]. Since the project involves one material with nonzero imaginary part of its refractive index, it indicates that the imaginary part of material in the filtered system can be also optimized using this mathematical algorithm.

However, in accordance with results of the previous research progress, GA optimization of layer thicknesses makes the stack change from periodic to non-periodic for achieving higher average transmittance. It is also pointed out that aperiodic design has better thermal emission

performance than periodic structure and has smaller total layer thickness [88]. The remaining issue is to use Genetic algorithm to optimize the width of each thin film in the stack for both normal and aperiodic arrangement and compare their thermal performance.

This section aims to give the optimization results of Genetic algorithm in calculating width of each layer among different structures and the best value of refractive index of Silicon. The research methods included are pattern search algorithm, transfer matrix method and genetic algorithm. The calculation outcome, shown in the form of tables, figures and screenshots, reveals that aperiodic structures have better optical performance in transmittance and high narrowband peak of emissivity.

Two different structures are introduced by following other research groups' progress. One of the papers gives an idea of using pattern search algorithm [89] to optimize the structure of one-dimensional photonic crystals. In this research, three different structures are simulated using PS algorithm and improvement can be clearly seen. PS method is a direct search method that explores and moves the current search point according to a fixed pattern and step size in order to find a feasible descent direction (non-fastest descent direction) [90, 91]. The step size increases and next iteration starts at this moment if the improvement point is located in iteration process; otherwise, the step size decreases and searching will continue afterwards.

Compared to PS, Genetic Algorithm has the fast-random global search ability. Genetic algorithm is a search algorithm used to solve optimization in computational mathematics[86, 92]. The evolutionary algorithm was originally developed based on some Biology phenomena which include genetics, mutations, natural selection and hybridization, etc. In this optimization part, GA algorithm is applied to calculate the best individuals of layer thickness of 1D photonic crystal. The process of Genetic Algorithm can be illustrated as follows:

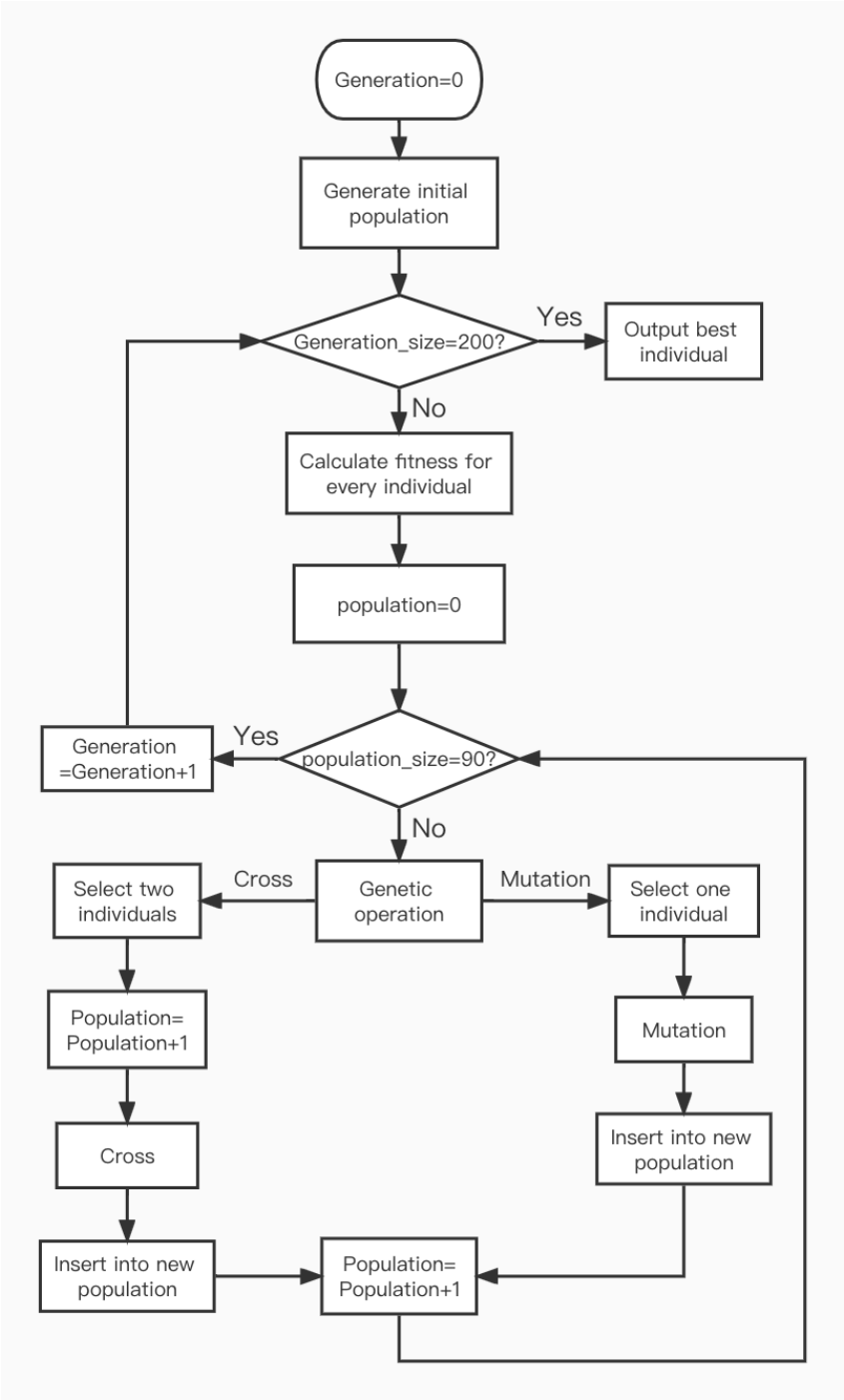

Figure 2.3: Flow chart of Genetic algorithm process. The process can be simply splited into: initialization, decode, calculation of fitness, selection, cross and mutation.

First, target function needed to be established. In this project, the goal function is transmittance of 1-D PhC. Besides, this is also fitness function in the algorithm. The optimization of layer thickness is also based on the calculations. Since complex refractive index is considered in the program, better optical performance means less thickness so there will be less absorption in transition through the stack. Fitness function is set to determine if each chromosome is better

than its father generation [93, 94]. In this case, it is a function that uses optical constant and film thickness as independent variables. Thus, the optimisation of layer thickness can be transferred to evaluation of calculation results of transmittance. The target function can be expressed as:

$$T' = \sqrt{\frac{1}{n}\sum_{i=1}^{n}(T_e(\lambda, d) - T(\lambda_i, d))^2} \tag{2.61}$$

where $T(\lambda_i, d)$ is the calculation results of transmittance and $T_e(\lambda, d)$ can be simply regraded as 1 at reference wavelength. The number of sampling points n is 501 and the range of wavelength varies from 350 to 2000 nm. This function is designed to calculate the difference between calculation and original values. More precise results will be obtained if smallest difference can be seen, which means the optimisation of layer thickness reaches its best value.

Then the limitation of searching population generation quantities should be set. This value should not be too large, to save calculation time. The population size is set as 90 since the input variable also includes 90 incidence angles. The next step is to produce initial population. N binary numbers will be developed in the whole group, which are the individuals of the initial population. This depends on calculation precision. Considering the running time of the whole program and the balance between time and precision, the chromosome size is finally set as 20. The possible range of chromosome size should be 8- 40. By using the following restriction to determine 20 as the best chromosome size:

$$2^{19} < (90 - 0) \times 10000 < 2^{20} \tag{2.62}$$

Where 90 and 0 are the upper and lower boundaries of the variable and 10000 means that the decimal part has 4 digits. After that, the fitness function should be used to calculate the best individual and next generation is produced. The generation size is set as 200, because it will achieve smaller progress if the final searching converges[95, 96], and that will be a huge waste of time.

2.3.2 Layer thickness optimisation

At the initial stage, pattern search algorithm is selected to optimise the layer thickness of 10-layer structure. The introduction of imaginary part means the loss of light transmission through

the material. By comparing the two algorithm calculation results in Table 2.1, it is obvious that the algorithms are likely to set the stack as aperiodic structure to achieve better performance. [88] This will be the focus of the discussion in the following chapters.

Table 2.1: Thickness optimization of PS and GA.

	L	H	L	H	L	H	L	H	L	H
Original/nm	82.276	30.174	82.276	30.174	82.276	30.174	82.276	30.174	82.276	30.174
PS/nm	73	2.8	8.3	30	77.5	27.5	75.8	27.7	81.4	0.4
GA/nm	72.283	2.8288	8.3107	26.968	77.4558	27.5338	75.7936	27.7224	81.4449	0.3772

By comparing the layer thicknesses obtained by different optimisation methods, small difference can be found. This means that the values are approaching the smallest value to achieve high transmittance. When the three curves of transmittance are plotted in a single figure (Figure 2.4), main peaks of Genetic algorithm and pattern search method have slightly moved towards long wavelength direction. However, the average transmittance increases when the main peak value decreases between the original and modified models.

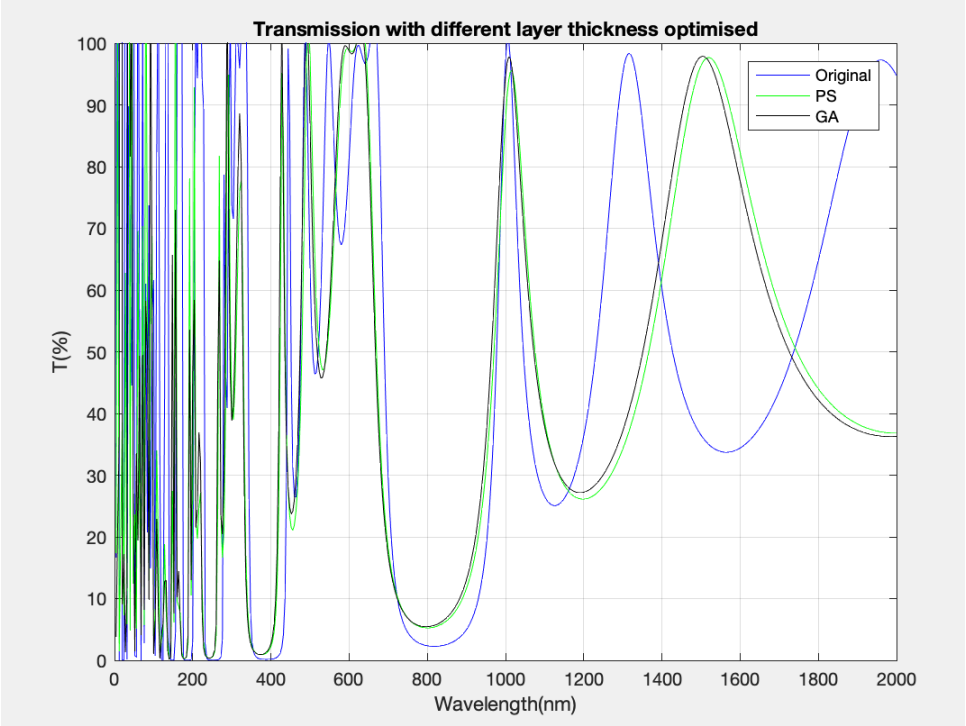

Figure 2.4: Transmittance with different layer thickness optimisation methods. The blue curve is the original. The green curve is layer thickness optimized using pattern search. The black curve is layer thickness optimized using genetic algorithm.

To cope with complicated aperiodic curves, GA is a good method to search for the minimum value. It has different outcome of the fourth layer, 26.968nm, when the result of PS is 30nm.

This is mainly because pattern search stops when it meets the best value which may not be the best among the whole group [90, 97, 98]. GA guarantees that each iteration will involve same chromosome size, in this case, i.e. 90. It uses random selection algorithm to choose 90 chromosomes each time. They may not be the first 90 among the generation so that less good individuals escape from the filtering. The key point is that not the best 90 individuals are winners because some individuals may have better mutation afterwards and then turn to be best individuals in the following iterations [73, 99]. However, due to the consideration of calculation time and huge amount of data involved, the generation size has to be a number which is not too large. Sometimes the codes stop searching earlier because of small mutation rate. The outcome may not be the best in the group. On the other hand, too big rate will cause unstable errors. In addition, when it comes to the later period of searching, most chromosomes are very similar, the algorithm will still give low efficiency and local optimum. So, it is also vital to set the parameters initially.

2.3.3 Searching optimal imaginary part

In the previous work, the refractive index of Si and SiO_2 are taken according to the paper [100]. The complex refractive index is $3.9766+0.030209i$ in accordance with the following figure. At this moment, the real and imaginary parts of dielectric constant are 15.813 and 0.24026 respectively. The absorption coefficient is $6460.5(cm)^{-1}$. Optimization will be done in this part to make the refractive index more suitable for these applications. For example, by using Genetic Algorithm, the imaginary part can be optimized to calculate the highest transmittance in a particular wavelength range. Also, the calculation result can be applied afterwards to test high emissivity at a specific frequency. Since complex index is involved in multilayer system, a little change of the imaginary part may result in a significant difference of the final result. If the refractive index is modified, the length of light transmission will be influenced and leads to the change of light phase [101]. It is known that absorption coefficient is given by the following equation:

$$\alpha = 2\pi k/\lambda \tag{2.63}$$

Only if the absorption through the layers is not too large, which means imaginary part is nonzero, will the results show positive effect. In this situation, the maximum thickness of layer d_{max} can

be used to determine the range of alpha $\alpha following the equation below : Here, the restriction of 0.2 is a reasonable$ and d_{max}. For example, the maximum layer thickness is 82.276 nm, the range of α can be restricted as no more than 0.00243. By using Eq. (2.63), the maximum value of k can be calculated as 0.4836. Since the range of k can be determined, it is interesting to use GA to calculate the best individual in this group for higher transmittance. From Figure 2.5, comparing to the previous data, the spectral efficiency has increased with the decrease of imaginary part. This means that the optimization of imaginary part helps to achieve better TPV performance using GA.

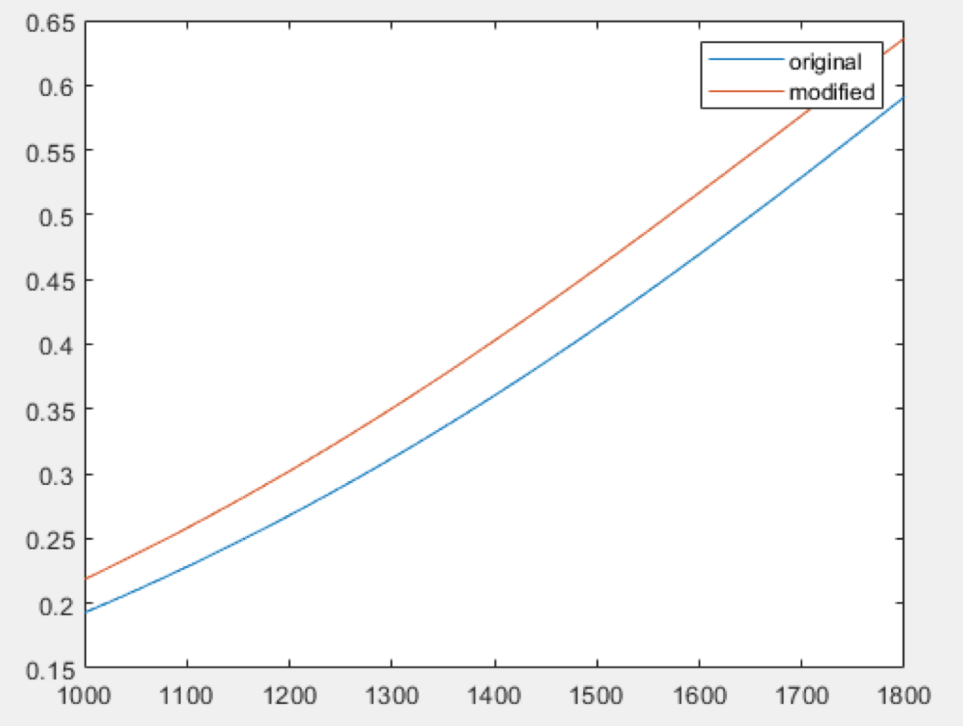

Figure 2.5: Spectral efficiency vs black body temperature. Blue curve is the original and red one is the layer thickness modified structure using GA.

For semiconductors, the product of energy gap and refractive index n^4 is constant. The materials of multilayer structure in this report are Silicon and SiO_2, which are also conventional materials for semiconductors. An idea occurred that if the refractive index is modified, especially the modification of imaginary part, better optical characteristics may be achieved. However, the introduction of complex RI means that the research is focused on the light absorption when transmitting through the layers. Suitable optimization method should be selected to make sure the imaginary part is reasonable.

2.4 Conclusion and further expectations

This chapter briefly describes the methods to build 1D and 2D photonic crystals using transfer matrix and plane wave expansion methods. The fabrication defects of complex refractive index and interface roughness are also introduced and the simulation methods are included. Genetic algorithm is the solution to most of the optimizations. It is especially used in optimizing the layer thickness and the imaginary part of refractive index. The optimization of layer thickness in this chapter is calculating optimal transmittance and derive the spectral efficiency using calculated results. This may not be the optimum unless the calculations of optimal spectral efficiency is also given and compared. The discussions on different optimization targets of the algorithm will be given in the following sections.

Chapter 3

1-D aperiodic thermal emitter

This chapter describes the application of one-dimensional photonic crystals in the application of thermal emitters. Using genetic algorithm to optimise a non-periodic structure and comparing it separately with a periodic structure before and after optimisation, it is concluded that a non-periodic 1D photonic crystal emitter can achieve the same high emissivity with a smaller total thickness of the films as a periodic structure with more layers.

3.1 Overview

Photonic crystals are dielectric materials with alternating refractive indices at periodic intervals. One-dimensional photonic crystals can be used to control the transmission and reflection properties of thermal radiation in a single direction due to their simple processing and easily controlled structure. An 1D periodic silver/tungsten emitter is introduced exhibiting excellent selective emission characteristics [102]. Using transfer matrix method, the 11-layer stack is built with one layer participating in emission and the remaining acting as filters. The structure shows enhanced emissivity similar to 3D photonic crystal but is easier to fabricate.

A 7-layer aperiodic structure of Si and SiO_2 is introduced to achieve high emissivity for narrow-band thermal emission. The paper gives comparison between 7-layer aperiodic and multilayer periodic structures. Research results reveal that, to achieve the same emission peak, periodic stack features several spurious peaks in the emission spectrum[88]. With the increase of number of layers, the total layer thickness shows a faster growth than in aperiodic structure. From Table 3.1 and the data given in this paper, if the extra emission peaks are eliminated by decreasing

the number of layers, the main peak value reduces as a result, which can be perfectly avoided by application of aperiodic structure.

Table 3.1: Summary of periodic and aperiodic stacks [88].

No.layers	$t_{total}(\mu m)$	f_{center}	$\|\varepsilon\|$	$Adj.^a f_{center}$	$Adj.^a\|\varepsilon\|$
7^b	3.92%	70.3	0.97	95.5	0.15
15	11.37	70.6	0.93	74.8	0.56
17	12.81	70.3	0.98	73.7	0.65
19	14.26	70.1	0.99	72.9	0.74

* Nearest unwanted adjacent emission peak.

** Proposed aperiodic design.

Although most of the research on improving thermophotovoltaics characteristics is focused on periodic arrayed stacks, aperiodic arrangement is simulated to see if higher thermal performance will be obtained. The flowchart of research process can be briefly described in Fig. 3.1:

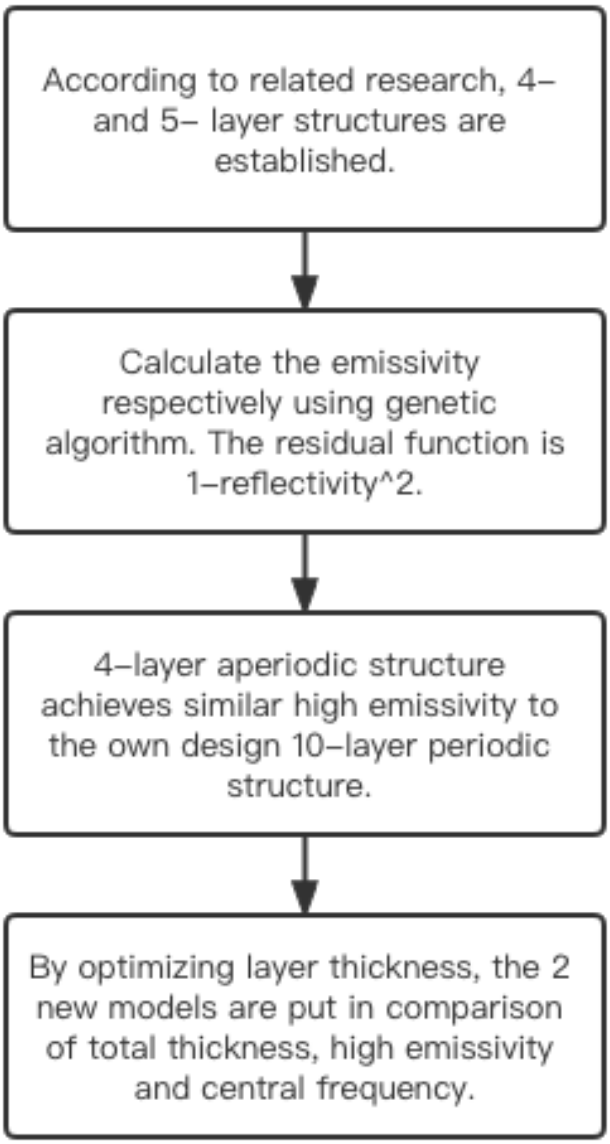

Figure 3.1: Flowchart of research process on emissivity of aperiodic multi-layer emitter.

The research methods involved in the simulation are transfer matrix and Genetic algorithm. The frequency range is set from 30 to 100 THz. The residual function is $1 - R^2$, where R is the reflectivity. Selection of refractive index of Si and SiO_2 will be discussed both from the related research and own optimized values. The target of this analysis is emissivity and reflectivity, not transmittance and spectral efficiency as in the following chapters.

3.2 Thermal emission of aperiodic structure

3.2.1 Structural characterisation

According to the illustration in former sub-chapter, periodically arrayed stack produces more useless peaks than aperiodic structure. The progress obtained in Chapter 2, on layer thickness optimisation, shows that the structures with layer thickness optimised by pattern search and genetic algorithm are more likely to be aperiodic, as shown in Table 3.2, and their optical performance is proved to be better than that of the original periodic model.

Table 3.2: layer thickness optimisation for 10-layer photonic crystal structures.

	L	H	L	H	L	H	L	H	L	H
Original/nm	82.276	30.174	82.276	30.174	82.276	30.174	82.276	30.174	82.276	30.174
PS/nm	73	2.8	8.3	30	77.5	27.5	75.8	27.7	81.4	0.4
GA/nm	72.283	2.8288	8.3107	26.968	77.4558	27.5338	75.7936	27.7224	81.4449	0.3772

Based on these simulation results, the assumption that better emissivity may be achieved by non-periodic structure is presented and remains to be proved by calculations and simulations. If the number of layers is reduced to eliminate the effects of adjacent peaks on emission spectrum, the maximum value of main peak will decrease with this modification[103, 104]. In the research cited previously, the stack consists of 7 layers, with SiO_2 and Silicon alternately arranged. The corresponding comparison structure is 17-layer periodic stack. Since the number of layers in the previous work is 10, the aperiodic objective will be selected as approximately 4 or 5. Specific number of layers will be tested to determine how many layers with aperiodic arrangement can achieve the same narrow band high-Q as the original periodic structure does.

3.2.2 Computational study

From Figure 3.2 (a) and (b), both periodic and non-periodic arrangements show narrowband high emissivity at the same frequency, 32.2 THz. Besides, the 10-layer alternating structure has some more adjacent peaks reaching their maximum emissivity at 37.15, 40.68 and 43.22 THz, respectively. For aperiodic 4-layer stack, the curve shows only the main emission peak within the range of 30 to 100 THz. However, the curve grows on the high-frequency side, which means the adjacent peak of aperiodic structure is located at the frequency larger than 100 THz.

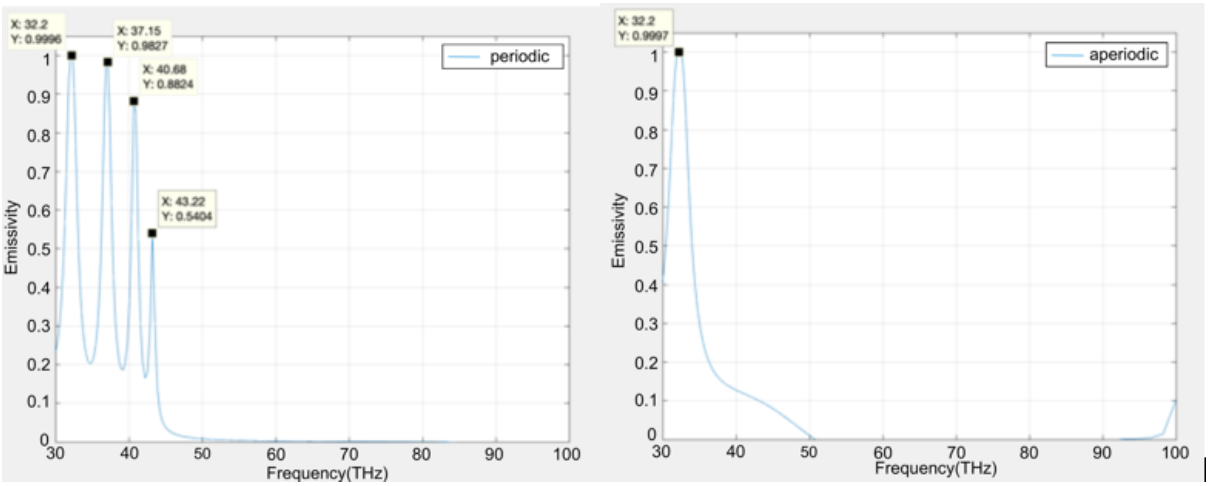

Figure 3.2: Emissivity versus frequency of (a) 10-layer periodic structure and (b) 4-layer non-periodic structure.

It is worth noting that in the optimisation, only the thicknesses of each layer are independent variables and the other parameters remain unchanged. The target is to obtain a non-periodic structure with the same or even higher emissivity around the same central frequency, or achieve same high emission peak with smaller total thickness. In accordance with Table 3.3, the same high-Q emissivity is more likely to be obtained. Without the interference of spurious adjacent peaks, the emission spectrum can be easier to use.

Table 3.3: Comparison between periodic and aperiodic stacks.

No.layers	$t_{total}(\mu m)$	f_{center}	$\|\varepsilon\|$	$Adj.^a f_{center}$	$Adj.^a \|\varepsilon\|$
10(periodic)	5.6225	32.2	0.9996	37.15	0.9827
4(aperiodic)	2.144	32.2	0.9997	100	-

By comparing the two models, the aperiodic stack achieves the same high emissivity with smaller number of layers, and the total thickness is only $214.3987nm$, much smaller than $562.25nm$ of periodic arrangement. For the 10-layer periodic structure, the adjacent peaks shift toward the main emission peak. The Q-factor and emissivity have an extremely small reduction, compared to the non-periodic stack (only 0.01%). In addition, the new structure eliminates spurious emission peaks beside the main peak.

3.3 Optimization of periodic and non-periodic structure

3.3.1 Periodic structural optimisation

Discussion in Chapter 3.2 is based on the assumption that a 10-layer structure has the same thickness of high and low refractive index layers. The previous discussion has already given the optimized results using Genetic Algorithm of each layer thickness, as Table 3.4 shows.

Table 3.4: Thickness optimization of GA and the original.

	L	H	L	H	L	H	L	H	L	H
Original/nm	82.276	30.174	82.276	30.174	82.276	30.174	82.276	30.174	82.276	30.174
GA/nm	72.283	2.8288	8.3107	26.968	77.4558	27.5338	75.7936	27.7224	81.4449	0.3772

The optimised film widths are more likely to approach aperiodic design. The total thickness is 400.7182 nm. As discussed previously, typically, the target function can be simply regarded as the fitness function if the difference of each evaluation is not too large. A fitness function can still be established to enhance the selection function among the population. Thus, fitness function in algorithm can be expressed as:

$$F = \frac{1}{n}\sum_{i=1}^{n}(E(f_i) - R(f_i))^2 \tag{3.1}$$

where f_{min} and f_{max} is 30 and 100 THz respectively and $R(fi)$ is reflectivity for the chosen frequency. This function can be obtained by Kirchhoff's law of thermal radiation and Transfer matrix method[105, 106]. The number of frequency points n is 501. $E(fi)$ is the target function and has the characteristics as below:

$$E(f_i) = \begin{cases} 1, & f = f_c \\ 0, & f \neq f_c \end{cases} \tag{3.2}$$

Here, f_c is the specific central frequency. The calculated result will become better if smaller F is obtained. The optimized variable is the thickness of each alternating dielectric layer t. Figure 3.3 shows the emissivity of the periodic structure with and without optimisation.

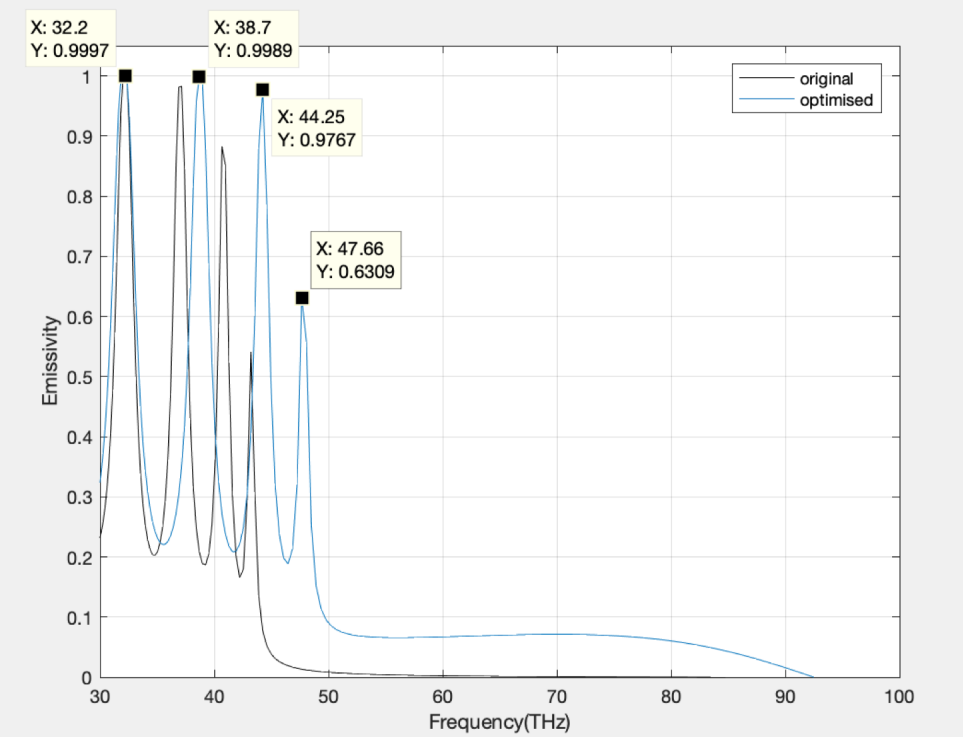

Figure 3.3: Emissivity versus frequency of (a) periodic stack and (b) optimised structure.

Comparing the curves and data given in Figure 3.3, the main peak stays at the centre frequency of 32.2 THz, and the narrowband width does not change much either. The adjacent peaks have all increased their maximum value and moved in the high frequency direction. Since the layer thicknesses are modified, the outcome shows that the second peak has raised its maximum value from 0.9927 to 0.9989. The distance between main and most adjacent peaks decreases from 60.61 to 46.15 nm. This makes the spurious adjacent peaks somehow more useful if the emissivity beyond main peak can be of interest.

3.3.2 Non-periodic structural optimisation

To optimise the Silicon and SiO_2 layers of non-periodic stack, the number of variables should be modified to 2 in GA and the other settings can follow its default operation. The optimized variable are the thickness of each dielectric layer t and number of layers N. The research target of this step is to narrow the main peak to meet the emission performance of previous periodic model. From Figure 3.4, it is obvious that the main peak has narrower width after optimisation. The total thickness has reduced from 3.4437 to 2.144 μm. The maximum values show small difference, between 0.9997 and 0.9996, the original best value. The optimized curve shows no rising trend in the specific range, which means its adjacent peak has moved to short wavelength

direction.

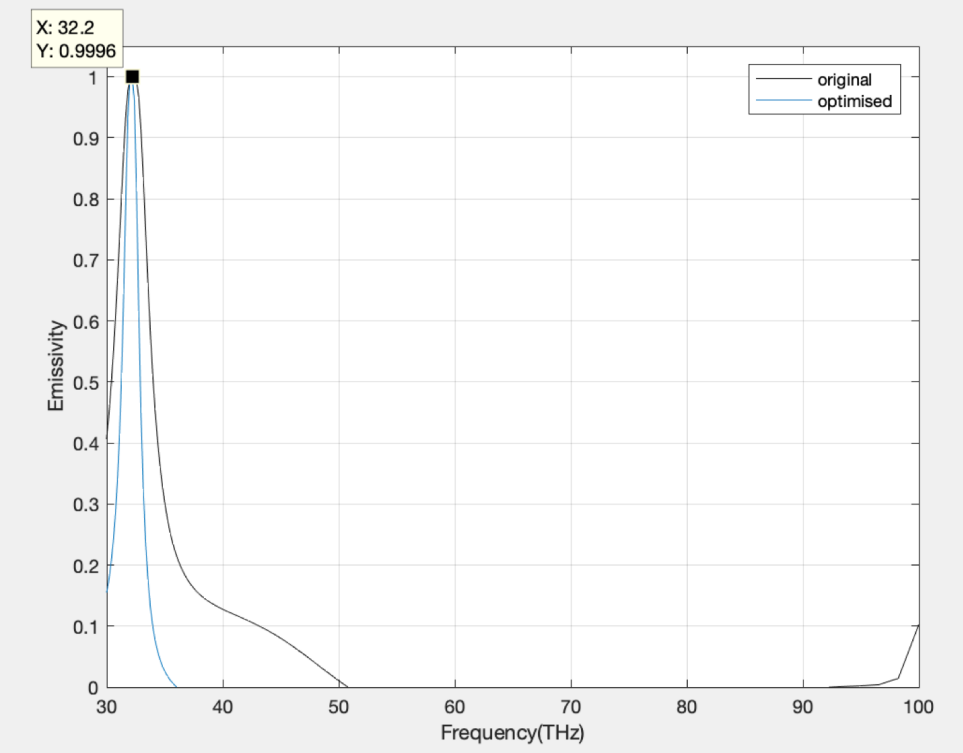

Figure 3.4: Emissivity versus frequency of (a) aperiodic stack and (b) optimised structure.

The characteristics of optimised emission spectrum shows a cut-off at around 0.83 μm, with the peak obtained between 0.83 and 1.01 μm and almost no emission beyond 0.83 μm. For the original 4-layer structure, the main emission peak occurs at approximately 0.59 μm and reaches a maximum at 0.93 μm.

3.3.3 Comparative studies of the structure characteristics

Finally, the comparison between optimised structures with periodic and non-periodic arrangement is shown in Figure 3.5. The peak values of emissivity are actually the same for both structures. Non-periodic structure has smaller width of the main peak and periodic structure has an adjacent peak which is very close to the maximum emissivity. From the data in Table 3.5, the total width of thin films of periodic and non-periodic structures are 4.0072 and 2.144 μm respectively.

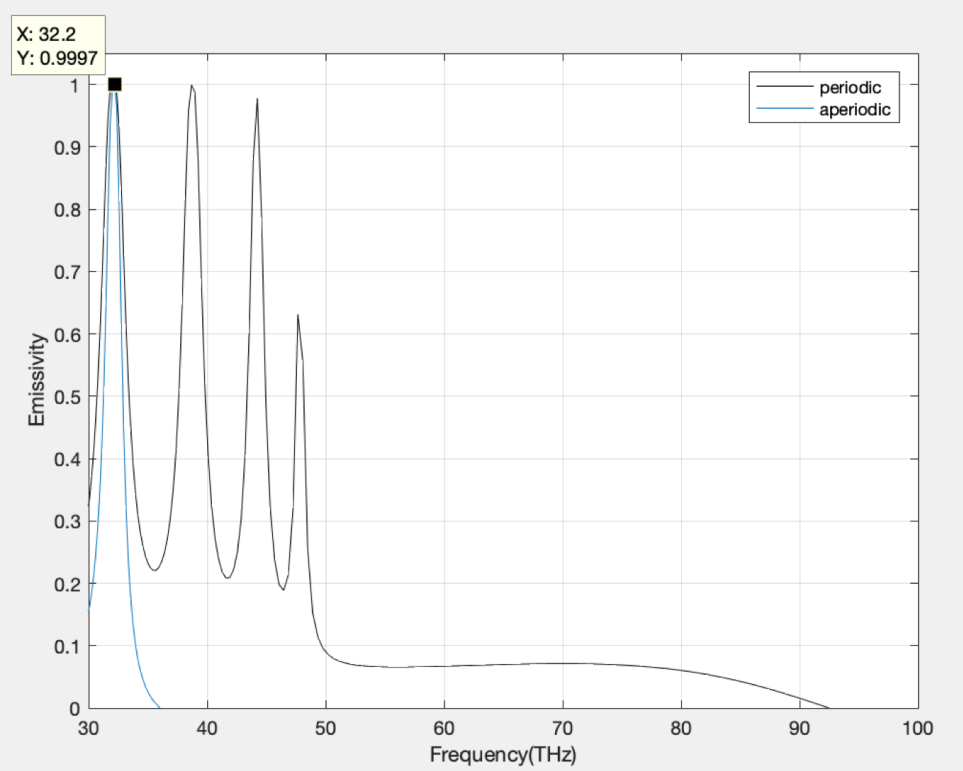

Figure 3.5: Emissivity versus frequency of optimised aperiodic and periodic structures.

The absorption of thermal emission energy by both crystal structures is mainly concentrated around 0.83-1.01 μm. Both structures are well suited for use with GaSb cells, since the emission energies of photons are in the band of less than 1.8 μm.

Table 3.5: Comparison between periodic and aperiodic stacks before and after optimisation.

No.layers	$t_{total}(\mu m)$	$f_{center}(THz)$	$\|\varepsilon\|$
10(periodic)	5.6225	32.2	0.9996
10(Optimised)	4.0072	32.2	0.9997
4(periodic)	3.4437	32.2	0.9997
4(Optimised)	2.144	32.2	0.9997

Table 3.5 shows the different structures of 10-layer original stack, and 10-layer films with optimised thicknesses. For non-periodic designs, there will also be original and GA optimised structures. If these two optimised models are fabricated, aperiodic stack has the advantages of smaller width and high emission performance. Based on our previous work, when the research target is the spectral efficiency, Genetic algorithm also shows the trend of changing from periodic to aperiodic structure of multilayer TPV system, which means non-periodic may have promising superiority both in emission and spectral performance.

3.4 Conclusion and further expectations

This chapter focused on improving the emission characteristics of alternately arrayed photonic crystals. Learning from the related research, aperiodic structure is introduced in this chapter. Compared to traditional photonic crystals, it uses smaller number of layers and obtains the same or even higher emissivity at specific frequency. The new structure shows better optical performance and is worth discussing its advantages and features in thermal emission field. The standard of determining an optimum is to enlarge the generation size. The result remains unchanged is the best value if such optimizations have been made.

Based on the previous optimized results, the two models of original stack of 10-layer PhC and thickness adjusted by GA are brought to comparison, as well as the structures of non-periodic with and without optimisation. Since the layer number is not too large, the transfer matrix can be easily modified for each layer. Two variables are the targets to be optimised. The optimization outcome both reduces the total thickness of the whole stack and maintains their high emissivity features. Regulated non-periodic thin films show even narrower band width of the main peak. For the modification of periodic structure, thickness optimised model increases the maximum value of the second peak closer to the best value on main peak, which may be considered useful if stronger emission is required for application in a specific frequency range.

Chapter 4

1-D multilayered filters

This chapter focuses on one-dimensional photonic crystals for applications in optical filters. The effect of structure on spectral efficiency is compared by simulations of self-designed models with related studies. Complex refractive index and interfacial roughness are employed separately to research the optical performance of multilayered system. In addition, the optimal spectral efficiency under the influence of rough interface is derived using a Genetic algorithm taking transmittance and spectral efficiency as optimisation objectives respectively.

4.1 Overview

This chapter presents the simulation results and data comparisons on both photonic crystal characteristics and its influence on TPV cell performance. Although the simulation of multilayer filters is not new, the simulation will still contain this part to show the specific designed model of this project. The transmittance and reflectance of the model will be in the first part of the results and then used in the calculations of average value of energy transfer from the hot body to the TPV cell. So it is important to give the structure properties initially. Spectral efficiency is a significant indicator to measure the conversion performance of TPV systems [26, 107]. The role of optical filter applied in the project is to increase the transmittance so that more energy can be transmitted to the cell [108]. In this chapter, the simulation would be focused on the layer numbers and different thickness of each layer. The goal of the attempts is to increase the transmission peaks of the spectrum with other main parameters constant (e.g. the refractive index of two materials). By comparing different structures of photonic crystals,

the best performance would be selected to calculate the spectral efficiency for its application in the TPV system. Besides, this part is not only used to compare the optical performance of different model properties in this project, but also to put in the comparison with related research to show the unique characteristics of the designed structure here.

In the second-half, we account for the effect of interface roughness, which is known to affect the spectral properties of thin films [36]. The reason why the specific design is selected to be 10-layer multistacks is briefly explained, with further research on how the layer number affect the optical performance with interface roughness considered. Its influence on the spectral efficiency of TPV systems, in particular those using multi-layer filters based on Si/SiO2 and SiO2/TiO2 are analyzed. Transmittance and spectral efficiency are set to be the optimisation target separately using the evolution algorithm.

4.2 Effect of complex refractive index on optical efficiency of thermophotovoltaics with multi-layer filters

4.2.1 Complex RI in two-layer filter

The model considered in this report has two materials. So, the multi-layer model would be firstly introduced. In this case, the period number is 1 and the transmittance won't change much because of the restricted filtering effects. It is important to point out that the complex refractive index is input so the absorption would be a bit different from the traditional cases. The simulation results are shown in Figure 4.1.

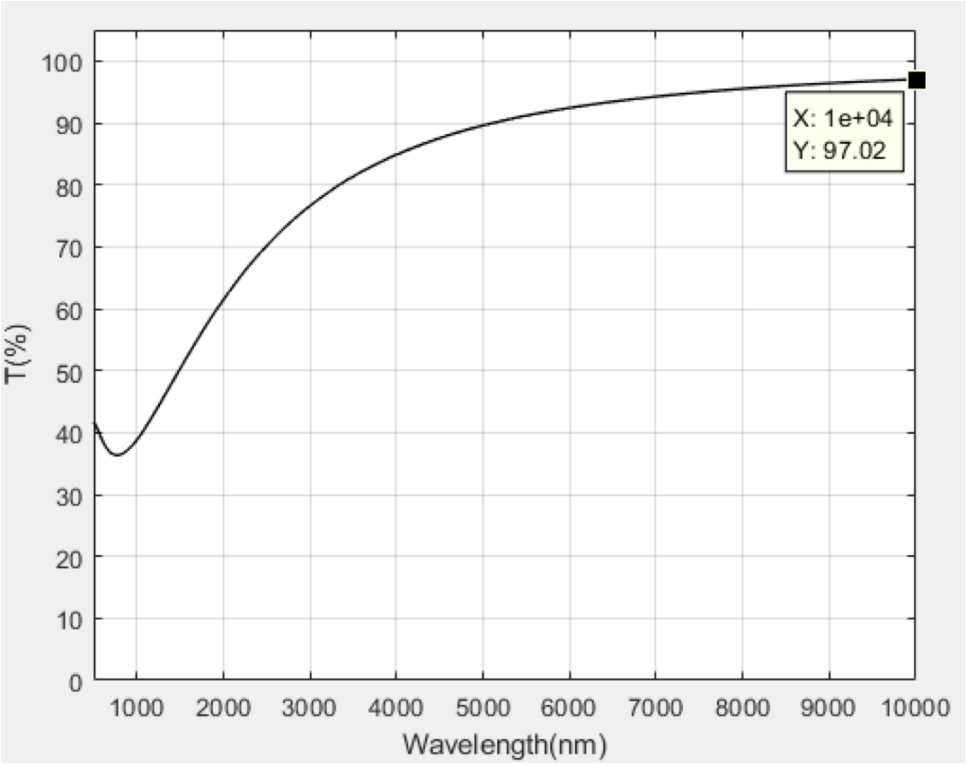

Figure 4.1: Transmittance on two-layer filter system. n(Si)=3.9766, n(SiO_2) = 1.4585.

From Fig. 4.1, the highest value of transmittance in the specific wavelength range can reached 0.9702. A small absorption exists due to the imaginary part of refractive index. This can be explained by the calculation process of transmittance[109]. The expression for the amplitude transmittance coefficient τ is

$$\tau = \frac{2\mu_0}{\eta_0 + Y} \tag{4.1}$$

η_0 is the surface admittance of incidence medium and Y is the admittance of medium 1 and 2. In this case, the value of τ equals to 0.3656-0.6629i and then changes to -0.1240 - $0.5731i$ for the other layer. The absolute value of τ decreased so that the transmittance is reduced as a result. The spectral efficiency in this case, as Figure 4.2 shows, is 0.1316 for the black body temperature 1000 K and 0.3800 for 1800 K, respectively.

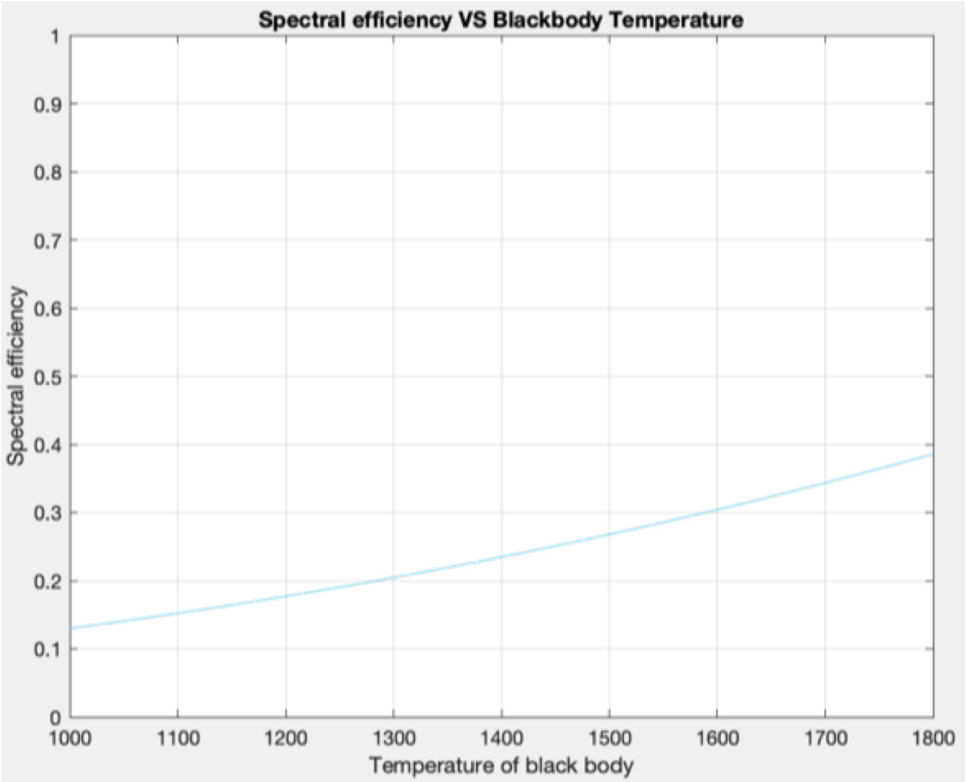

Figure 4.2: Spectral efficiency of two-layer filter system. n(Si)=3.9766, n(SiO_2) = 1.4585.

4.2.2 Complex RI in multi-layer filter

For multilayer structure, the number of periods should be taken into consideration. This subchapter discusses different structures, described in related literature. Simulated results will be combined together to see the difference of structure properties. Last but not the least, all the simulations will be based on the fact that one medium has complex refractive index.

Figure 4.3 shows the transmission spectrum of $L/2H(LH)^4$ structure (a 10-layer periodic structure with first layer half-sized) [26]. The bandgap is between 1800 to 3800 nm and the minimum value of transmittance is 4.362×10^{-4}. The largest peak reaches 80.51% at 7777 nm. From 2 to 3.5 , the transmittance remains at 0 which means the light could be 100% refelcted back in this range. The transmission spectrum in the specific range of wavelength shows its good compatibility with GaSb cell(1.78). Figure 4.4 shows the curves plotted for different wavelengths and black body temperatures.

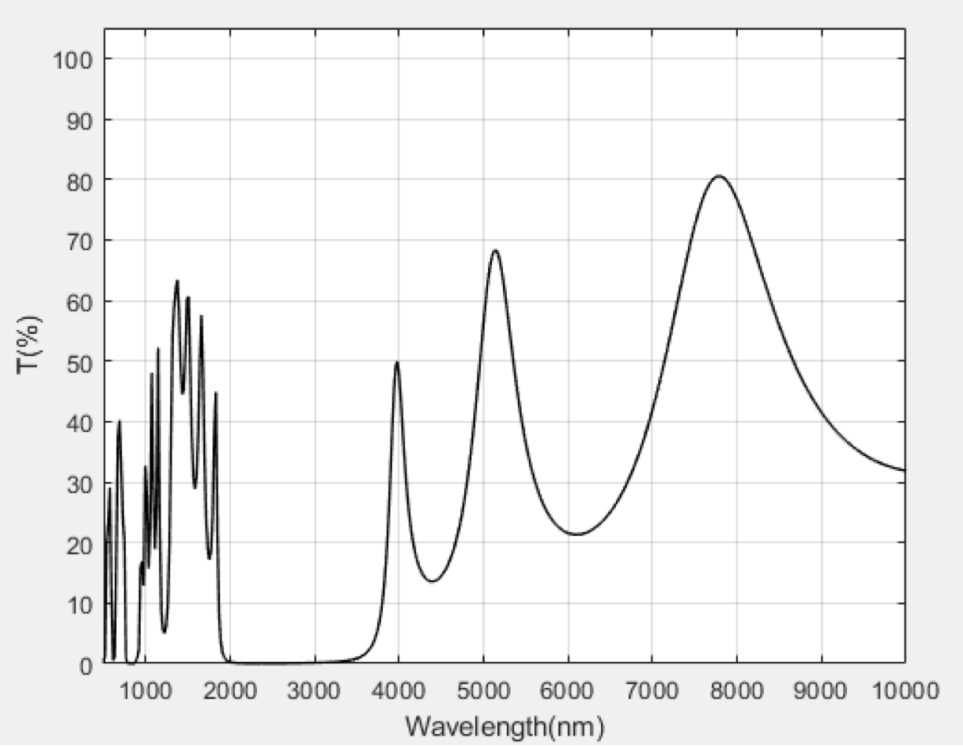

Figure 4.3: Transmittance of L/2H(LH)4 structure. n(Si)=3.9766, n(SiO_2) = $1.4585 + 0.30209i$.

As demonstrated above, the complex index has affected every loop and changed the size of every loop iteration. This may results in the large quantity of calculations. However, these curves can be filtered by the expressions in Chapter 2. For example, some of the data are negative and some of the data exceeded 1. These can be obvious faults and should be avoided. The range of spectral efficiency in this case is 0.1908-0.58. This range is a bit smaller than for the two-layer structure in the former sub-chapter, because of more layers with complex index involved.

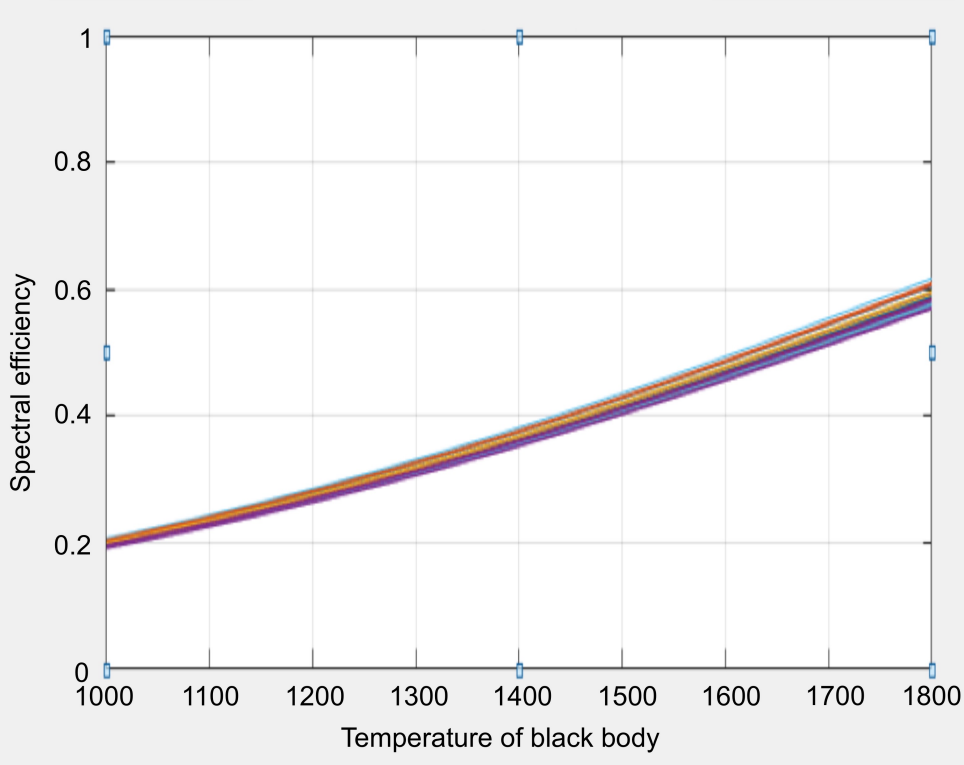

Figure 4.4: Spectral efficiency of L/2H(LH)4 structure.n(Si)=3.9766, n(SiO_2) = 1.4585 + 0.30209i.

There are three types of optical filters with the same stack structure but different layer thicknesses according to the research of optimized structure designs [89]. For periodic stack, the thicknesses of high and low index media are 495 and 160 nm, respectively. Modified structure will have its first and last layers reduced in thickness, and the optimized structure has different thickness of each layer.

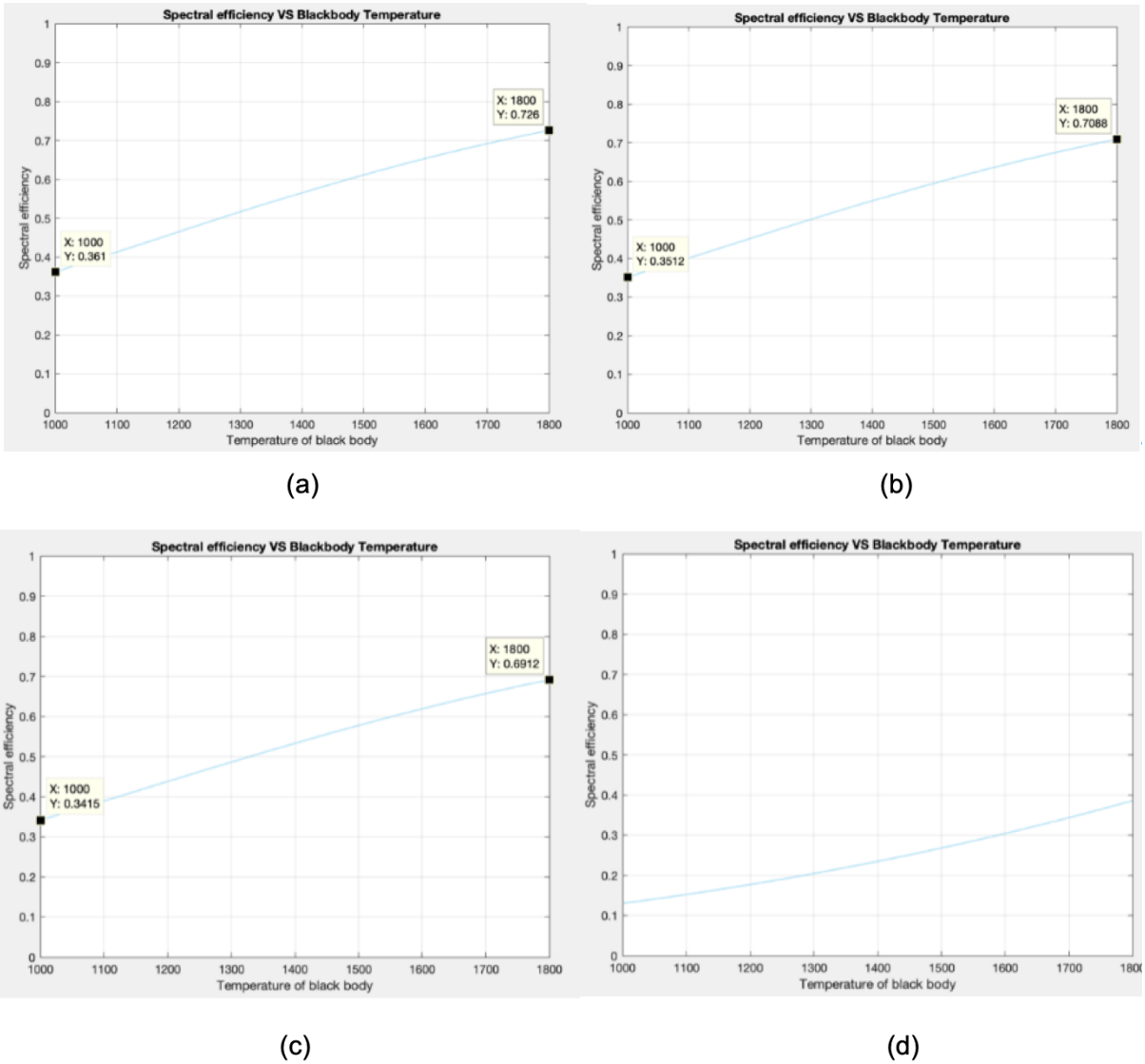

Figure 4.5: Spectral efficiency of (LH)5 structure. (a) Periodic structure (b) Modified structurefirst and last layer half-sized (c) Optimized structure (optimized based on (b))(d) Stacks with no filter applied.

It is obvious to point out that the spectral efficiency of the three models has slightly increased due to the modification of structure. The spectral efficiency for original 10-layer structure is 34.15%-69.12%. Modified structure possesses 35.12%-70.88% and the range for the optimized stack is from 36.1% to 72.6%. With the filters applied, the efficiency of the TPV system is improved.

4.2.3 Complex RI in designed 1D PhC filter TPV system

In this section, the designed structure of optical filter is built with 10 layers. Each layer has its thickness. Since the absorption is included, the thickness will be slightly changed compared to

the reference optical thickness. Since the complex refractive index has influence on the optical performance of the filter structure, the factors illustrated before, i.e. complex refractive index, should be taken into consideration for better performance. To achieve higher transmittance, the number of periods should not be too large. From various related research reports, the limitation for the number of layers in typical models is 10 [26, 89, 110–112]. The reason why 10-layer structure is preferable will be included in Chapter 4.3, with figures and explanations. Based on our previous calculations, the layer thickness should not be too large either, to obtain higher transmission peak values. The main transmission peaks increase when the imaginary part is increasing. At this moment, the side peaks decrease. So, it is important to check the transmission peaks distribution in the specific angular frequency range of the unique structure.

Typically, the layer thickness equals a quarter of free space wavelength divided by the refractive index [113]. In this case, the reference free space wavelength is 480 nm. The absolute reference layer thickness (since the refractive index of one medium contains complex number) of two media should be 30.174 and 82.276 nm respectively. The thickness of each layer is shown in Table 4.1.

Table 4.1: Thickness of $(LH)_5 structure$.

	L	H	L	H	L	H	L	H	L	H
Thickness/nm	73	2.8	8.3	30	77.5	27.5	75.8	27.7	81.4	0.4

Transmittance curve of this structure is shown in Fig. 4.6. The maximum value at the peak is 90.29% and the average transmittance is 70.16%. Compared to the structure with thickness not modified, the peak value is reduced. However, the average value has increased from 58.77% to 70.16%. As mentioned in the former chapters, the average transmittance is an important factor in the calculation of spectral efficiency. So, the modified model does have better optical performance than the original structure.

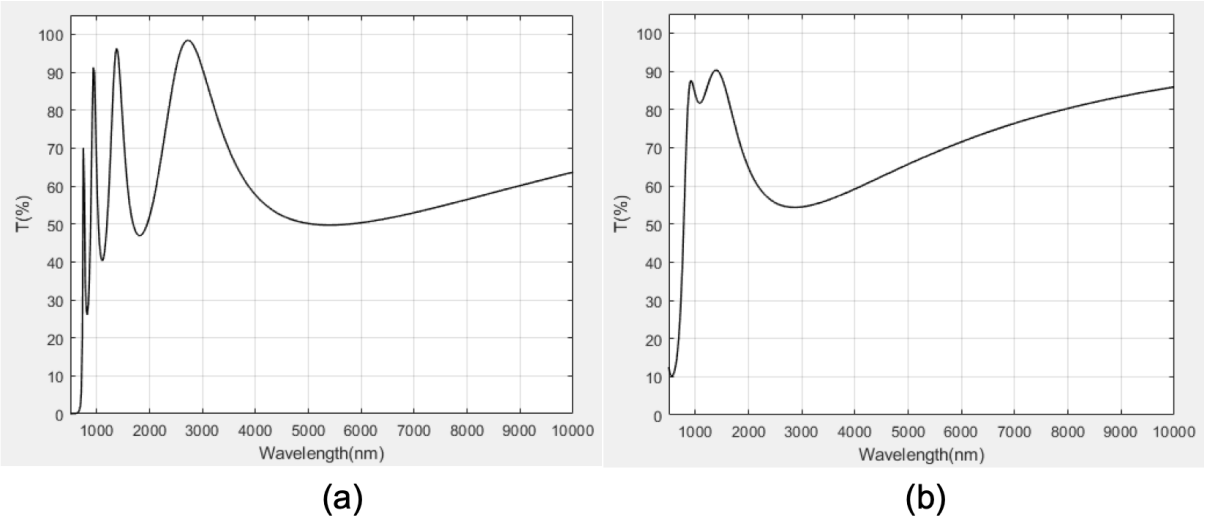

Figure 4.6: Transmission spectrum of designed structure with (a) Reference layer thickness (b) Modified layer thickness.

Comparing the structures in Figure 4.6 (a) and (b), their spectral efficiency has different trend, as given in Figure 4.7. By modifying the layer thickness, the spectral efficiency range rises from 18.75-54.62% to 19.85-59.16%. Compared to the two-layer filter model, the efficiency has increased approximately by 13.9% on the average.

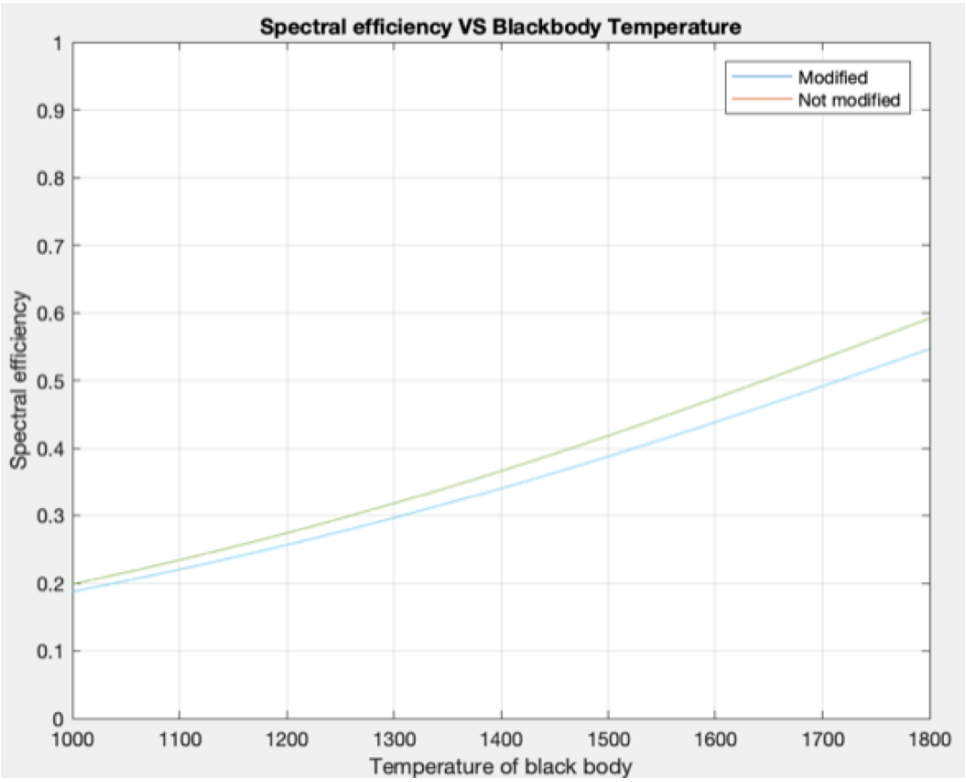

Figure 4.7: Spectral efficiency of designed structure with and without modifications.

The simulation results are all based on the fact that one medium has complex refractive index. The imaginary part influences the amplitude transmittance and reflectance coefficient and finally influence the spectral efficiency. In the process of photonic crystal fabrication, deviation cannot be completely avoided. The complex refractive index has provided practical meaning for discussing the transmission characteristics of photonic crystals.

4.3 Effect of interface roughness on spectral efficiency of thermophotovoltaics with multi-layer filters

4.3.1 Simulation of different models in the literature

Since the spectral efficiency is one of the most important parameters to define the optical performance of TPV system, we consider the effect of interface roughness on spectral efficiency. The 10-layer filter structure designed in [89] is based on MgF_2 and Ge layers, with the refractive indices 1.36 and 4.2, respectively. In the initial periodic structure, with no layer thickness optimization, the widths of low and high index layers are 0.495 and $0.16\mu m$. In this case, MgF_2 and Ge array is $(LH)^5$. Although the blackbody temperature range in [89] was from 1200 to 1800 K, it is here expanded to 1000-1800 K for comparison with other structures. Fig. 4.8 shows the spectral efficiency variation when changing the rms height Z.

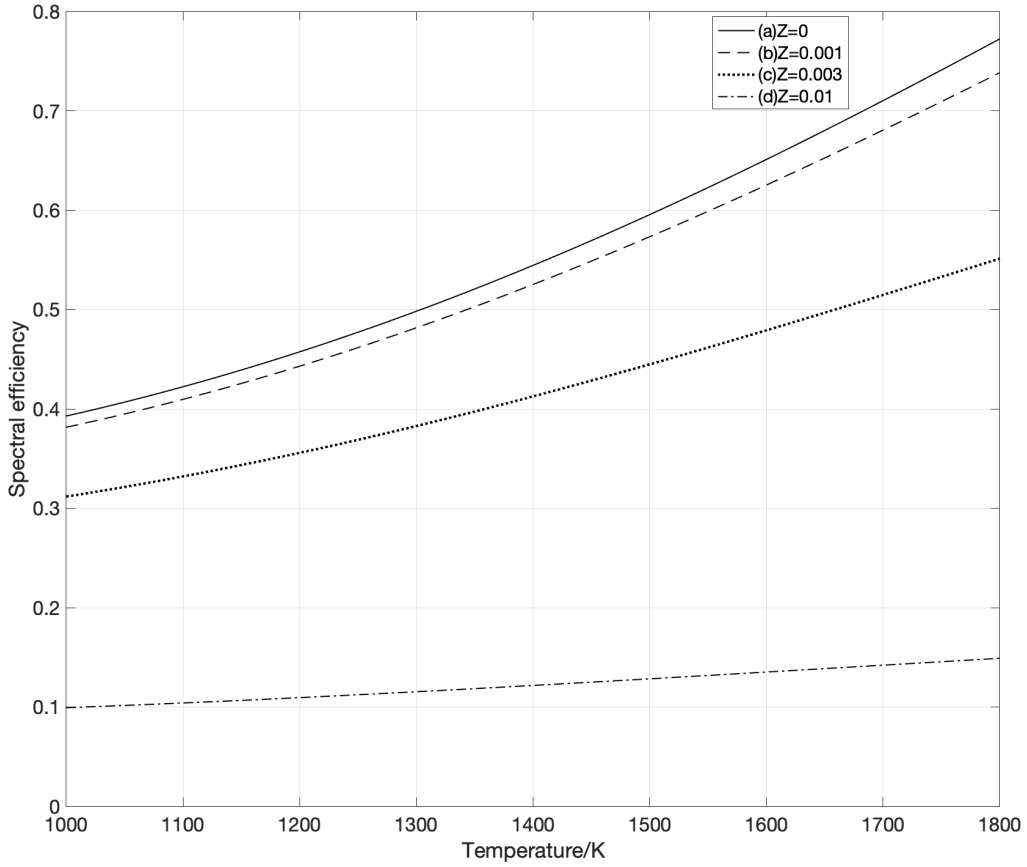

Figure 4.8: $(LH)_5$ structure of MgF_2/Ge with (a) perfectly flat interfaces, Z=0[89] (b) Z=0.001μm (c) Z=0.003μm (d) Z=0.01μm.

Introducing finite Z clearly has a strong influence on the spectral efficiency of this structure. When Z is 0.001, the efficiency decreases only mildly, from 39.28-77.24% to 38.15- 73.83% in the temperature range 1000-1800K; however, for Z increasing to 0.01, the efficiency decreases very much, to just 9.93- 10.49%. Another example is from [26], with $L/2H(LH)^4$ structure. For this, 10-layer structure, Si and SiO_2 are periodically arrayed and the difference from the previous example is aperiodicity in the initial layers. The effects of roughness are shown in Fig. 4.9.

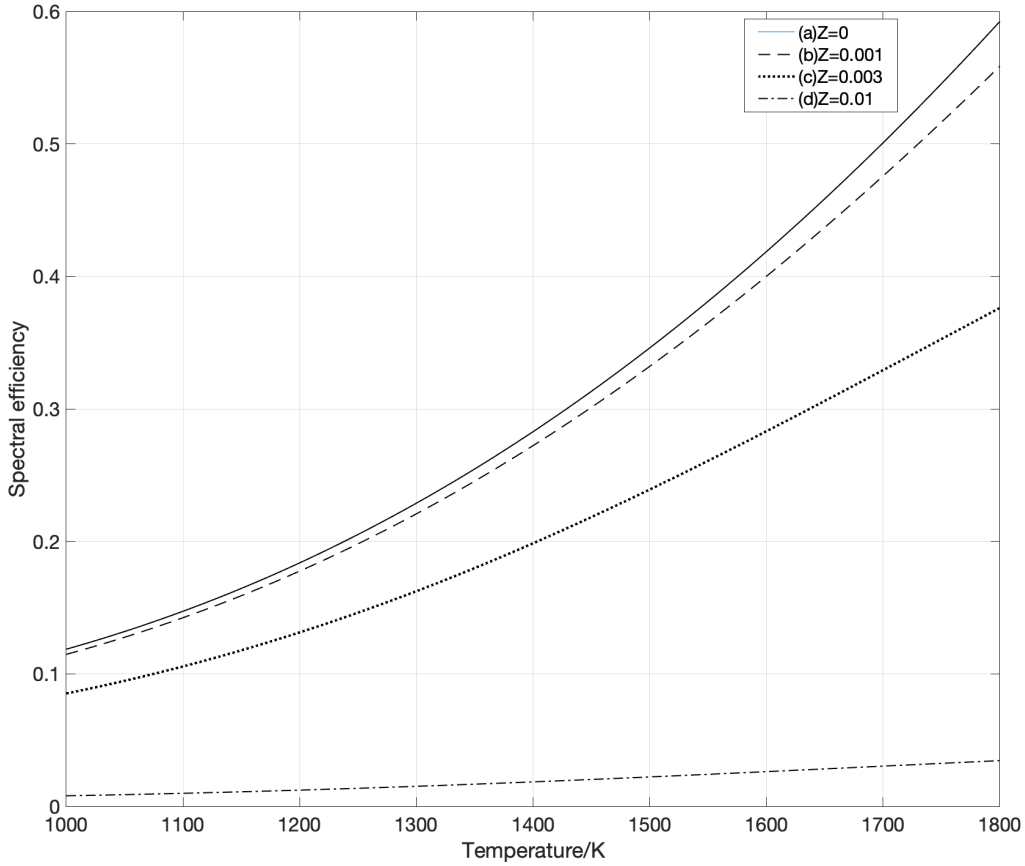

Figure 4.9: Spectral efficiency of an $L/2H(LH)_4$ structure of Si/SiO_2 with (a) perfectly flat interfaces, Z=0 [26], (b) Z=0.001μm (c) Z=0.003μm (d) Z=0.01μm. n(Si) and n(SiO_2) are 3.4 and 1.5, and d(Si)=0.17μm, d(SiO_2)=0.39μm.

The interface roughness also seriously degrades the spectral efficiency. The spectral density show a moderate decrease from 11.86- 59.24% to 11.47- 55.86% in the temperature range 1000-1800K when rms height is 0.001μm, and a very significant reduction, to 0.80 – 3.35% if Z is 0.01μm.

4.3.2 Different materials for 10-layer structure

In this example the stack also has 10 layers, and the structure is $(LH)_5$. $SiO_2 is the material for low refractive ind$ will be high index layers, and the two choices will be compared. Fig. 4.11 gives the performance of Si/SiO_2 with different interface roughnesses.

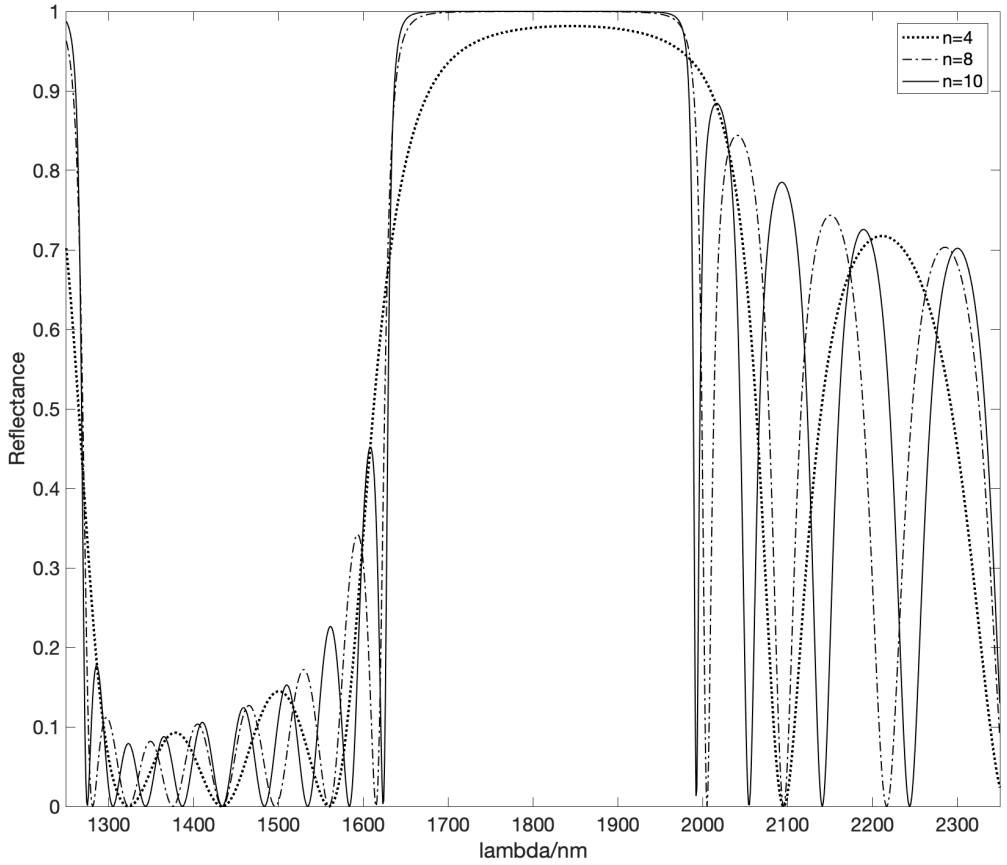

Figure 4.10: Reflectance of Si/SiO_2 $(LH)_n$ structures with (a) n=4 (b) n=8 (c) n=10. The refractive indices n(Si) and n(SiO_2) are 3.97 and 1.45, and widths d(Si)=30.18nm, d(SiO_2)=82.76nm.

Fig. 4.11 shows the spectral efficiency for a 10 layer, SiO_2/Si periodic $(LH)_5$ filter structure. This choice is based on comparison of results shown in Fig. 4.10. The reflectance in the bandgap region steeply increases to 99% when the number of periods increased from 4 to 8. The reflectance reaches 100% for 10-layer structure. Therefore, the 10-layer periodic array of Silicon and SiO_2 is chosen as the initial model, in which the roughness is introduced. From Fig. 4.11, for Z=0.001μm the spectral efficiency only slightly decreases relative to the case of perfectly flat layers, from 19- 61% to 18- 55%, but for Z=0.01μm the spectral efficiency dramatically decreases to 1- 4%.

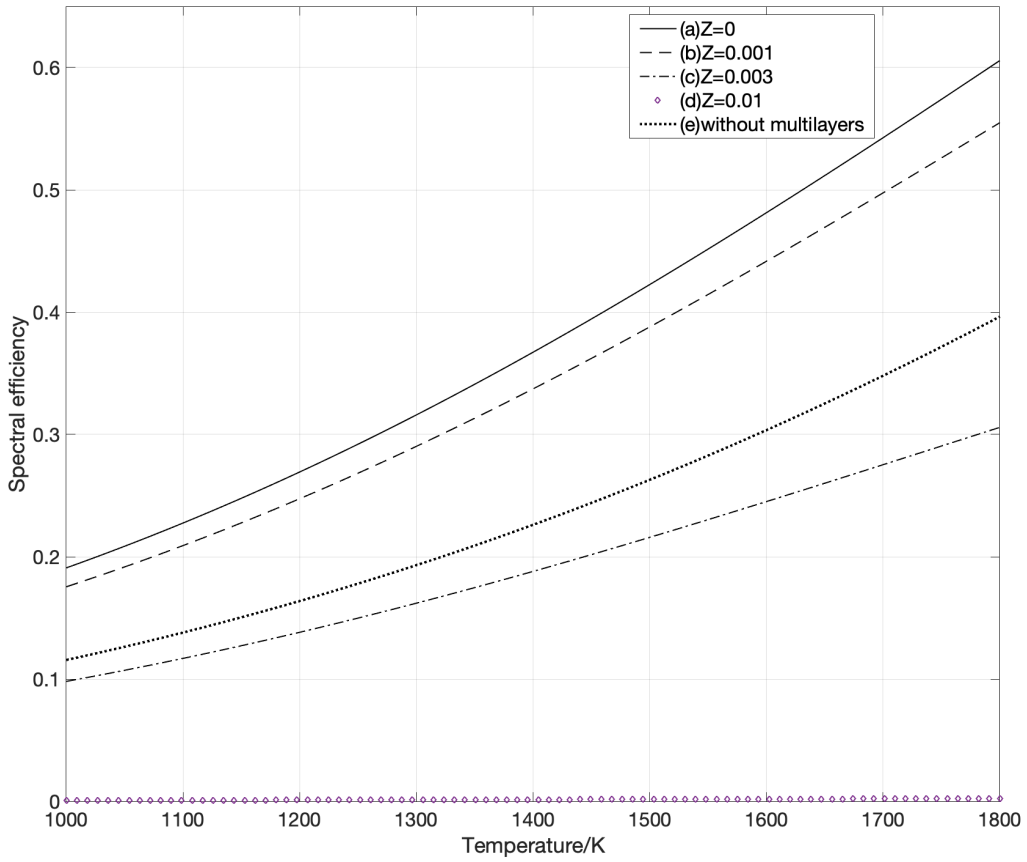

Figure 4.11: $(LH)_5$ structure of Si/SiO_2 with (a) Z=0 (b) Z=0.001μm (c) Z=0.003μm (d) Z=0.01μm (e) without multilayer filter. n(Si) and n(SiO_2) are 3.97 and 1.45, and d(Si)=30.18nm, d(SiO_2)=82.76nm.

When the high index material is changed from Si to TiO_2, the spectral efficiency changes from 19- 56% for flat interfaces to 18- 53% for Z =0.001μm, and 1 – 3% for Z = 0.01μm (Fig. 6). If no spectral filter is used, the efficiency is only 12-40%, as given by line (e) in Fig. 4.12.

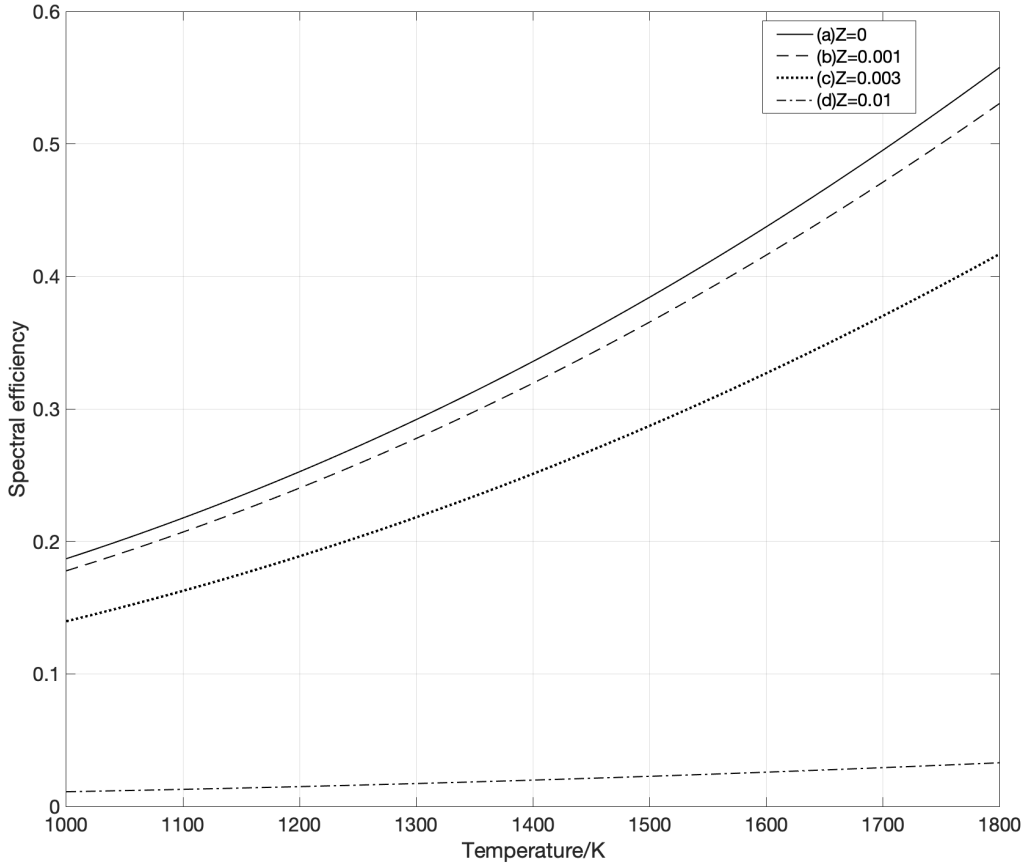

Figure 4.12: $(LH)_5$ structure of SiO_2/TiO_2 with (a) Z=0 (b) Z=0.001μm (c) Z=0.003μm (d) Z=0.01μm. n(TiO_2) is 2.1 and d(TiO_2)=57.14nm.

4.3.3 Optimisation of number of layers and thickness

In the above discussion, different materials and structures of 10-layer stacks were considered. To obtain a better spectral efficiency, the number of layers and their thicknesses can be optimized as well. For multilayer structures composed of SiO_2 and TiO_2, 10-layers, 8-layers and 6-layers cases are compared in Fig. 4.13.

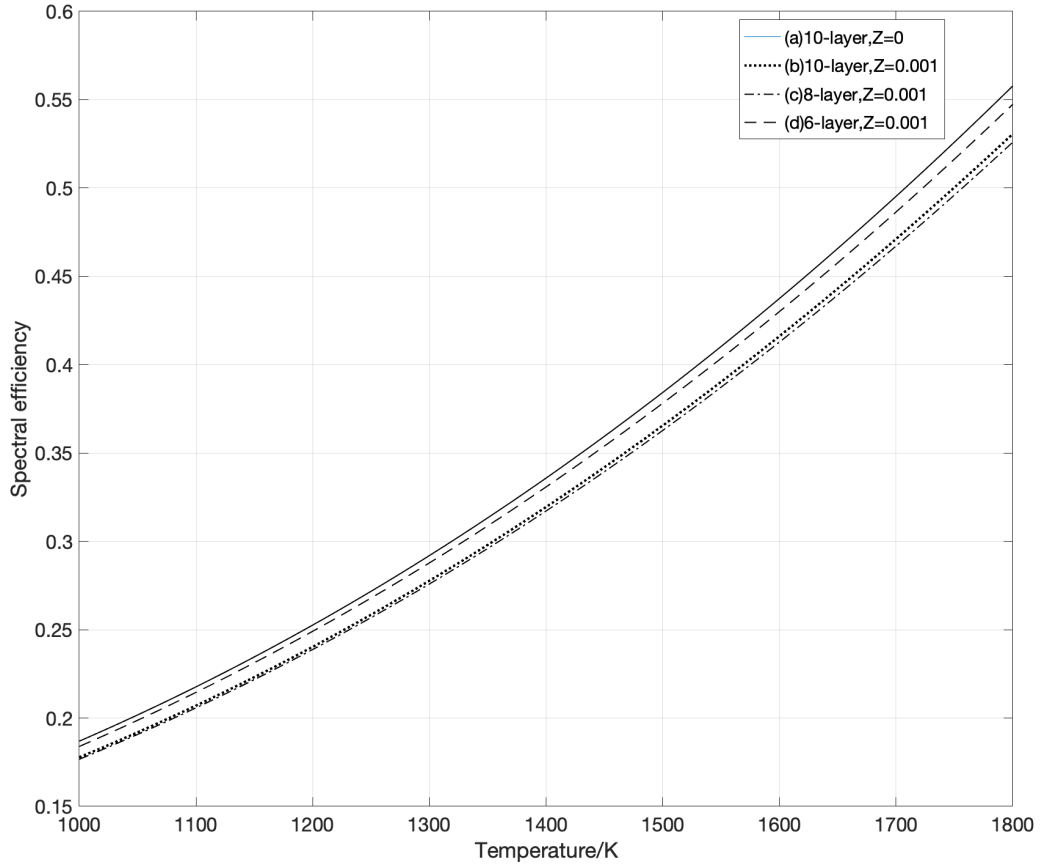

Figure 4.13: $(LH)_5$ structure of SiO_2/TiO_2 with (a) perfectly flat 10-layers (b) 10-layers, Z=0.001μm (c) 8-layers, Z=0.001μm. (d) 6-layers, Z=0.001μm.

By comparing the data for spectral efficiency of the three structures, it is interesting to point out that, in the presence of interface roughness, the 6-layers structure shows higher efficiency than 10-layer and 8-layer ones, which means that, if roughness cannot be avoided, 6-layers would be the best choice to obtain better performance. Another example includes the optimization of layer thicknesses of Si/SiO_2 structure. Genetic algorithm is applied to calculate the best value of each layer thickness, where the goal function is the transmittance of the same type as in one-dimensional photonic crystals. A fitness function is set to determine if each chromosome is better than its father generation [114, 115]. In this case the target function has optical constants and film thicknesses as independent variables. The target function for nth generation can be written as:

$$T' = \sqrt{\frac{1}{n}\sum_{i=1}^{n}(T_e(\lambda, d) - T(\lambda, d))^2} \tag{4.2}$$

where $T(\lambda_i, d)$ is the calculated transmittance and T_e can be taken as 1 for photon energies higher than the PV cell band gap, and 0 otherwise [87, 116]. This function is designed to find the difference between calculated and target values. The overall, global target is to minimize T'. A structure optimized in this way does not necessarily yield the global maximum, but it can be expected that it will identify a design which lies close to the top of the performance range. Alternatively, the spectral efficiency can be used as the optimization target function (and this then depends on the black body source temperature).

Table 4.2: Optimized $(LH)_5$ Si/SiO_2 structures layer thicknesses. n(high)=3.9766, n(low)=1.4585.

	L	H	L	H	L	H	L	H	L	H
Original/nm	82.276	30.174	82.276	30.174	82.276	30.174	82.276	30.174	82.276	30.174
GA_T/nm	72.283	2.8288	8.3107	26.968	77.4558	27.5338	75.7936	27.7224	81.4449	0.3772
GA_{SE}/nm	70.7242	2.9044	8.3189	26.577	73.8153	25.0146	73.3876	26.8928	72.6942	0.4046

Table 4.2 lists the optimum thicknesses of each layer obtained both by using transmittance T' as the target (GA_T entries) and by using spectral efficiency at T = 1500K as the target (GA_{SE} entries). Some of layer thicknesses have been modified significantly by the evolution algorithm. Fig. 4.14 compares the spectral efficiencies of structures optimized by both the above methods with the unoptimized structure, throughout the temperature range 1000-1800K. The optimized structures have higher spectral efficiencies than the original structure in most of the temperature range considered, both with and without interface roughness included. Use of the spectral efficiency target results in designs with better performance at low temperatures, but the transmittance target yields designs which perform better at the higher end of the temperature range.

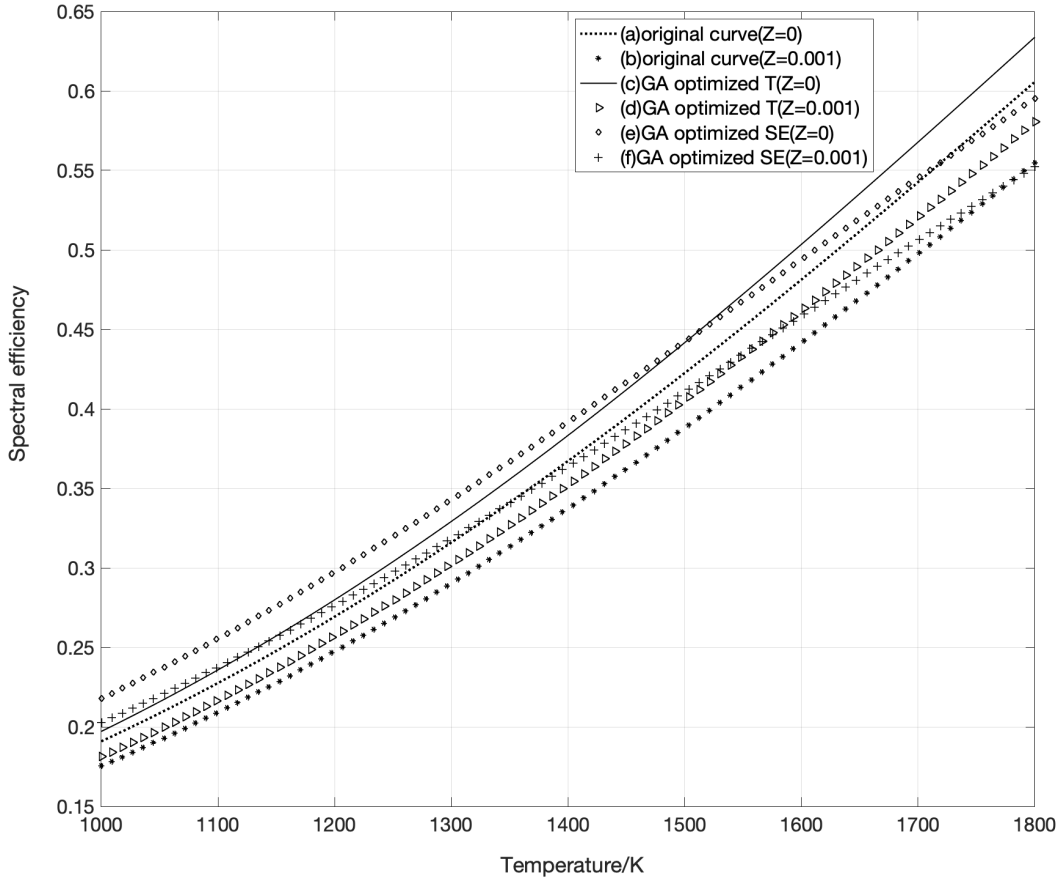

Figure 4.14: The spectral efficiency of $(LH)_5$ structure with Si/SiO_2 with (a) original 10-layer periodic structure with Z=0, (b) original 10-layer periodic structure with Z=0.001μm, (c) optimized for Transmittance, with Z=0, (d) optimized for Transmittance, with Z=0.001μm, (e) optimized for Spectral efficiency, with Z=0, (f) optimized for Spectral efficiency, with Z=0.001μm.

In Figure 4.14, curves (a) and (b) are for periodic structure with original layer thicknesses. The genetic algorithm is then applied to optimize layer widths, assuming Z=0. The calculated widths are used in the spectral efficiency calculations to obtain curves (c) and (d). To demonstrate the influence of roughness on the performance of multilayer filters, the evolution algorithm is then used to calculate layer thicknesses when the spectral efficiency is taken as the target, as shown in the third line in Table.2. Curves (e) and (f) are then obtained using these new optimization results, for Z=0 and Z=0.001 respectively.

Table 4.3: Spectral efficiency of original, transmittance-optimized and spectral efficiency optimized structures.

Average spectral efficiency	Z=0	Z=0.001
Original	37.80%	34.70%
GA_T	39.45%	36.21%
GA_{SE}	39.69%	36.87%

From Fig. 4.14, the difference among various cases is hard to observe. Table 4.3 gives the comparison. The optimized structures improved by 1.89% and 2.17% in cases of Z=0 and 0.001 , respectively, which points to the fact that layer thickness optimization delivers a higher spectral efficiency, especially when interfaces are not ideally smooth.

4.4 Conclusion and further expectations

Using the Transfer Matrix method, the effects of complex refractive index and interface roughness on the spectral efficiency of multi-layer structures used as filters in TPV systems are investigated. Different materials and structures are tested in this respect, both from other published research or our own designs, based on which the guidelines for tolerable interface roughness in these structures were given, in the range Z=0.001μm to Z=0.003μm. Also, if the roughness cannot be avoided, the structures with smaller number of layers are generally preferable. Besides, the genetic algorithm can be used to raise the average transmittance considering the refractive index with imaginary part by approximately 11%. Finally, the optimization of layer thicknesses with interface roughness accounted for can slightly improve the optical performance of a filter, but it is still below that with no roughness present.

Chapter 5

2-D W photonic crystals

The research in this chapter explores different materials and structures of two-dimensional photonic crystals to provide a theoretical basis for the application of radiators in thermophotovoltaic systems. Photonic band utilisation ratio is proposed as a criterion for evaluting the optical performance. Optimal structures are derived based on comparison and their fill rates are optimised using genetic algorithms.

5.1 Overview

For thermal emitters of TPV system, the best choice to match emission spectrum of GaSb cell is 3D Tungsten photonic crystal [11, 117]. A 2D PhC in single-crystal tungsten which is well-matched to the PV diode of the whole system is introduced [12]. Compared with 1D PhC, the 2D PhC absorber has the obvious advantages, with a wider absorption capacity, a high absorption rate, and a wide-angle of absorption [118]. In the second-half of this work, the optimizations of 2D Tungsten PhC will be discussed by moderating the shape of air holes and materials filling in the holes instead of air. In order to ensure the simulation has practical meaning in industrial use, processing error is considered (e.g. the diameter of holes in the substrate).

5.2 Silicon based photonic crystals

5.2.1 Dielectric rods in air background

The energy gap of GaSb cell is approximately 0.72 eV and its corresponding wavelength is around 1.7 μm. Since the concept of selective emitters exists, rare-earth oxides were regarded as the ideal materials [119]. With the development of processing technology and the innovation of materials and structures, tungsten photonic crystal shows better spectrum emissivity [11, 44, 120]. This chapter will give bandgap characteristics of 2D photonic crystals of different shapes of holes in the substrate and different material to be filled in the holes. For the silicon rods in triangular lattice air background, three different models of shapes are simulated:

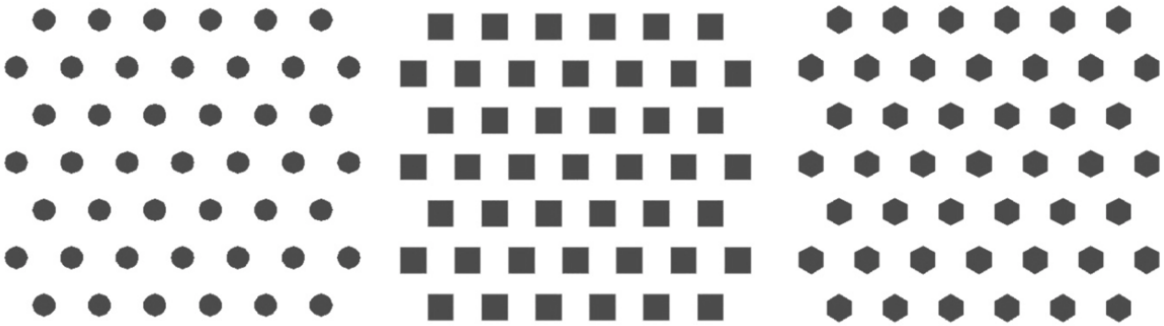

Figure 5.1: Schematic diagram of circular (left), square (middle) and hexagonal (right) rods.

In Fig. 5.2, bandgap for both TE and TM mode can be observed at specific frequency range. Two TE bandgaps and three TM bandgaps are found in Fig. 5.2(a). For square rods in Fig. 5.2(b), there are 3 TM bandgaps and no TE bandgaps. Only one TE bandgap and 3 for TM mode are found for hexagonal rods. The width of each bandgap found is given in Table. 5.1. The complete bandgap can be obtained only when the shape of rods is hexagonal.

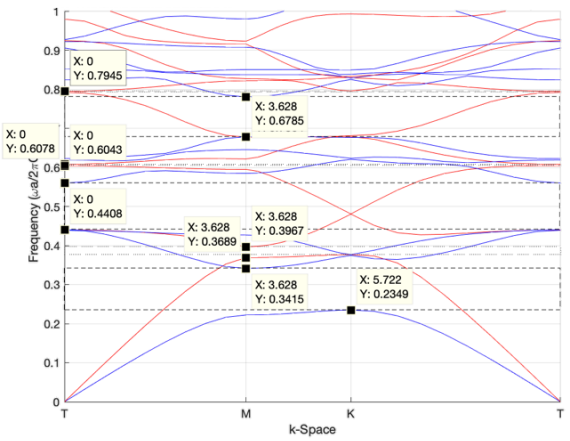

(a)

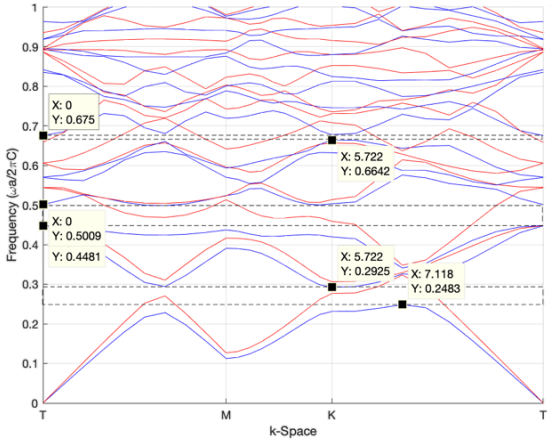

(b)

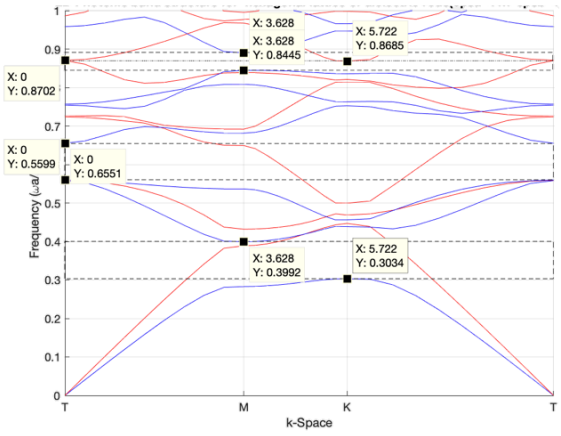

(c)

Figure 5.2: Photonic bands for structures from Fig. 5.1, (a) circular rods, (b) square rods and (c) hexagonal rods.

Combining Figure 5.2(a) and Table 5.1, the normalised frequency range of the main TM bandgap of circular rods is located at 0.2349-0.3415. The width of bandgap is 0.1066 and its central frequency is 0.2882. For square rods, the main bandgap for TM polarization is only 0.0442 at 0.2483-0.2925. None of the structures mentioned above obtains complete bandgap. However, for hexagonal rods in air background, the complete bandgap is 0.0017. Here, utilization ratio is presented to show how large the bandgap width can be. The central frequency ω_{mid} and the utilization ratio calculated as $\frac{\triangle\omega}{\omega_{mid}}$ are 0.8694 and 0.2% respectively.

Table 5.1: Bandgap width of TE, TM modes and complete bandgaps for silicon rods.

Mode	Circular holes	Square holes	Hexagonal holes
TE mode	δ_1=0.0018	none	δ_1=0.0017
	δ_2=0.0035		
TM mode	δ_1=0.01019	δ_1=0.0108	δ_1=0.0456
	δ_2=0.119	δ_2=0.0528	δ_2=0.0952
	δ_3=0.1066	δ_3=0.0442	δ_3=0.0958
Complete bandgap	none	none	δ=0.0017

Based on the simulation results, the structure with dielectric rods in air achieves larger TM than TE bandgaps .The superscripts means the number of bandgaps. It is obvious that the amount of TM bandgaps obtained is more than that of TE bandgaps. Although the model of hexagonal rods gives the only complete bandgap among the considered structures, the width is too small to be useful in practical applications.

5.2.2 Air holes in silicon substrate

Similarly, there are further simulations for different shapes of air holes on silicon substrate as Fig. 5.3 shows. The shapes of holes are circular, square and hexagonal, same geometric options as in the previous sub-chapter.

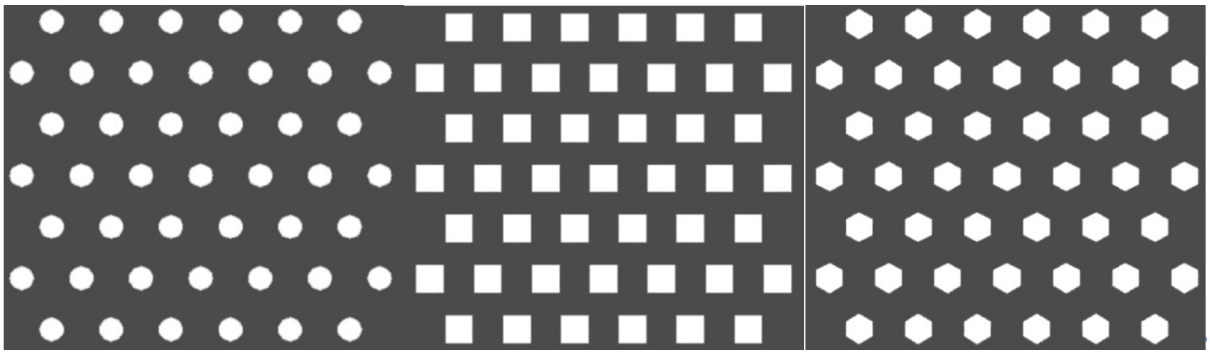

Figure 5.3: Schematic diagram of circular (left), square (middle) and hexagonal (right) holes.

According to the simulation results, only 1 bandgap for TE mode is found from normalised frequency range of 0.2092 to 0.2751 in Fig. 5.4(a). From Fig. 5.4(b), the bandgap widths of TE and TM bandgaps are 0.0543 and 0.0059, respectively. The corresponding widths of these bandgaps in hexagonal structure are 0.0721 and 0.086. Table. 5.2 lists all the data involved and 2 complete bandgaps are obtained for both square and hexagonal holes in the substrate.

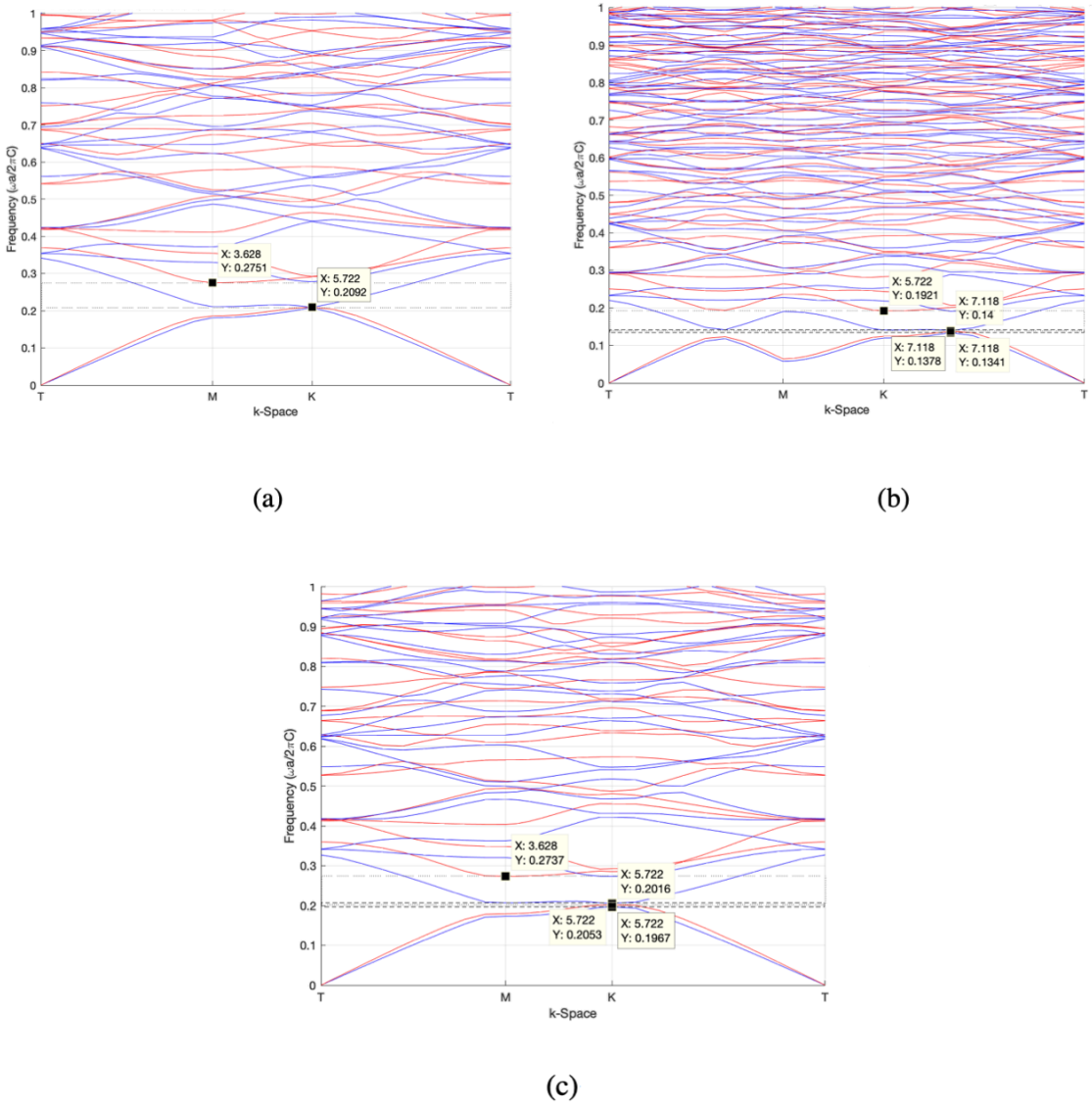

Figure 5.4: Photonic bands for structures from Fig. 5.3, (a) cirular holes, (b) square holes and (c) hexagonal holes.

In summary, both square and hexagonal structures give the complete bandgaps. Their widths are 0.0022 and 0.0037, respectively. The percentage of utilization can be 1.58% for square and 1.82% for hexagonal, at central frequency 0.1389ω and 0.2035ω correspondingly. The circular holes, on the other hand, give the bandgap for TE mode only, at 0.2422ω.

Table 5.2: Bandgap widths for TE, TM modes and complete bandgaps for air holes.

Mode	Circular holes	Square holes	Hexagonal holes
TE mode	δ_1=0.0659	δ_1=0.0543	δ_1=0.0721
TM mode	none	δ_1=0.059	δ_1=0.086
Complete bandgap	none	δ=0.0022	δ=0.0037

From the simulations of silicon based 2-D triangular lattice PhC, the band structures are researched on how to enlarge the complete bandgaps. Effective methods to approach this target are modifying the structures and materials [121, 122]. As the existing structures of two-dimensional photonic crystals introduced in our previous work are well established, the next chapter will discuss material substitutions based on cell characteristics in thermophotovoltaic applications.

5.3 Tungsten based photonic crystals

5.3.1 Hexagonal lattice tungsten photonic crystal

Since GaSb cell is used in the TPV system in the study and the bandgap equivalent wavelength is 1.78μm, the dielectric constant of tungsten should be selected in this range (in this case, over 1.1-1.78μm). The value is found as 21.216 at 1.8μm, so that most of electromagnetic waves beyond the specified range can be reflected. This will severely reduce the heat effects of crystal material, in other words, improve the photoelectric conversion efficiency. The difference between substrate and holes(rods) is shown below in Figure 5.5 if the material is replaced by tungsten. Similarly, the simulations will be divided into 2 different lattice types and 3 different shapes of holes(rods) for each type of lattice.

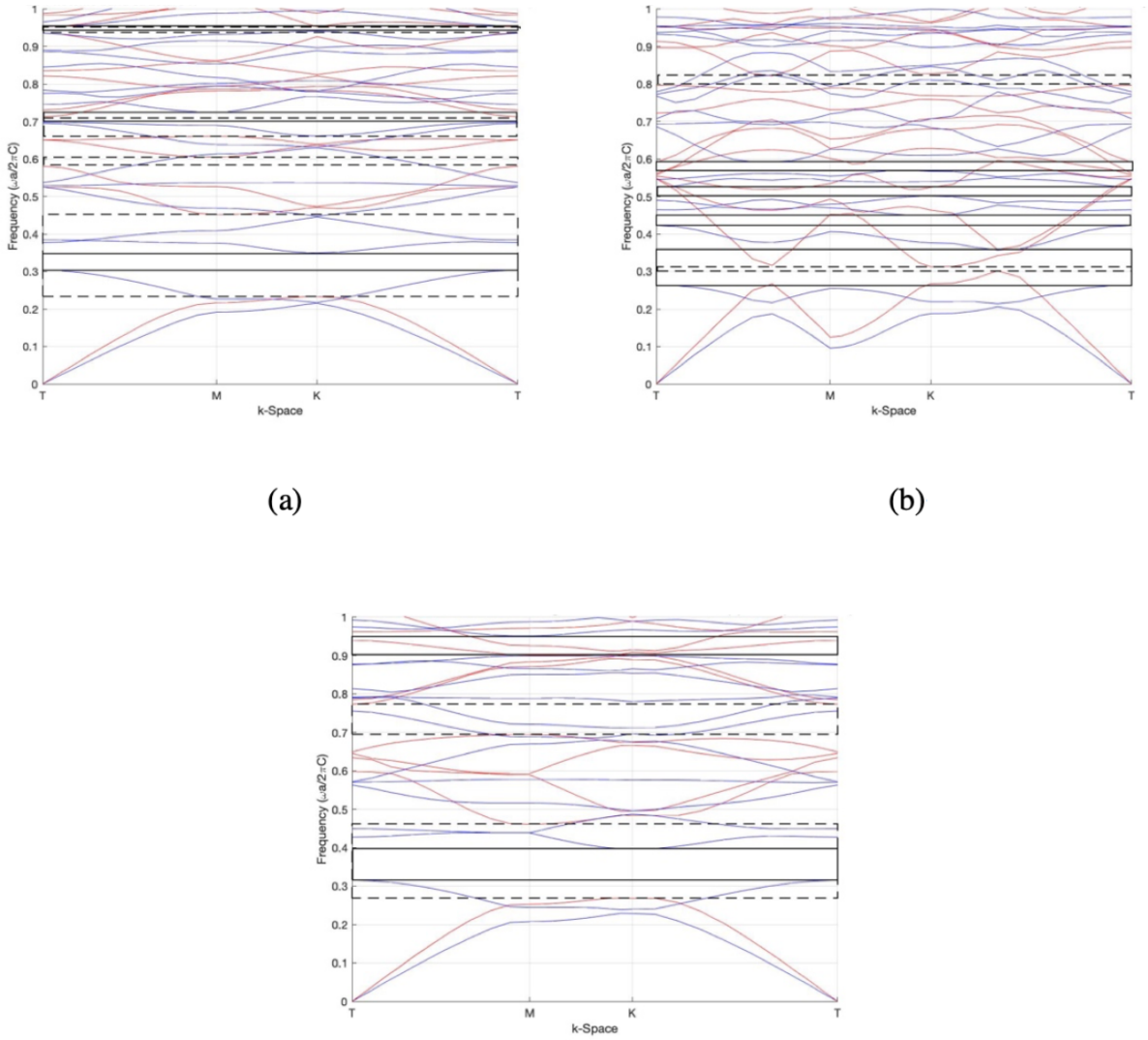

Figure 5.5: Photonic band structure of (a) circular, (b) square and (c) honeycomb holes in hexagonal lattice.

From the Fig. 5.5, each structure has more than one bandgap (the solid or dashed frame in the figures) for TE and TM modes, and at least one complete bandgap. For convenient and clear demonstration, only main complete bandgaps will be used for comparison in achieving the best utilization of band structures. Table 5.3 lists the frequency range of every bandgap and other parameters necessary to discuss in depth.

Table 5.3: Band characteristics of air holes in hexagonal lattice tungsten substrate.

Shape of rods	Mode	Frequency range	$\triangle\omega$	Central frequency	$\frac{\triangle\omega}{\omega_{mid}}$
Circular	TE mode TM mode Complete bandgap	0.2333-0.4515 0.304-0.3494 0.2333-0.4515	0.0454ω	0.327ω	13.90%
Square	TE mode TM mode Complete bandgap	0.3012-0.3124 0.2641-0.3573 0.3012-0.3124	0.0112ω	0.3068ω	3.65%
Hexagonal	TE mode TM mode Complete bandgap	0.268-0.4604 0.315-0.3959 0.315-0.3959	0.0809ω	0.3555ω	22.67%

For the structure with circular holes, the TE bandgap is larger than that for TM mode. The width of complete bandgap $\triangle\omega$ is 0.0454ω and central frequency $\omega_{mid} = 0.0327\omega$. The ratio of $\triangle\omega/\omega_{mid}$ is 13.90%. The bandgap of TE mode is also larger than that of TM for honeycomb holes. The complete bandgap width is 0.0909ω and the utilization ratio of bandgap can be 22.67%, which is the best among all the cases compared.

5.3.2 Rectangular lattice tungsten photonic crystal

Likewise, the simulations of rectangular lattice can be made and plotted in Fig. 5.6:

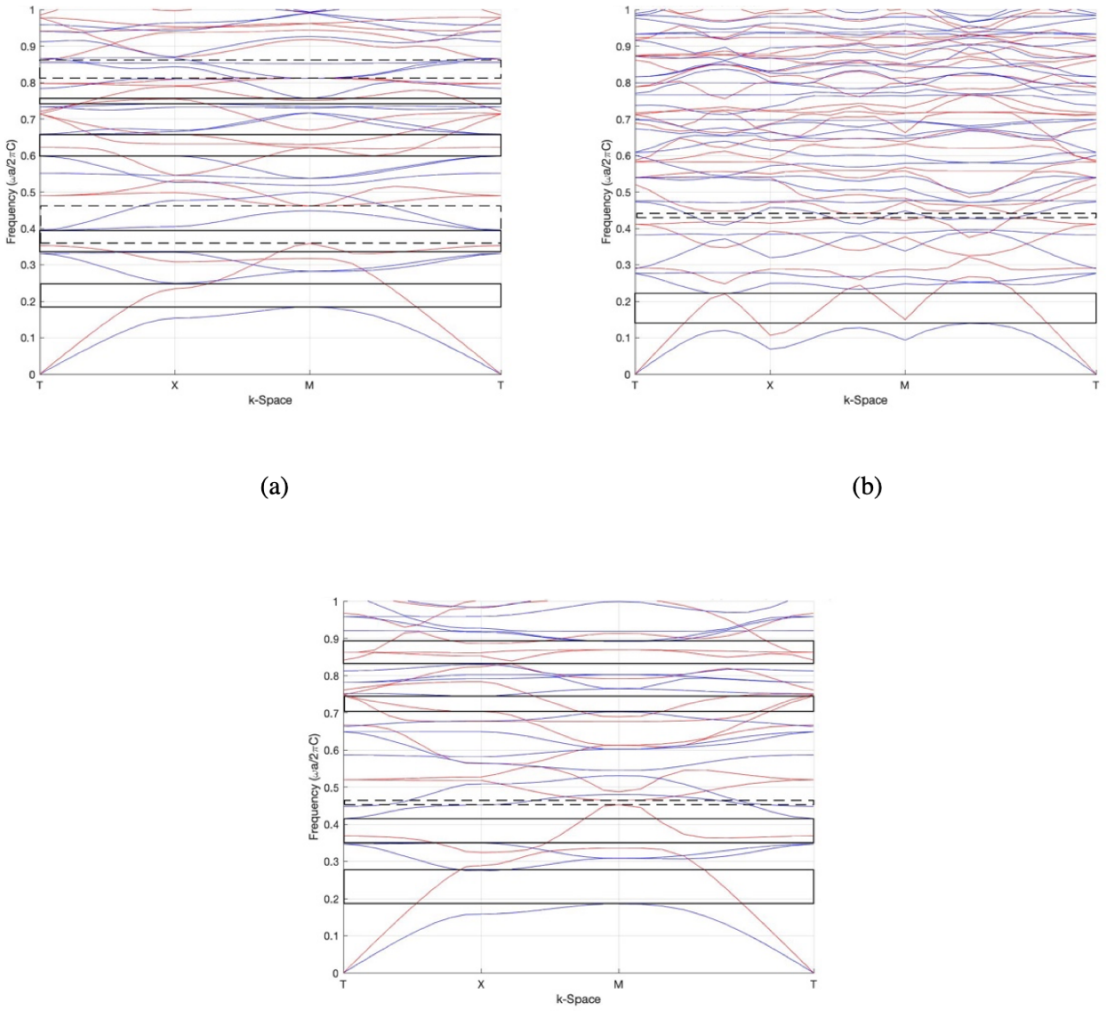

Figure 5.6: Photonic band structure of (a) circular, (b) square and (c) honeycomb holes in rectangular lattice.

Clearly, the complete bandgap can be only obtained for circular holes and produced by the intersection of TE and TM modes. For circular holes in the substrate, the complete bandgap width is 0.0376ω and the utilization ratio of bandgap is 9.97%.

Table 5.4: Band characteristics of air holes in rectangular lattice tungsten substrate.

Shape of rods	Mode	Frequency range	$\triangle\omega$	Central frequency	$\frac{\triangle\omega}{\omega_{mid}}$
Circular	TE mode TM mode Complete bandgap	0.3582-0.4606 0.3342-0.3958 0.3582-0.3958	0.0376ω	0.377ω	9.97%
Square	TE mode TM mode Complete bandgap	0.4274-0.4408 0.1389-0.2206 -	-	-	-
Hexagonal	TE mode TM mode Complete bandgap	0.4526-0.4643 0.3499-0.4151 -	-	-	-

5.3.3 Maximize the bandgap width using Genetic algorithm

By comparing various structures of 2D tungsten photonic crystals, honeycomb air holes in hexagonal lattice gives the best utilization ratio of band structures. The above discussions are all based on the same filling fraction of 0.7. To search for the best band structures, smaller and larger filling fractions of 0.6 and 0.8 are added to find which can give the largest bandgap width and utilization ratio.

Table 5.5: Band characteristics of honeycomb holes in hexagonal lattice optimised by Genetic algorithm.

Filling fraction	Frequency range	$\triangle\omega$	Central frequency	$\frac{\triangle\omega}{\omega_{mid}}$
0.6	0.2798-0.3115	0.0317ω	0.2957ω	10.72%
0.7	0.315-0.3959	0.0809ω	0.3555ω	22.76%
0.8	0.4662-0.5031	0.0369ω	0.4847ω	7.61%
0.7434	0.3412-0.4641	0.1229ω	0.4027ω	30.52%

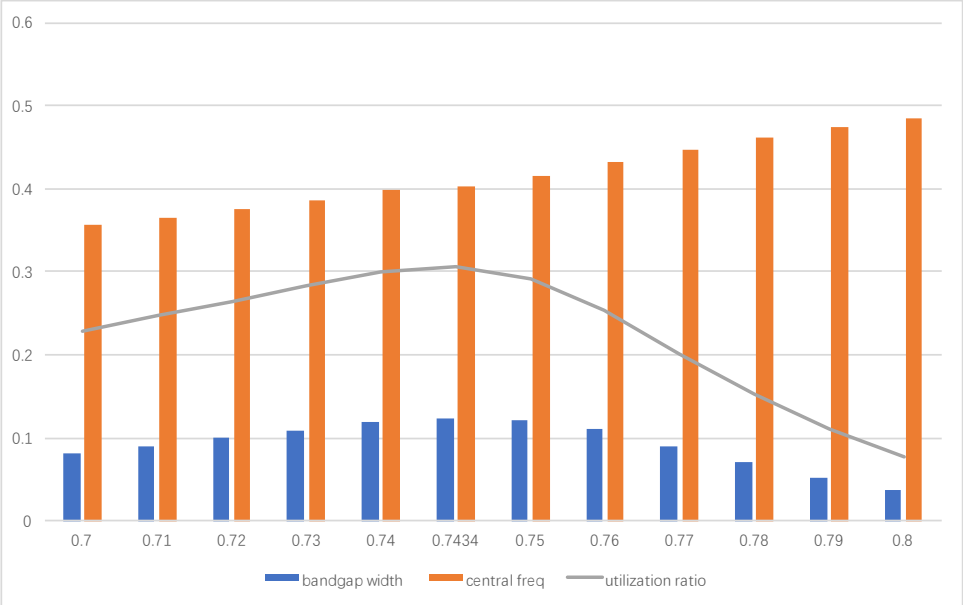

Figure 5.7: The utilization ratio (grey curve) of bandgap width (blue chart) at corresponding central frequency (orange chart). The range of filling fraction is from 0.7 to 0.8.

From the above table and Fig. 5.7, the best filling fraction is between 0.6-0.8. The range is set after inserting different filling fractions. According to previous research, evolution algorithm can be introduced here to search for the largest bandgap width and its corresponding filling fraction [84, 95, 123]. As shown in Table 5.5, the complete bandgap width is 0.0369ω at the normalized frequency range from 0.3412 to 0.4641. The utilization ratio of bandgap has peaked at 30.52% . Figure 5.8 gives the band structure of the optimal case, with a large complete bandgap observed. Since the target of this study is to use the band characteristics to obtain the best efficiency for reflecting back most of electromagnetic waves beyond the range accepted by GaSb cell, and our own design seems to be the best choice.

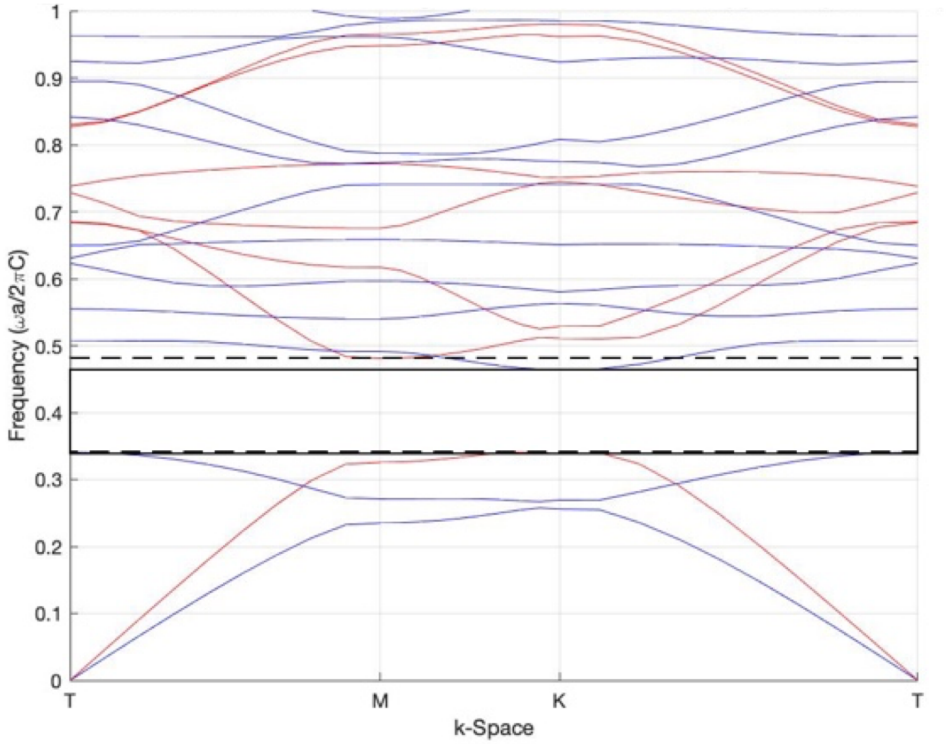

Figure 5.8: Photonic band structure of honeycomb holes in hexagonal lattice. (Filling fraction at 0.7434.)

5.4 Conclusion and further expectations

To summarise, the structure with silicon rods shows larger bandgaps for TE and TM modes but less complete bandgaps than that with air holes. For the 2D tungsten photonic crystal, hexagonal lattice with honeycomb holes is the best structure to give the largest complete bandgap width and percentage over central frequency. Genetic algorithm is applied to search for the filling fraction at the peak. Our own design combination of optical filters and thermal emitters can reach the highest conversion frequency to reflect most of electromagnetic waves with $\lambda > 1.8\mu m$ and accept those in this range. Since the current progress is focused on maximizing the bandgap for the largest reflection area in TPV applications, it is also interesting to do research on minimizing the bandgap, for using these structures in modulators. This will be discussed in detail in the next chapter.

Chapter 6

2-D Si/SiO2 photonic crystal slabs

This chapter aims to search for optimal photonic-crystal structures, which will deliver a large change of the effective refractive index at a target wavelength, based on the band structure shift of PhC slabs when the refractive index of silicon varies by a small amount by modulating the free carrier density in it. A small shift of the photonic band structure has a large effect on light with frequency near the band gap between two photonic bands, provided that during this band structure shift the band gap crosses this frequency, as discussed in [64, 124]. Calculations are done for 2D silicon-based photonic crystal slab with air holes, for various lattice types and shapes of holes, and changes of the effective refractive index between the first and second TM bands are obtained.

6.1 Overview

The electro-optic modulator is a key functional device in fibre-optic communications and networks, as well as in other areas [125]. The increasing demands for capacity of optical interconnects have increased the need for high-speed modulators. The conventional silicon-based modulators perform electro-optic modulation by using the plasma dispersion effect in silicon, i.e. the change of refractive index with the free-carrier density, by injection, depletion or accumulation. However, owing to the small change of refractive index which can be achieved in real structures, these modulators require a significant length of the phase-shifter arms, and face a bottleneck in improving the modulation rate and efficiency, making further improvements hard. A data rate of 50 Gb/s has been demonstated in a modulator based on free carrier depletion

[126], and a silicon-based electro-optic modulator with a modulation rate exceeding 64 Gb/s has been proposed [127].

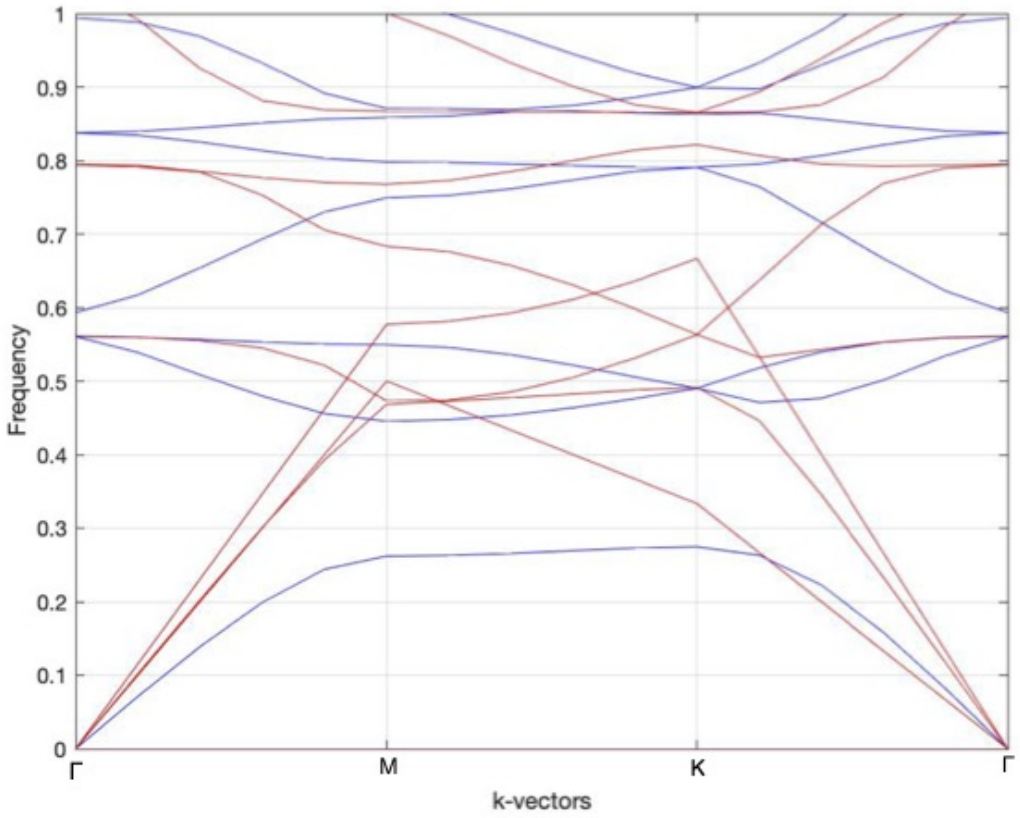

Figure 6.1: 2D photonic crystal slab of triangular lattice with circular air holes in silicon substrate(red curves with sharp changes at M and K is the light cone).

The restrictions present in bulk-like modulators can be overcome by tailoring the material and structure used in the modulator. A research on using phase change material (PCM) has shown that it also enables a high-performance modulator, with larger bandwidth, larger extinction ratio and lower operating voltage compared to the state-of-the-art models [128]. Another approach is based on using the two-dimensional photonic crystal (PhC) slab (made of silicon, and integrable on silicon platform) for two arms of Mach-Zehnder interferometer, and modulating the free carrier density in one or both arms [64]. By combining the advantages of MZI and ring modulators, the required phase shift of the proposed design comes from the change of effective refractive index of PhCs. The key issue is to find a structure with large effective refractive index change, in order to obtain significantly different phase accumulation in the two arms of the system. Mpb tool is used to calculate photonic band structure, like that shown as Fig.

6.1. In Fig. 6.1, the band structures of 2D triangular photonic crystal slab with circular holes etched in are given. Similarly, the electric field distributions and amplitude profiles can be also obtained using this tool.

6.2 Calculations of effective refractive index

In this study we calculate the effective refractive index for light propagating along the boundaries of irreducible Brillouin zone, obtained from the band structure calculated as described above.

The phase accumulation ϕ is linked to the effective refractive index n_{eff} as [64]:

$$\varphi = n_{eff}\frac{2\pi}{\lambda}d \tag{6.1}$$

where d is the propagation length of light, and the relation of wavevector k and frequency is given by Eq. (6.2) [129]:

$$k = \frac{\omega}{c}n_{eff} \tag{6.2}$$

Based on the experimental results of Soref and Bennett [130], the injection of electron and hole carriers leads to the refractive index change given by the sum of Eq. (6.3) and (6.4):

$$\triangle n_e = -8.8 \times 10^{-22} \times (\triangle N_e) \tag{6.3}$$

$$\triangle n_h = -8.5 \times 10^{-18} \times (\triangle N_h)^{0.8} \tag{6.4}$$

where $\triangle N_e$ and $\triangle N_h$ are the concentrations of electron and hole carriers in the silicon PhC slab, injected for purpose of shifting the PhC band structure. By injecting $\triangle N_e$ and $\triangle N_h$, both equal to 4.1×10^{18} cm^{-3}, the refractive index of silicon changes from 3.47 to 3.48, and this is used in further calculations (same as in [64]). Concerning the sign of the refractive index, it can be determined from the frequency variation with the k-vector, or using equi-frequency contours[131]. For instance, if k-vector varies along Γ-M direction and the corresponding frequency for a particular band is increasing as well, the sign of refractive index is positive, otherwise it would be

negative. In this case the group velocity and phase velocity have the same sign. The simulation process can be briefly described by the flow chart in Fig. 6.2. At the frequencies of 0.26 and $0.32(\omega a/\pi), different effective indices will be obtained. Since the effective index for the second band is negative du$

6.3 Simulations results and discussion

6.3.1 Structures from previous research

In this section the structure proposed by A. Govdeli, et al [124] is simulated using Mpb tool(Mit photonic bands tool) [56] as shown in Fig. 6.4. The key feature of this, MZI-based modulator with PhC in its arms, is that it provides positive and negative refractive index in the same structure in two different photonic bands. For the slab structure, with its finite height (unlike the conventional two-dimensional materials), the light is confined in the slab because of the refractive index difference between the slab and cladding layers on the upper and lower sides [52, 54, 55], and the dispersion will not be exactly the same as for the two-dimensional photonic crystal. It is useful to add the dispersion curve, called light cone (calculated with the average refractive index of the photonic crystal slab), in the band structure diagrams. By adding the light cone in Fig. 6.4, the available frequency within limits can be visually displayed.

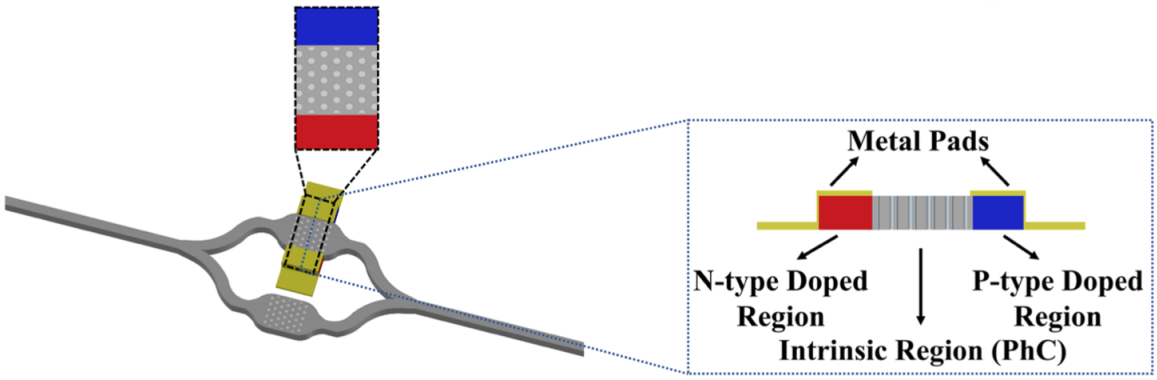

Figure 6.3: Schematic representation of the analysed structure.

It is important to note that the slab structure features symmetry on the plane z=0 and the k-vectors on x and y planes are observation targets. Thus, the TE and TM polarizations can be simply replaced by their analogous modes: even and odd modes respectively [56]. For the TM-like mode the effective refractive index for the first band is 1.66 and the corresponding value for the second band is -2.038. The total change of refractive index is therefore 3.698 when

the real refractive index of silicon changes by 0.01, increasing from 3.47 to 3.48 by free carriers injection (these values, corresponding to realistically achievable injected carriers density, were taken from [64]). This result is very close to that obtained by phase accumulation (3.886) in [64], and the small difference comes from different methods of calculation. With the range of k-vectors used in the calculations, and further for interpolation, the simulation is reasonably accurate and can be used as a reference data for further comparison with all other structures considered here.

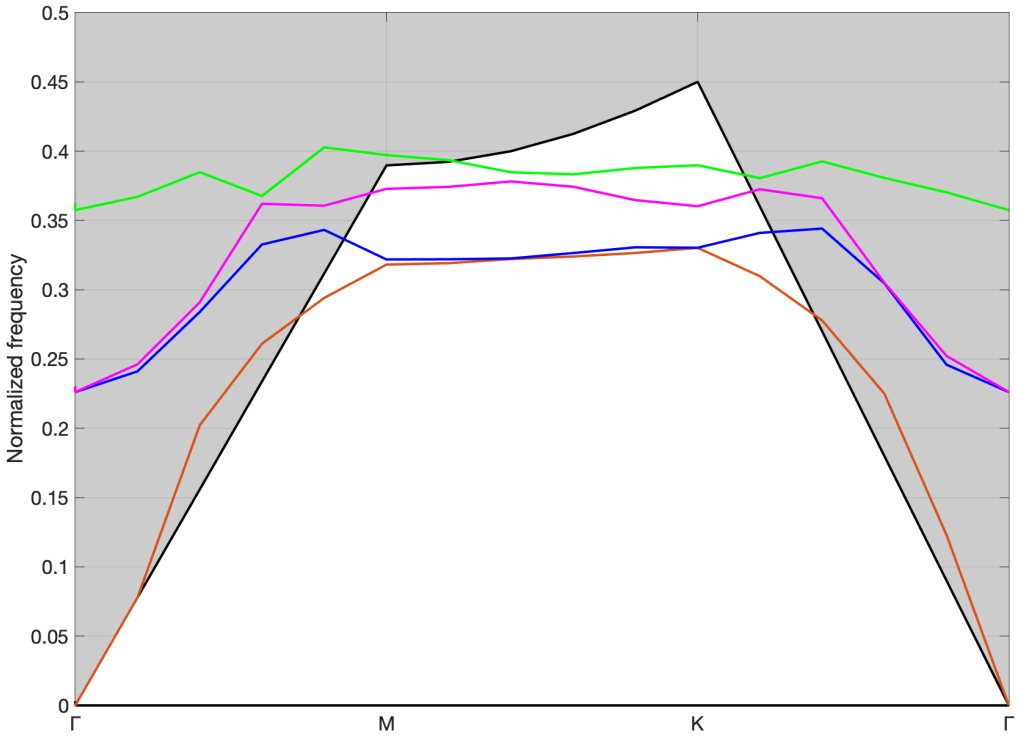

Figure 6.4: Photonic band structure of a circular air-hole triangular lattice, with r=0.3a and h=0.6a (lattice constant a=0.5μm) for TM-like polarization (the black curve is light cone).

6.3.2 Triangular lattices

For these structures the calculations were done for 5 types, according to the shapes of holes (sphere, ellipse, block, cylinder and cone), and each of them was analyzed using the Mpb code. From the optimization perspective, annular holes are used in all structures, as shown in Table 6.1. Furthermore, triangular holes in case of triangular lattice and honeycomb holes in case of honeycomb lattice are considered in order to analyze the performance if the holes are of the same shape as the lattice structure [62]. Matlab is used for calculation of some structures which

cannot be handled by the Mpb program due to its limited default geometry types and objects. Since the PWE in Matlab does not allow calculation with finite height in the vertical direction, the structures with * labels in Table 6.1 and 6.3 denote the conventional 2D photonic crystals, not slabs.

Table 6.1: Effective index calculations for triangular lattices.

	Triangular*	Ellipse	Block	Cylinder	Annular($r_i = 0.15a$)**	Sphere	Cone
n_{eff1}	1.169	2.066	1.575	1.66	2.055	1.805	1.828
n_{eff2}	-1.697	-1.197	-1.908	-2.038	-1.772	-2.121	-2.104
$\triangle n_{eff}$	2.366	3.263	3.483	3.698	3.827	3.926	3.932
Bandgap shift	6×10^{-4}	7×10^{-4}	7×10^{-4}	7×10^{-4}	6×10^{-4}	6×10^{-4}	6×10^{-4}

* label refers to the structure of conventional 2D PhC, not slab.

** label refers to the structure with inner radius optimised by evolution algorithm.

The outer radii of cylinder, annular, sphere and cone holes are all set as 0.3a for convenience of comparison. For annular type, the inner radius of holes (i.e. the radius of the silicon rods in the air holes) is 0.15a, which is found by optimization using Genetic algorithm, in the range of 0 to r. Among the structures of this type, the cone structure gives the highest effective index change, of 3.932, more than other geometries. In contrast, triangular lattice with the same shape of holes etched in silicon gives the lowest change of refractive index, of 2.366.

With the change of refractive index of silicon from 3.47 to 3.48, the bandgap shifts from the first band to the second band for all the structures are also given in Table 6.1, and they do not vary much. The structure with cone holes is here the optimal one. The wavelength range in which the modulation can be done is 1610-1613 nm.

6.3.3 Square lattices

Another typical lattice type is the square lattice, and its corresponding shape in three-dimensional space is a block. The length of each side is set to 0.6a for comparison, same as the diameter of other models. It is worth mentioning that the optimal structure is block holes, and its effective index change is 3.827. For the annular holes, the range of inner radius is set to be 0-0.3a and the optimized result provided by the algorithm is 0.1a.

In terms of bandgap shift, the structure with cylinder holes gives the lowest value, while the block hole structures give 6×10^{-4} and are optimal for this lattice type. The wavelength range

in which the modulation can be done is here 1643-1680nm.

Table 6.2: Effective index calculations for square lattices.

	Ellipse	Cone	Sphere	Annular($r_i = 0.1a$)	Cylinder	Block
n_{eff1}	2.361	2.207	2.185	2.196	1.655	2.055
n_{eff2}	-0.873	-1.131	-1.258	-1.38	-2.038	-1.772
$\triangle n_{eff}$	3.234	3.338	3.443	3.576	3.693	3.827
Bandgap shift	6×10^{-4}	5×10^{-4}	6×10^{-4}	5×10^{-4}	3×10^{-4}	6×10^{-4}

6.3.4 Honeycomb lattices

Honeycomb structure is a variant of the triangular lattice, with two holes per unit cell at specific positions, as shown in Fig. 6.3 [56, 132, 133]. The specific design of honeycomb lattice with the same shape of etched holes gives the value of the refractive index change of 3.416, intermediate among the cases given in Table 6.3. In contrast to previous results, elliptical shape shows a better performance, with RI change of 3.55, than most of other structures. The only case where the total index change approaches 4 is for annular holes on the dielectric substrate, delivering the RI change of 3.952. Effective refractive indices for the first and second band are 2.047 and -1.905 respectively. The inner radius optimized by the evolution algorithm here is 0.15a, similar to that found in other cases.

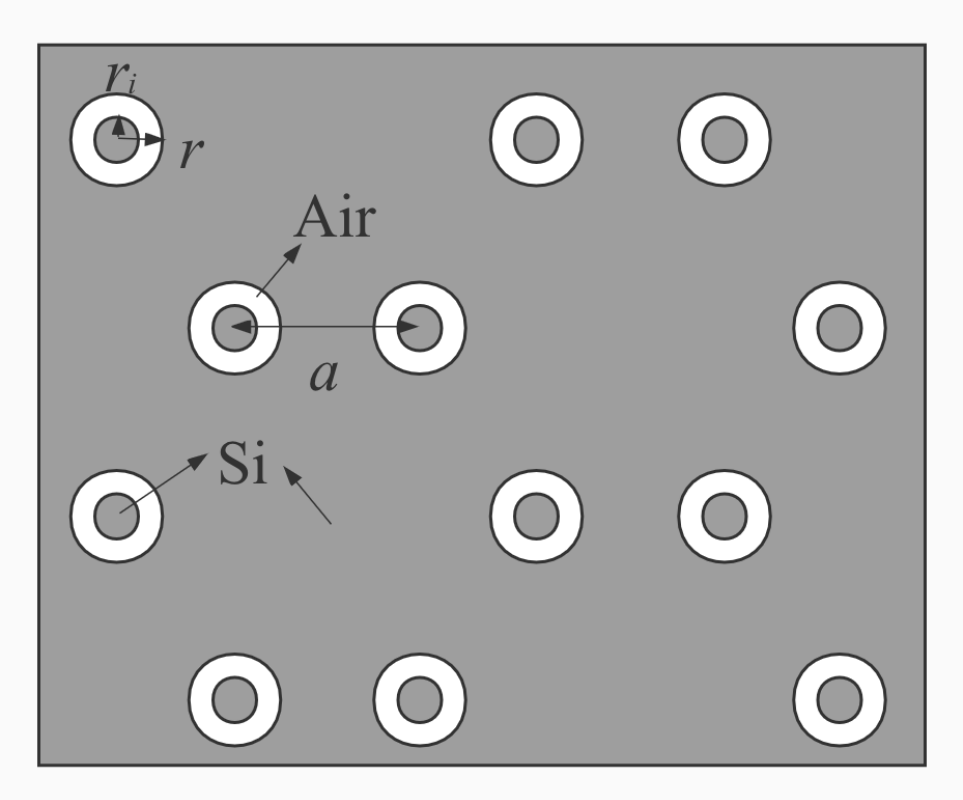

Figure 6.5: 2D-annular Si photonic crystal with honeycomb lattice. The lattice constant a=0.6 , height h=0.6a, outer radius of the holes r=0.3a.

Table 6.3: Effective index calculations for honeycomb lattices.

	Cylinder	Block	Honeycomb*	Sphere	Ellipse	Cone	Annular($r_i = 0.15a$)**
n_{eff1}	1.358	1.579	2.129	1.561	2.021	1.669	2.047
n_{eff2}	-1.819	-1.776	-1.287	-1.966	-1.529	-2.02	-1.905
$\triangle n_{eff}$	3.177	3.355	3.416	3.527	3.55	3.689	3.952
Bandgap shift	8×10^{-4}	7×10^{-4}	6×10^{-4}	7×10^{-4}	6×10^{-4}	4×10^{-4}	6×10^{-4}

* label refers to the structure of conventional 2D PhC, not slab.

** label refers to the structure with inner radius optimised by evolution algorithm.

In this structure the largest bandgap shift is for cylinder holes, but the refractive index change is here much smaller than for annular holes, so annular hole structure is optimal for modulators. Interestingly, for this lattice type, the bandgap shift varies with the annular hole radius, but according to the refractive index change, the one with inner radius of 0.15a is the best choice. The wavelength range acceptable for modulation here is 1572-1575nm.

Comparing the results obtained for all the structures considered in this study shows that annular air hole is the optimal geometry, giving somewhat better results than that in [64]. Annular air

holes on dielectric substrate can be viewed as the combination of silicon rods in air background and air holes on silicon substrate [63, 134]. This gives a reduced symmetry of the crystal structure, and enhanced scattering strength, and this makes it easier to obtain bandgaps than in other structures. Furthermore, the simulations are performed for TM-like polarization bands, and the annular mode is more likely to produce bandgaps, due to its special fabrication of combining both rods and holes [135–137]. The bandgap between the first two bands is located between 0.257637 and 0.25764 as Fig. 6.4 shows. The frequency difference is just $3 \times 10^{-6}\omega$ and the central frequency is 0.2576385 (the number of digits is given just to illustrate the small width of the bandgap). The ratio of bandgap width and the central frequency of this structure is $1.164 \times 10^{-3}\%$. Since the purpose of this study is to search for promising structures for the electro-optic modulator, such a small width of the bandgap is very useful for high-speed modulation.

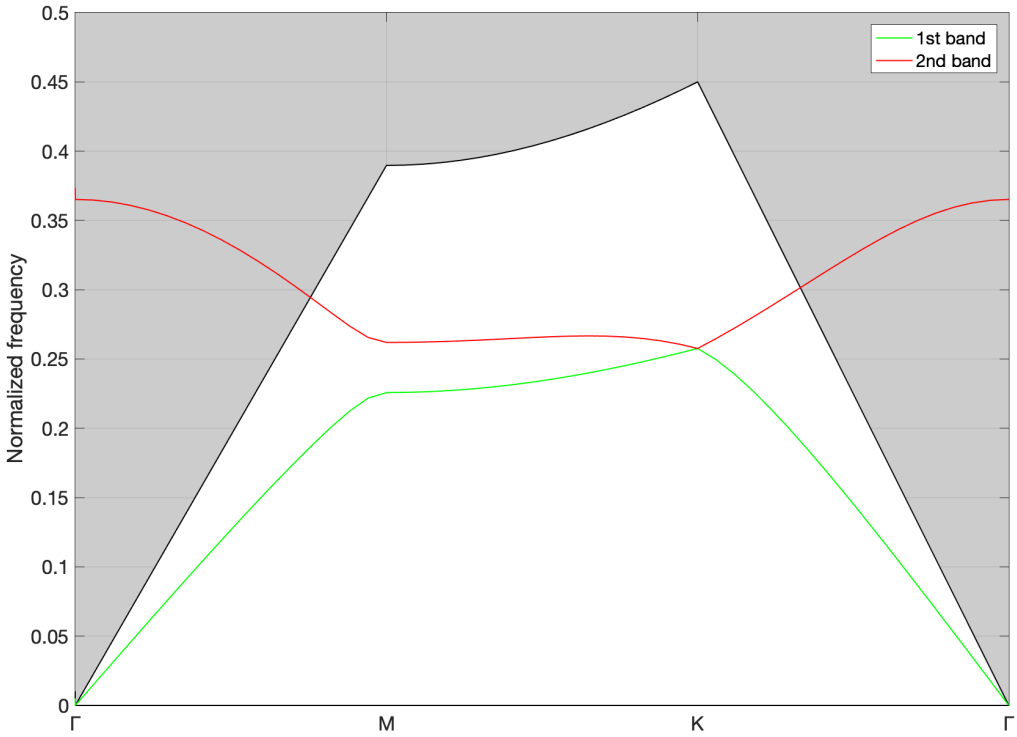

Figure 6.6: Band structures of annular air-hole honeycomb lattice for TM-like polarization,with r=0.3a and h=0.6a (lattice constant a=0.5μm)(the black curve is light cone).

6.4 Comparison with related research results

6.4.1 Triangular lattice

The lattice constant a in A. Govdeli's work was set to 0.5 μm. The air holes radius and thickness were 0.3 and 0.6 a, respectively. The effective refractive index difference of 3.73 can be achieved in the air-hole structure with triangular lattice (1.68 for n_1 and -2.05 for n_2, as shown in Figure 6)[64], while the annular structure with identical structural parameters yields a higher refractive index difference, of 3.827, and a smaller band gap shift. This demonstrates that using the new structure can lead to improved modulation performance.

From Fig. 6.7(a), another PhC with triangular air holes lattice is introduced, with thickness $0.57a$ and radius $0.244a$, where the lattice constant a is $0.4561\mu m$. The positive and negative refractive indices are 1.71 and -1.31 at $0.292(\omega a/2\pi c)$ and $0.3156(\omega a/2\pi c)$, respectively. In Fig. 6.7(b), the structure with circular holes is simulated according to the data given in the paper. The effective refractive index for the first band is 1.641 and for the second band it is -1.332. The effective RI change is 2.973, very close to the value (3.02) given in the paper, and the bandgap shift is 1.8×10^{-3}. The calculation is also made for annular-hole structure for comparison, shown by solid blue lines in Fig. 6.7(b). The outer radius here is $0.244a$, and the inner radius is $0.01a$. The effective refractive index for the first band is 1.432, and the negative refractive index for the second band is -1.736 at $0.3156(\omega a/2\pi c)$. The total change of the effective refractive index is 3.168, a bit larger than for the circular structure. The bandgap shift is 2.1×10^{-3}, also a bit larger than in the first case.

6.4.2 Annular structure

From the above discussion the annular hole structures are shown to have larger effective index difference than other structures. The recent research on negative refraction in annular photonic crystals (APCs) also points to the potential of annular rods to be used in light modulators [139]. Fig. 6.8(a) shows the band structures for different values of inner radius, from 0.1 to 0.25 μm. The lattice constant a is $1\mu m$, and the outer radius is $0.4a$. Since the discussion in this paper does not include APC slabs, it is interesting to model such a structure and compare its performance.

The photonic bands of circular rods and annular rods structures are shown in Fig. 6.8(b). The

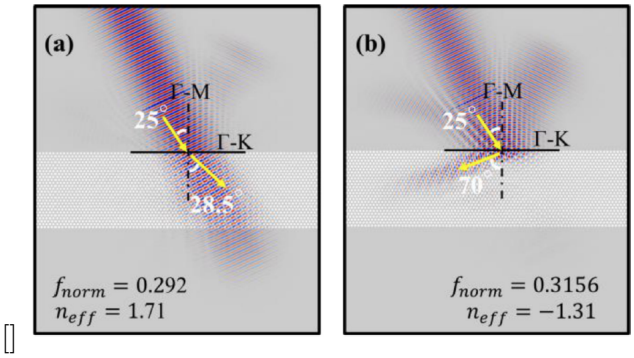

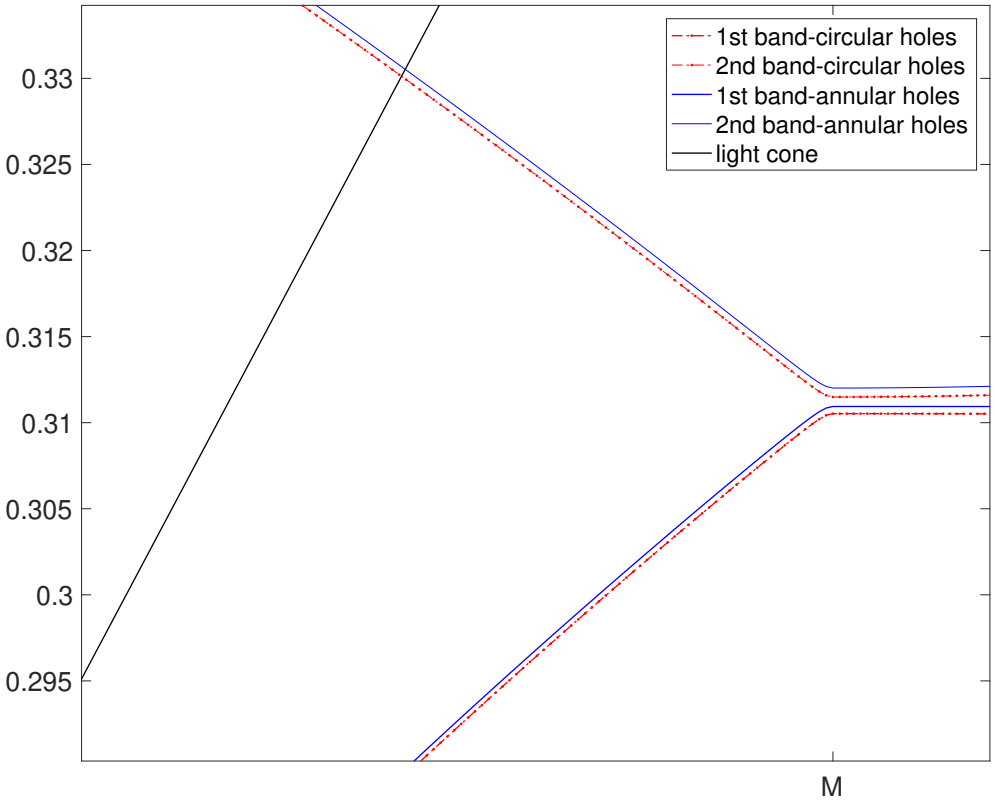

Figure 6.7: (a) Electric field distribution for light with the normalized frequency 0.292 ($\omega a/2\pi c$) in the PhC, obtained by the FDTD method.[138]; (b) Photonic band structure of the structure given in [138] (dashed red), and of our designed annular structure (solid blue).

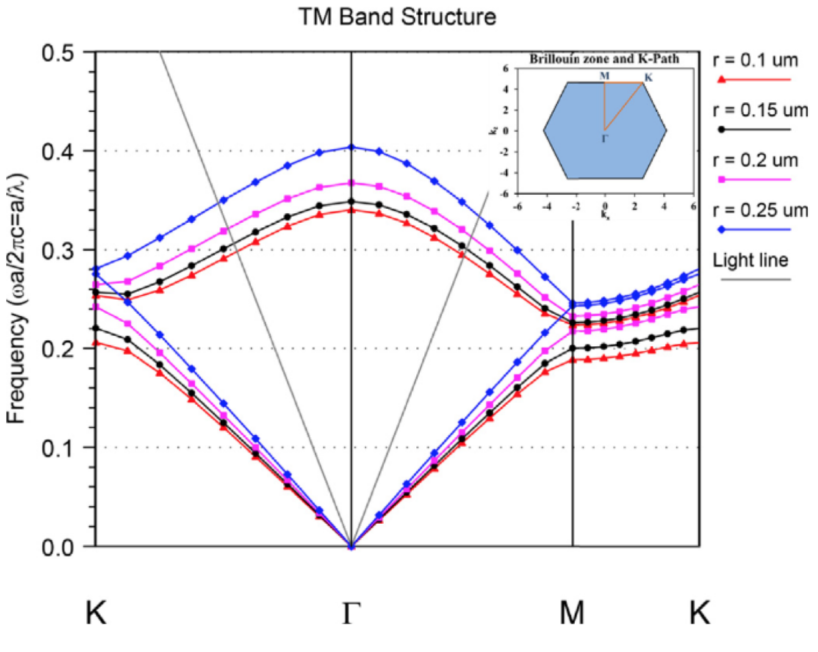

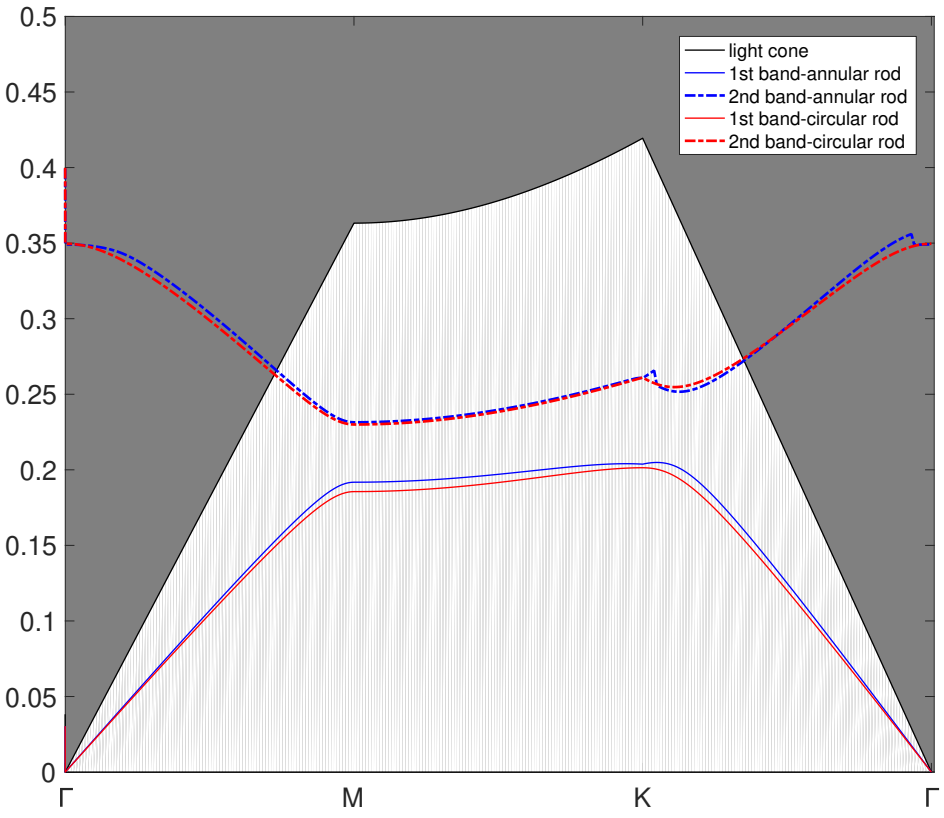

Figure 6.8: (a) Band structures for different values of inner radius, of $0.1\mu m$,$0.15\mu m$, $0.2\mu m$ and $0.25\mu m$, for TM polarization[139]; (b) Photonic band structure of circular rod (red) and annular rod (blue) structures.

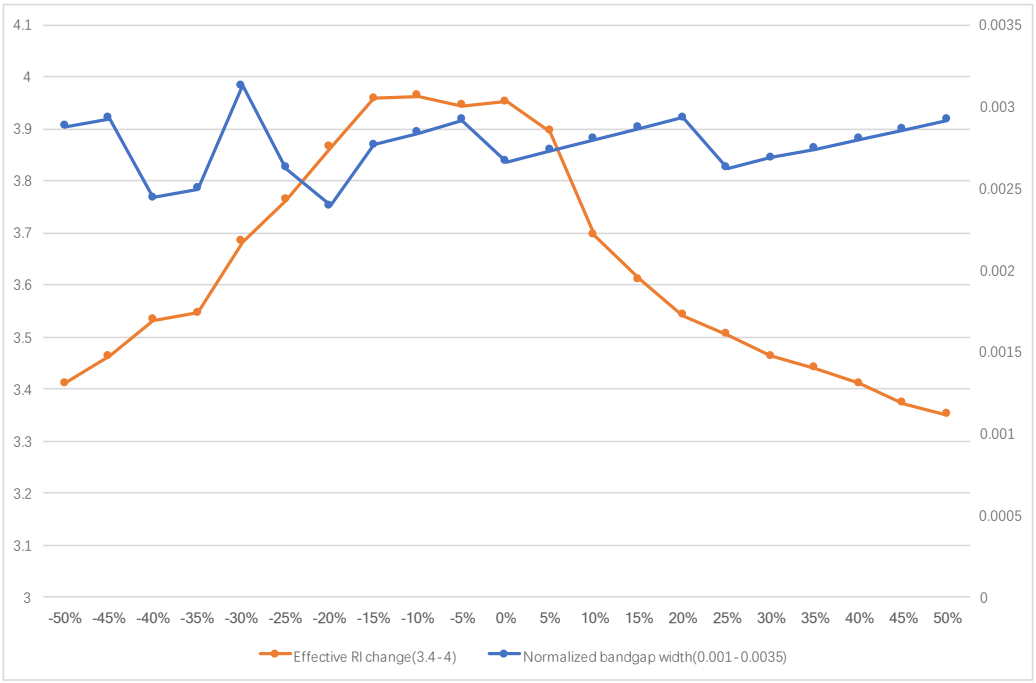

Figure 6.9: Effective refractive index change (red) and normalized bandgap width ($\triangle\omega/\omega_{mid}$)(blue) dependence on the structure parameters, for honeycomb lattice with annular air holes. 0% means that the inner radius is r=0.15a.

TM-like bandgap for circular rods is 0.03 and its central frequency is 0.2164. The utilization rate of the bandgap is 13.86%. The effective refractive indices for the first and second bands are 1.7496 and -1.0366, respectively, so the effective RI change is 2.7862. For annular rods the bandgap width is 0.0252, located at central frequency of 0.2174. The utilization rate is 11.59%, which is smaller than for circular structure. The positive refractive index for the first band is 1.8314 and the negative index for the second band is -1.052, so the total change of effective refractive index is 2.8834, larger than for the other structure. Therefore, the annular rod structure is better for light modulation applications, since it has a smaller photonic band gap and a larger effective refractive index change. Together with the above conclusions, this also shows that the annular structure improves the performance of both air holes or dielectric rods.

6.4.3 Tolerance to inner radius variations

In this section we consider the effects of the annular photonic crystals' structural parameters variation on the structure performance. Fig. 6.9 shows the variation of the normalized band gap and effective refractive index as the inner radius of air holes varies in the range -50% to +50% around the optimised value 0.15a. From Fig. 6.9 the effective index change is rather constant

when the inner annular diameter is in the range of -15% to 5% around the optimal value $0.15a$. As for the normalised bandwidth, it is also relatively stable, between 0.25% and 0.3%. This indicates that there is not much change in the photonic band structure when the inner diameter of the air holes is drastically adjusted. For better modulating performance, smaller bandgap if preferable and the corresponding tolerance range is -20% to 20%. And the minimum value occurs when the inner radius is 20% smaller. Therefore, the fabrication tolerance limits for the annular hole diameter can be perceived as -15% to 5% around the optimal value, and the structure would practically maintain its best performance in this range.

6.5 Conclusions and further expectations

Using the plane-wave expansion method, the effective RI change in two-dimensional Si PhC slabs, induced by varying the refractive index of silicon, was investigated, for application in electro-optic modulators. The structures with different lattice types and with different arrangements of holes were considered and compared. The annular air-hole photonic crystal slab gives the optimal performance in this respect, with the largest index change for both rectangular and honeycomb lattices, and with a rather high value for triangular lattice. The ring structure has a little advantage over the typical cylindrical shape in both the air hole and the dielectric column structures when comparing the pertinent research findings since 2018. The inner radius of annular holes was optimized using a Genetic algorithm to search for a small bandgap width which is favorable for high-speed modulation, and the tolerance limits of fabrication defects were also considered. The final results show that a reasonable range of fabrication errors can be tolerated without a significant decrease of the performance.

Chapter 7

Conclusions and future perspectives

Throughout the course of this research, the application and study of photonic crystals in the field of thermophotovoltaics has become increasingly widespread and well researched. Since the concept of photonic crystals was first introduced in 1987, the spectral control and photonic band utilisation of TPV systems have been significantly improved. Controlling the emission spectrum of thermal emitters to give them the desired selective radiation characteristics is an important way to improve the conversion efficiency of the whole system. Increased attention is now being drawn to improving the photovoltaic conversion efficiency of thermophotovoltaics, for example, filters with $M_G F_2$ structures were proposed in 2018, and the optimised structures demonstrated significant improvements in optical performance and spectral efficiency. In 2019, an emitter based on a silicon rod-type photonic crystal obtained a high efficiency (11.2%) of 1.65 times the previously reported record (6.8%). A ZrO_2/ZrO_2-aerogel filter reached a maximum TPV system efficiency of around 27% in 2021. The limitations of the conversion efficiency of thermophotovoltaic systems due to the limitations of conventional semiconductor materials are gradually decreasing.

7.1 Conclusions

In order to improve the conversion efficiency of thermophotovoltaic systems and to circumvent the problems of defects that may be encountered in practical applications, the research described in this thesis establishes an understanding of two main areas, the performance improvement of one-dimensional photonic crystal optical filters and the photonic band optimisation of 2D

photonic crystals.

This thesis first investigates the non-periodic structure of a 1D photonic crystal thermal emitter to explore the effect of irregularly arrayed films on emissivity. In the discussion, it is observed that the aperiodic structure achieves high emissivity with a smaller total film thickness and fewer interference peaks similar to that of a multi-layer periodic structure. Similar performance enhancements are seen in studies of filter-related applications. By including the complex refractive index, this work describes the reduction in spectral efficiency of a 10-layer one-dimensional Si/SiO_2 photonic crystal, providing a systematic approach to the study of inevitable defects in the deposition process. A structure consisting of alternating defect and dielectric layers containing a complex refractive index reduces the average spectral efficiency in a specific wavelength range by up to around 11%.

In addition, the degree of interfacial roughness has been investigated in this study. In a 10-layer Si/SiO_2 1D photonic crystal filter, increasing the roughness by a root mean square height Z = 0.001 μm per layer decreases the average spectral efficiency by approximately 3.5%. This reduction surges to 38% as Z increases to 0.01 μm. In addition to the problems that may arise in the multilayer structure described above, this paper also uses genetic algorithm to optimise the thickness of each film so that the optimised spectral efficiency is closer to that of the original structure without defects taken into account. In a discussion of photonic crystal filters under the influence of interface roughness, this thesis also finds that higher optical performance is obtained by using spectral efficiency as the optimisation target than by using transmittance as the target. Also, in cases where rough film surfaces cannot be avoided, film systems with fewer layers are a better choice.

In recent years, 2D photonic crystals have become an efficient option used to control thermal radiation spectroscopy. The research in this thesis highlights the fact that the two-dimensional photonic crystals can give a larger photonic forbidden band when optimised in terms of material and structure, hence the choice of tungsten with a larger dielectric constant and a more suitable absorption range for GaSb, which is commonly used for thermophotovoltaic cells, instead of silicon in conventional solar cells. Through comparison and algorithm optimisation, a triangular lattice honeycomb hole tungsten photonic crystal with a filling rate of 74.34% is found to give the largest forbidden band width and centre frequency occupation.

Additionally, the possible minimum values are given in the study of the extreme values of the

photonic band characteristics. For 2D photonic crystal slabs, their finite height in the direction perpendicular to light propagation makes them somewhat similar to 3D photonic crystals. In simulations of the 3 lattice types, with 8 hole shapes, the annular hole is more likely to yield a TM-like bandgap. Comparing the resulting optimal structures, the honeycomb lattice with annular holes gives the smallest bandgap width and largest effective refractive index of $3 * 10^{-6}$ and 3.952 respectively. This study emphasises that this optimal structure is optimised for fast band switching with a small bandgap shift by inner radius optimisation.

7.2 Future expectations

The results of this thesis demonstrate that technological breakthroughs are still possible and necessary in the following areas. Regarding 1D photonic crystal filters, the fabrication methods can be further optimised and adjusted to avoid complex refractive indices as well as interfacial roughness as much as possible. Together with the optimisation of the layer thickness, this research is expected to lead to an increase in the efficiency of thermophotovoltaic systems in terms of filter performance. Furthermore, the study of non-periodic thermal emitters in this thesis could consider the inclusion of an impurity layer to further increase the density of states in the photonic band, which could help to achieve enhanced spontaneous radiation. In particular, the optimisation of the periodic structure leads to an increase in the maximum value of the emission peaks beyond the main peak. If these spurious emissions around the central frequency can be utilised, it will contribute to the overall radiation performance.

Furthermore, based on the photonic band structures of the 2D photonic crystals reported in this study, microstructural adjustments to the surface can be added to the optimal structure of the tungsten crystal. This research is now more extensive and in-depth, but calculation methods for complex structures still need further investigation. In addition, studies of 2D photonic crystal slabs should consider more hole structures to obtain a larger effective refractive index and smaller bandgap shift.

The photonic crystal designs discussed in this thesis for applications such as filters and emitters help to achieve more stable, less fabrication demanding and more efficient components for thermophotovoltaic systems. Designing components with higher performance and a wider range of available temperatures to suit the characteristics of different thermal sources is the overall goal of future research.

References

1. Ferrari, C., Melino, F., Pinelli, M., Spina, P. & Venturini, M. Overview and status of thermophotovoltaic systems. *Energy Procedia* **45,** 160–169 (2014).
2. Coutts, T. J. An overview of thermophotovoltaic generation of electricity. *Solar energy materials and solar cells* **66,** 443–452 (2001).
3. Datas, A. & Algora, C. Global optimization of solar thermophotovoltaic systems. *Progress in Photovoltaics: Research and Applications* **21,** 1040–1055 (2013).
4. Crystals, J. *JX Crystals – Infrared Energy* `https://jxcrystals.com/wp/`. Accessed 14 May 2021.
5. Christ, S. & Seal, M. *Viking 29 – A Thermophotovoltaic Hybrid Vehicle Designed and Built at Western Washington University* `https://doi.org/10.4271/972650.`. Accessed 14 May 2021.
6. Khosroshahi, F. K., Ertürk, H. & Mengüç, M. P. Optimization of spectrally selective Si/SiO2 based filters for thermophotovoltaic devices. *Journal of Quantitative Spectroscopy and Radiative Transfer* **197,** 123–131 (2017).
7. Mbakop, F. K., Tom, A., Dadjé, A., Vidal, A. K. C. & Djongyang, N. One-dimensional comparison of TiO2/SiO2 and Si/SiO2 photonic crystals filters for thermophotovoltaic applications in visible and infrared. *Chinese Journal of Physics* **67,** 124–134 (2020).
8. Su, A. & Gao, Y. Filter characteristics of one-dimensional photonic crystal with complex dielectric constant. *Chinese Journal of Lasers* **36,** 1535 (2009).
9. Ghanekar, A., Sun, M., Zhang, Z. & Zheng, Y. Optimal design of wavelength selective thermal emitter for thermophotovoltaic applications. *Journal of thermal science and engineering applications* **10** (2018).

10. Fleming, J. Addendum:"Three-Dimensional Photonic-Crystal Emitter For Thermal Photovoltaic Power Generation"[Appl. Phys. Lett. 83, 380 (2003)]. *Applied Physics Letters* **86,** 380 (2005).

11. Lin, S.-Y., Moreno, J. & Fleming, J. Three-dimensional photonic-crystal emitter for thermal photovoltaic power generation. *Applied physics letters* **83,** 380–382 (2003).

12. Celanovic, I., Jovanovic, N. & Kassakian, J. Two-dimensional tungsten photonic crystals as selective thermal emitters. *Applied Physics Letters* **92,** 193101 (2008).

13. Gomard, G., Drouard, E., Letartre, X., Meng, X., Kaminski, A., Fave, A., Lemiti, M., Garcia-Caurel, E. & Seassal, C. Two-dimensional photonic crystal for absorption enhancement in hydrogenated amorphous silicon thin film solar cells. *Journal of Applied Physics* **108,** 123102 (2010).

14. Datas, A. & Martı, A. Thermophotovoltaic energy in space applications: Review and future potential. *Solar Energy Materials and Solar Cells* **161,** 285–296 (2017).

15. Melnick, C. & Kaviany, M. From thermoelectricity to phonoelectricity. *Applied Physics Reviews* **6,** 021305 (2019).

16. Lenert, A., Bierman, D. M., Nam, Y., Chan, W. R., Celanović, I., Soljačić, M. & Wang, E. N. A nanophotonic solar thermophotovoltaic device. *Nature nanotechnology* **9,** 126–130 (2014).

17. Rinnerbauer, V., Ndao, S., Yeng, Y. X., Chan, W. R., Senkevich, J. J., Joannopoulos, J. D., Soljačić, M. & Celanovic, I. Recent developments in high-temperature photonic crystals for energy conversion. *Energy & Environmental Science* **5,** 8815–8823 (2012).

18. Baldasaro, P., Raynolds, J., Charache, G., DePoy, D., Ballinger, C., Donovan, T. & Borrego, J. Thermodynamic analysis of thermophotovoltaic efficiency and power density tradeoffs. *Journal of Applied Physics* **89,** 3319–3327 (2001).

19. Dziendziel, R. J., DePoy, D. M. & Baldasaro, P. F. *Tandem filters using frequency selective surfaces for enhanced conversion efficiency in a thermophotovoltaic energy conversion system* US Patent 7,166,797. Jan. 2007.

20. Zenker, M., Heinzel, A., Stollwerck, G., Ferber, J. & Luther, J. Efficiency and power density potential of combustion-driven thermophotovoltaic systems using GaSb photovoltaic cells. *IEEE Transactions on Electron Devices* **48,** 367–376 (2001).

21. Whale, M. & Cravalho, E. G. Modeling and performance of microscale thermophotovoltaic energy conversion devices. *IEEE Transactions on Energy Conversion* **17,** 130–142 (2002).

22. Fourspring, P. M., DePoy, D. M., Beausang, J. F., Gratrix, E. J., Kristensen, R. T., Rahmlow Jr, T. D., Talamo, P. J., Lazo-Wasem, J. E. & Wernsman, B. *Thermophotovoltaic spectral control* in *AIP Conference Proceedings* **738** (2004), 171–179.

23. Ehsani, H., Bhat, I., Borrego, J., Gutmann, R., Brown, E., Dziendziel, R., Freeman, M. & Choudhury, N. Optical properties of degenerately doped silicon films for applications in thermophotovoltaic systems. *Journal of applied physics* **81,** 432–439 (1997).

24. Rahmlow, T., Lazo-Wassem, J., Gratrix, E., Fourspring, P., DePoy, D. & Azarkevich, J. *Engineering spectral control using front surface filters for maximum TPV energy conversion system performance* in *2nd International Energy Conversion Engineering Conference* (2004), 5678.

25. Celanovic, I., O'Sullivan, F., Ilak, M., Kassakian, J. & Perreault, D. Design and optimization of one-dimensional photonic crystals for thermophotovoltaic applications. *Optics letters* **29,** 863–865 (2004).

26. O'Sullivan, F., Celanovic, I., Jovanovic, N., Kassakian, J., Akiyama, S. & Wada, K. Optical characteristics of one-dimensional Si/ Si O 2 photonic crystals for thermophotovoltaic applications. *Journal of Applied Physics* **97,** 033529 (2005).

27. Dobrowolski, J. & Kemp, R. Refinement of optical multilayer systems with different optimization procedures. *Applied optics* **29,** 2876–2893 (1990).

28. Lee, C.-C., Wu, K. & Chen, Y.-J. *Reflection coefficients and optical admittances loci monitoring for thin film coatings and its applications to optical systems* in *Optical Complex Systems: OCS11* **8172** (2011), 81720Y.

29. Dong, Y., Xuelei, W. & Xiangzhong, Q. Research on forbidden band gap of one-dimensional photonic crystal changed under different incidence angles. *Optoelectron Technol* **29,** 51 (2009).

30. Olivier, S., Rattier, M., Benisty, H., Weisbuch, C., Smith, C., De La Rue, R., Krauss, T., Oesterle, U. & Houdré, R. Mini-stopbands of a one-dimensional system: The channel waveguide in a two-dimensional photonic crystal. *physical Review B* **63,** 113311 (2001).

31. Inouye, H. & Kanemitsu, Y. Direct observation of nonlinear effects in a one-dimensional photonic crystal. *Applied physics letters* **82,** 1155–1157 (2003).

32. Simonot, L. & Mazauric, S. Matrix method to predict the spectral reflectance o f stratified surfaces including thick layers and thin films. *HAL Arch.,* 1–20 (2015).

33. Hardhienata, H., Aziz, A. I., Rahmawati, D. & Alatas, H. *Transmission characteristics of a 1D Photonic crystal sandwiched by two graphene layers* in *Journal of Physics: Conference Series* **1057** (2018), 012003.

34. LI, W.-s., ZHANG, Q., HUANG, H.-m. & FU, Y.-h. Tansmssion Characteristics of 1-D Quasi-Periodic Photonic Crystal with Complex Refractive Index Medium. *Acta Sinica Quantum Optica* (2013).

35. Biswal, A., Kumar, R., Nayak, C. & Dhanalakshmi, S. Photonic bandgap characteristics of GaAs/AlAs-based one-dimensional quasi-periodic photonic crystal. *Optik* **234,** 166597 (2021).

36. Tikhonravov, A. V., Trubetskov, M. K., Tikhonravov, A. A. & Duparre, A. Effects of interface roughness on the spectral properties of thin films and multilayers. *Applied optics* **42,** 5140–5148 (2003).

37. Katsidis, C. C. & Siapkas, D. I. General transfer-matrix method for optical multilayer systems with coherent, partially coherent, and incoherent interference. *Applied optics* **41,** 3978–3987 (2002).

38. Chen, C., Dong, Z., Chen, H., Chen, Y., Zhu, Z. & Shi, W. Two-Dimensional Photonic Crystals. *Progress in Chemistry* **30,** 775–784 (2018).

39. Qiao-feng, D. Thermal Emission Control with Two-Dimensional Photonic Crystals. *Electro-Optic Technology Application* (2010).

40. Tsai, M.-W., Chuang, T.-H., Meng, C.-Y., Chang, Y.-T. & Lee, S.-C. High performance midinfrared narrow-band plasmonic thermal emitter. *Applied physics letters* **89,** 173116 (2006).

41. Biswas, R., Zhou, D., Puscasu, I., Johnson, E., Taylor, A. & Zhao, W. Sharp thermal emission and absorption from conformally coated metallic photonic crystal with triangular lattice. *Applied Physics Letters* **93,** 298 (2008).

42. John, S. & Wang, R. Metallic photonic-band-gap filament architectures for optimized incandescent lighting. *Physical Review A* **78,** 043809 (2008).

43. Jovanović, N., Čelanović, I. & Kassakian, J. *Two-dimensional Tungsten Photonic Crystals as Thermophotovoltaic Selective Emitters* in *AIP Conference Proceedings* **890** (2007), 47–55.

44. Araghchini, M., Yeng, Y., Jovanovic, N., Bermel, P., Kolodziejski, L., Soljacic, M., Celanovic, I. & Joannopoulos, J. Fabrication of two-dimensional tungsten photonic crystals for high-

temperature applications. *Journal of Vacuum Science & Technology B, Nanotechnology and Microelectronics: Materials, Processing, Measurement, and Phenomena* **29,** 061402 (2011).

45. Yeng, Y. X., Ghebrebrhan, M., Bermel, P., Chan, W. R., Joannopoulos, J. D., Soljačić, M. & Celanovic, I. Enabling high-temperature nanophotonics for energy applications. *Proceedings of the National Academy of Sciences* **109,** 2280–2285 (2012).

46. Rinnerbauer, V., Ndao, S., Xiang Yeng, Y., Senkevich, J. J., Jensen, K. F., Joannopoulos, J. D., Soljačić, M., Celanovic, I. & Geil, R. D. Large-area fabrication of high aspect ratio tantalum photonic crystals for high-temperature selective emitters. *Journal of Vacuum Science & Technology B, Nanotechnology and Microelectronics: Materials, Processing, Measurement, and Phenomena* **31,** 011802 (2013).

47. Yeng, Y. X., Chan, W. R., Rinnerbauer, V., Joannopoulos, J. D., Soljačić, M. & Celanovic, I. Performance analysis of experimentally viable photonic crystal enhanced thermophotovoltaic systems. *Optics express* **21,** A1035–A1051 (2013).

48. Rinnerbauer, V., Yeng, Y. X., Chan, W. R., Senkevich, J. J., Joannopoulos, J. D., Soljačić, M. & Celanovic, I. High-temperature stability and selective thermal emission of polycrystalline tantalum photonic crystals. *Optics express* **21,** 11482–11491 (2013).

49. Ghebrebrhan, M., Bermel, P., Yeng, Y., Celanovic, I., Soljačić, M. & Joannopoulos, J. Tailoring thermal emission via Q matching of photonic crystal resonances. *Physical Review A* **83,** 033810 (2011).

50. Jovanovic, N. Z. *Two-dimensional photonic crystals as selective emitters for thermophotovoltaic power conversion applications* PhD thesis (Massachusetts Institute of Technology, 2005).

51. Maruyama, S., Kashiwa, T., Yugami, H. & Esashi, M. Thermal radiation from two-dimensionally confined modes in microcavities. *Applied Physics Letters* **79,** 1393–1395 (2001).

52. Johnson, S. G., Fan, S., Villeneuve, P. R., Joannopoulos, J. D. & Kolodziejski, L. Guided modes in photonic crystal slabs. *Physical Review B* **60,** 5751 (1999).

53. Fan, S. & Joannopoulos, J. D. Analysis of guided resonances in photonic crystal slabs. *Physical Review B* **65,** 235112 (2002).

54. Moll, N. & Bona, G.-L. Comparison of three-dimensional photonic crystal slab waveguides with two-dimensional photonic crystal waveguides: Efficient butt coupling into these photonic crystal waveguides. *Journal of Applied Physics* **93,** 4986–4991 (2003).

55. Pugh, J., Ho, Y. D., Engin, E., Railton, C., Rarity, J. & Cryan, M. Novel high-Q modes in thick 2D photonic crystal slabs. *Journal of Optics* **15,** 035004 (2013).

56. Johnson, S. G. & Joannopoulos, J. D. Block-iterative frequency-domain methods for Maxwell's equations in a planewave basis. *Optics express* **8,** 173–190 (2001).

57. Vogelaar, L., Nijdam, W., van Wolferen, H. A., De Ridder, R., Segerink, F. B., Flück, E., Kuipers, L. & van Hulst, N. F. Large area photonic crystal slabs for visible light with waveguiding defect structures: fabrication with focused ion beam assisted laser interference lithography. *advanced materials* **13,** 1551–1554 (2001).

58. Whittaker, D. & Culshaw, I. Scattering-matrix treatment of patterned multilayer photonic structures. *Physical Review B* **60,** 2610 (1999).

59. Carlsson, N., Takemori, T., Asakawa, K. & Katayama, Y. Scattering-method calculation of propagation modes in two-dimensional photonic crystals of finite thickness. *JOSA B* **18,** 1260–1267 (2001).

60. Tikhodeev, S. G., Yablonskii, A., Muljarov, E., Gippius, N. A. & Ishihara, T. Quasiguided modes and optical properties of photonic crystal slabs. *Physical Review B* **66,** 045102 (2002).

61. Meade, R., Winn, J. N. & Joannopoulos, J. Photonic crystals: Molding the flow of light. *Pinceton Univ. Press* (1995).

62. Segovia-Chaves, F. & Vinck-Posada, H. Effects of pressure and rotation on photonic crystal slabs composed by triangular holes arranged in a hexagonal lattice. *Optik* **207,** 164382 (2020).

63. Kassa-Baghdouche, L. Photonic Band Gap Analysis of Silicon Photonic-Crystal Slab Structures with Non-Circular Air Holes. *Acta Physica Polonica, A.* **138** (2020).

64. Govdeli, A., Sarihan, M. C., Karaca, U. & Kocaman, S. Integrated optical modulator based on transition between photonic bands. *Scientific reports* **8,** 1–11 (2018).

65. Säynätjoki, A., Mulot, M., Vynck, K., Cassagne, D., Ahopelto, J. & Lipsanen, H. Properties, applications and fabrication of photonic crystals with ring-shaped holes in silicon-on-insulator. *Photonics and Nanostructures-Fundamentals and Applications* **6,** 42–46 (2008).

66. Cicek, A. & Ulug, B. Polarization-independent waveguiding with annular photonic crystals. *Optics Express* **17,** 18381–18386 (2009).

67. Jágerská, J., Le Thomas, N., Zabelin, V., Houdré, R., Bogaerts, W., Dumon, P. & Baets, R. Experimental observation of slow mode dispersion in photonic crystal coupled-cavity waveguides. *Optics letters* **34,** 359–361 (2009).

68. Lax, M. & Nelson, D. Maxwell equations in material form. *Physical Review B* **13,** 1777 (1976).

69. Parini, A., Bellanca, G., Trillo, S., Saccomandi, L. & Bassi, P. Transfer matrix and full Maxwell time domain analysis of nonlinear gratings. *Optical and quantum electronics* **36,** 189–199 (2004).

70. Troparevsky, M. C., Sabau, A. S., Lupini, A. R. & Zhang, Z. Transfer-matrix formalism for the calculation of optical response in multilayer systems: from coherent to incoherent interference. *Optics express* **18,** 24715–24721 (2010).

71. Liu, J., Sun, J., Huang, C., Hu, W. & Huang, D. Optimizing the spectral efficiency of photonic quantum well structures. *Optik* **120,** 35–39 (2009).

72. Nam, Y., Yeng, Y. X., Lenert, A., Bermel, P., Celanovic, I., Soljačić, M. & Wang, E. N. Solar thermophotovoltaic energy conversion systems with two-dimensional tantalum photonic crystal absorbers and emitters. *Solar Energy Materials and Solar Cells* **122,** 287–296 (2014).

73. Musin, R. & Zheltikov, A. Designing dispersion-compensating photonic-crystal fibers using a genetic algorithm. *Optics communications* **281,** 567–572 (2008).

74. Shi, S., Chen, C. & Prather, D. W. Plane-wave expansion method for calculating band structure of photonic crystal slabs with perfectly matched layers. *JOSA A* **21,** 1769–1775 (2004).

75. Xiao, S., Shen, L. & He, S. A plane-wave expansion method based on the effective medium theory for calculating the band structure of a two-dimensional photonic crystal. *Physics Letters A* **313,** 132–138 (2003).

76. Antos, R. & Veis, M. Fourier factorization with complex polarization bases in the plane-wave expansion method applied to two-dimensional photonic crystals. *Optics express* **18,** 27511–27524 (2010).

77. Winn, J. N., Fink, Y., Fan, S. & Joannopoulos, J. D. Omnidirectional reflection from a one-dimensional photonic crystal. *Optics letters* **23,** 1573–1575 (1998).

78. Vinogradov, A., Dorofeenko, A., Erokhin, S., Inoue, M., Lisyansky, A., Merzlikin, A. & Granovsky, A. Surface state peculiarities in one-dimensional photonic crystal interfaces. *Physical Review B* **74,** 045128 (2006).

79. Chiu, M.-H., Lee, J.-Y. & Su, D.-C. Complex refractive-index measurement based on Fresnel's equations and the uses of heterodyne interferometry. *Applied optics* **38,** 4047–4052 (1999).

80. Pettersson, L. A., Roman, L. S. & Inganäs, O. Modeling photocurrent action spectra of photovoltaic devices based on organic thin films. *Journal of Applied Physics* **86,** 487–496 (1999).

81. Zhan, T., Shi, X., Dai, Y., Liu, X. & Zi, J. Transfer matrix method for optics in graphene layers. *Journal of Physics: Condensed Matter* **25,** 215301 (2013).

82. Malitson, I. H. Interspecimen comparison of the refractive index of fused silica. *Josa* **55,** 1205–1209 (1965).

83. Tan, C. Determination of refractive index of silica glass for infrared wavelengths by IR spectroscopy. *Journal of Non-Crystalline Solids* **223,** 158–163 (1998).

84. Preble, S., Lipson, M. & Lipson, H. Two-dimensional photonic crystals designed by evolutionary algorithms. *Applied Physics Letters* **86,** 061111 (2005).

85. Sanchis, L., Håkansson, A., López-Zanón, D., Bravo-Abad, J. & Sánchez-Dehesa, J. Integrated optical devices design by genetic algorithm. *Applied Physics Letters* **84,** 4460–4462 (2004).

86. Zhou, Y., Bao, Z., Luo, Q. & Zhang, S. A complex-valued encoding wind driven optimization for the 0-1 knapsack problem. *Applied Intelligence* **46,** 684–702 (2017).

87. Wang, Y., Gao, S., Zhang, H. & Tang, Z. An improved genetic algorithm based complex-valued encoding (2010).

88. Botros, J., Ali, M. O., Tait, R. N., Amaya, R. E. & Gupta, S. Direct thermal emission testing of aperiodic dielectric stack for narrowband thermal emission at mid-IR. *Journal of Applied Physics* **127,** 114502 (2020).

89. Binidra, K., Miloua, R., Khadraoui, M., Kebbab, Z., Bouzidi, A. & Benramdane, N. Spectral control in thermophotovoltaic systems by optimized one-dimensional photonic crystals. *Optik* **156,** 879–885 (2018).

90. Miloua, R., Kebbab, Z., Chiker, F., Sahraoui, K., Khadraoui, M. & Benramdane, N. Determination of layer thickness and optical constants of thin films by using a modified pattern search method. *Optics letters* **37,** 449–451 (2012).

91. Amroun, M. & Khadraoui, M. Effect of substrate temperature on the properties of SnS2 thin films. *Optik* **184,** 16–27 (2019).

92. Park, C. H., Lee, W. I., Han, W. S. & Vautrin, A. Improved genetic algorithm for multi-disciplinary optimization of composite laminates. *Computers & Structures* **86,** 1894–1903 (2008).

93. Lu, J.-H., Cai, D.-P., Tsai, Y.-L., Chen, C.-C., Lin, C.-E. & Yen, T.-J. Genetic algorithms optimization of photonic crystal fibers for half diffraction angle reduction of output beam. *Optics Express* **22,** 22590–22597 (2014).

94. Minkov, M. & Savona, V. Automated optimization of photonic crystal slab cavities. *Scientific reports* **4,** 1–8 (2014).

95. Shen, L., Ye, Z. & He, S. Design of two-dimensional photonic crystals with large absolute band gaps using a genetic algorithm. *Physical Review B* **68,** 035109 (2003).

96. Li, H., Jiang, L., Jia, W., Qiang, H. & Li, X. Genetic optimization of two-dimensional photonic crystals for large absolute band-gap. *Optics communications* **282,** 3012–3017 (2009).

97. Jiang, L., Hu, W. & Wu, X. An Active Learning Genetic Algorithm Research Based on Pattern Search. *Journal of Wuhan University of Technology(Transportation Science & Engineering)* **35,** 246–249 (2011).

98. Bogani, C., Gasparo, M. & Papini, A. Generalized pattern search methods for a class of nonsmooth optimization problems with structure. *Journal of Computational and Applied Mathematics* **229,** 283–293 (2009).

99. Fühner, T. & Jung, T. Use of genetic algorithms for the development and optimization of crystal growth processes. *Journal of crystal growth* **266,** 229–238 (2004).

100. Aspnes, D. E. & Studna, A. Dielectric functions and optical parameters of si, ge, gap, gaas, gasb, inp, inas, and insb from 1.5 to 6.0 ev. *Physical review B* **27,** 985 (1983).

101. Ravindra, N., Ganapathy, P. & Choi, J. Energy gap–refractive index relations in semiconductors–An overview. *Infrared physics & technology* **50,** 21–29 (2007).

102. Narayanaswamy, A. & Chen, G. Thermal emission control with one-dimensional metallodielectric photonic crystals. *Physical Review B* **70,** 125101 (2004).

103. Yu, H., Zhang, H., Dai, Z. & Xia, X. Design and analysis of low emissivity radiative cooling multilayer films based on effective medium theory. *ES Energy & Environment* **6,** 69–77 (2019).

104. Voti, R. L., Larciprete, M., Leahu, G., Sibilia, C. & Bertolotti, M. Optimization of thermochromic VO2 based structures with tunable thermal emissivity. *Journal of Applied Physics* **112,** 034305 (2012).

105. Luk, T. S., Mclellan, T., Subramania, G., Verley, J. C. & El-Kady, I. Emissivity measurements of 3D photonic crystals at high temperatures. *Photonics and Nanostructures-Fundamentals and Applications* **6,** 81–86 (2008).

106. Luo, C., Narayanaswamy, A., Chen, G. & Joannopoulos, J. Thermal radiation from photonic crystals: a direct calculation. *Physical Review Letters* **93,** 213905 (2004).

107. Mostafa, S. I., Rafat, N. H. & El-Naggar, S. A. One-dimensional metallic-dielectric (Ag/-SiO2) photonic crystals filter for thermophotovoltaic applications. *Renewable Energy* **45,** 245–250 (2012).

108. Mustafa, K., Abdullah, M., Bakar, M. & Abdullah, M. Performance, combustion characteristics and economics analysis of a combined thermoelectric and thermophotovoltaic power system. *Applied Thermal Engineering* **193,** 117051 (2021).

109. Nichelatti, E. *et al.* Complex refractive index of a slab from reflectance and transmittance: analytical solution. *Journal of Optics A: Pure and Applied Optics* **4,** 400–403 (2002).

110. Pirvaram, A., Talebzadeh, N., Rostami, M., Leung, S. N. & O'Brien, P. G. Evaluation of a ZrO2/ZrO2-aerogel one-dimensional photonic crystal as an optical filter for thermophotovoltaic applications. *Thermal Science and Engineering Progress* **25,** 100968 (2021).

111. Suthar, B., Kumar, V., Kumar, A., Singh, K. S. & Bhargava, A. Thermal expansion of photonic band gap for one dimensional photonic crystal. *Progress in Electromagnetics Research Letters* **32,** 81–90 (2012).

112. Mbakop, F. K., Djongyang, N. & Radandi, D. One–dimensional TiO2/SiO2 photonic crystal filter for thermophotovoltaic applications. *Journal of the European Optical Society-Rapid Publications* **12,** 1–9 (2016).

113. Ghodgaonkar, D. K., Varadan, V. & Varadan, V. K. Free-space measurement of complex permittivity and complex permeability of magnetic materials at microwave frequencies. *IEEE Transactions on instrumentation and measurement* **39,** 387–394 (1990).

114. Saghai-Maroof, M. A., Soliman, K. M., Jorgensen, R. A. & Allard, R. Ribosomal DNA spacer-length polymorphisms in barley: Mendelian inheritance, chromosomal location, and population dynamics. *Proceedings of the National Academy of Sciences* **81,** 8014–8018 (1984).

115. Azadeh, A., Ghaderi, S. F., Nokhandan, B. P. & Sheikhalishahi, M. A new genetic algorithm approach for optimizing bidding strategy viewpoint of profit maximization of a generation company. *Expert Systems with Applications* **39,** 1565–1574 (2012).

116. Chaudhuri, B. & Garai, G. Grid clustering with genetic algorithm and tabu search process. *Journal of Pattern Recognition Research* **4,** 152–168 (2009).

117. Cui, K., Lemaire, P., Zhao, H., Savas, T., Parsons, G. & Hart, A. J. Tungsten–Carbon Nanotube Composite Photonic Crystals as Thermally Stable Spectral-Selective Absorbers and Emitters for Thermophotovoltaics. *Advanced Energy Materials* **8,** 1801471 (2018).

118. Bermel, P., Lee, J., Joannopoulos, J. D., Celanovic, I. & Soljačić, M. Selective solar absorbers. *Annual Review of Heat Transfer* **15** (2012).

119. Guazzoni, G., Kittl, E. & Shapiro, S. *Rare earth radiators for thermophotovoltaic energy conversion* in *1968 International Electron Devices Meeting* (1968), 130–130.

120. Arpin, K. A., Losego, M. D., Cloud, A. N., Ning, H., Mallek, J., Sergeant, N. P., Zhu, L., Yu, Z., Kalanyan, B., Parsons, G. N., *et al.* Three-dimensional self-assembled photonic crystals with high temperature stability for thermal emission modification. *Nature communications* **4,** 1–8 (2013).

121. Li, Z.-Y., Gu, B.-Y. & Yang, G.-Z. Large absolute band gap in 2D anisotropic photonic crystals. *Physical Review Letters* **81,** 2574 (1998).

122. Dobson, D. C. & Cox, S. J. Maximizing band gaps in two-dimensional photonic crystals. *SIAM Journal on Applied Mathematics* **59,** 2108–2120 (1999).

123. Preble, S. F., Lipson, H. & Lipson, M. F. *Novel two-dimensional photonic crystals designed by evolutionary algorithms* in *Nanophotonics for Communication: Materials and Devices* **5597** (2004), 118–128.

124. Govdeli, A. & Kocaman, S. *Tunable integrated optical modulator with dynamical photonic band transition of photonic crystals* in *Silicon Photonics XIV* **10923** (2019), 194–200.

125. Berezhno, A. Electro-optical modulators and shutters. *Journal of Optical Technology* **66,** 583 (1999).

126. Thomson, D. J., Gardes, F. Y., Fedeli, J.-M., Zlatanovic, S., Hu, Y., Kuo, B. P. P., Myslivets, E., Alic, N., Radic, S., Mashanovich, G. Z., *et al.* 50-Gb/s silicon optical modulator. *IEEE Photonics Technology Letters* **24,** 234–236 (2011).

127. Jalali, B., Yegnanarayanan, S., Yoon, T., Yoshimoto, T., Rendina, I. & Coppinger, F. Advances in silicon-on-insulator optoelectronics. *IEEE Journal of selected topics in Quantum Electronics* **4,** 938–947 (1998).

128. Ghosh, R. R., Bhardwaj, P. & Dhawan, A. Numerical modeling of integrated electro-optic modulators based on mode-gap shifting in photonic crystal slab waveguides containing a phase change material. *JOSA B* **37,** 2287–2298 (2020).

129. Anand, S. *Two Dimensional Photonic Crystals in InP-Based Materials* in *ECS Meeting Abstracts* (2006), 1267.

130. Soref, R. & Bennett, B. Electrooptical effects in silicon. *IEEE journal of quantum electronics* **23,** 123–129 (1987).

131. Jiang, B., Zhang, Y., Wang, Y., Liu, A. & Zheng, W. Equi-frequency contour of photonic crystals with the extended Dirichlet-to-Neumann wave vector eigenvalue equation method. *Journal of Physics D: Applied Physics* **45,** 065304 (2012).

132. Curély, J., Lloret, F. & Julve, M. Thermodynamics of the two-dimensional Heisenberg classical honeycomb lattice. *Physical Review B* **58,** 11465 (1998).

133. Weng, T.-I. & Guo, G. Band structure of honeycomb photonic crystal slabs. *Journal of applied physics* **99,** 093102 (2006).

134. Liu, W.-L. & Yang, T.-J. Variation of group velocity and complete bandgaps in two-dimensional photonic crystals with drilling holes into the dielectric rods. *Physica B: Condensed Matter* **368,** 151–156 (2005).

135. Scheuer, J. & Yariv, A. Optical annular resonators based on radial Bragg and photonic crystal reflectors. *Optics express* **11,** 2736–2746 (2003).

136. Khalkhali, T. F. & Bananej, A. Tunable complete photonic band gap in anisotropic photonic crystal slabs with non-circular air holes using liquid crystals. *Optics Communications* **369,** 79–83 (2016).

137. Shi, P., Huang, K., Kang, X.-l. & Li, Y.-p. Creation of large band gap with anisotropic annular photonic crystal slab structure. *Optics express* **18,** 5221–5228 (2010).

138. Govdeli, A. & Kocaman, S. On-chip switch and add/drop multiplexer design with left-handed behavior in photonic crystals. *IEEE Journal of Selected Topics in Quantum Electronics* **26,** 1–8 (2019).

139. Xia, F., Li, S., Zhang, K., Jiao, L., Kong, W., Dong, L. & Yun, M. Negative Luneburg lens based on the graded annular photonic crystals. *Physica B: Condensed Matter* **545,** 233–236 (2018).